Incursion on Contact Problems using a Meshless method

António Moisés Fonseca Ferreira

Thesis submitted to
Faculdade de Engenharia da Universidade do Porto
as a requirement to obtain the

MSc degree in Mechanical Engineering

under the supervision of:
Professor Jorge Américo Oliveira Pinto Belinha

and
Professor Lúcia Maria de Jesus Simas Dinis

and
Professor Renato Manuel Natal Jorge

Departamento de Engenharia Mecânica
Faculdade de Engenharia da Universidade do Porto

U.PORTO
FEUP FACULDADE DE ENGENHARIA
UNIVERSIDADE DO PORTO

Porto, July 2013

Abstract

Contact is one of the most important problems in many engineering fields. In the case of mechanical engineering, it is most important in the analysis of processes such as forging or sheet metal stamping.

In this work, the contact problem is extended to a meshless method, the Natural Neighbour Radial Point Interpolation Method (NNRPIM).

In the NNRPIM the Natural Neighbour concept is used in order to enforce the nodal connectivity. Using the Voronoï diagrams, constructed from the unstructured set of nodes discretizing the problem domain, it is possible to obtain the "influence-cells", which are in fact influence-domains entirely nodal dependent. From the Delaunay triangles, the dual of the Voronoï cells, a node-depending background mesh is created. This integration mesh is used in the numerical integration of the NNRPIM interpolation functions, which are constructed using the Radial Point Interpolators (RPI). The obtained interpolation functions possess the delta Kronecker property, which simplify the imposition of natural and essential boundary conditions.

A simple approximated non-linear algorithm is implemented, in order to apply the contact.

Several examples are tested, without friction and only considering the elastic approximated non-linear analysis. In the studied examples, plane stress and plane strain assumptions are considered. Arbitrary shape boundaries are used, both static and dynamic.

Resumo

O contacto é um dos mais importantes problemas nas diversas áreas de engenharia. No caso de engenharia mecânica, é muito importante na análise de processos de forjamento e conformação plástica de chapa.

Neste trabalho, "Natural Neighbour Radial Point Interpolation Method" (NNRPIM) é estendido á mecânica do contacto.

No NNRPIM, o conceito de vizinho natural (Natural Neighbour) é usado de forma a impor a conectividade nodal. Através do diagrama de Voronoï, construído a partir de um conjunto indiscriminado de nós que discretizam o domínio do problema, é possível obter as "células de influência" ("Influence-cells"), as quais são de facto domínios de influência, inteiramente dependentes dos nós.

A partir do diagrama de Delaunay, que é o gráfico dual do diagrama de Voronoï, é construída uma malha de integração dependente dos nós. Esta malha de integração é usada para a integração numérica das funções interpoladoras do NNRPIM, que são construídas usando os "Radial Point Interpolators" (RPI). As funções obtidas possuem a propriedade do delta de Kronecker, facilitando a aplicação das condições de fronteira naturais e essenciais.

Para aplicar o contacto, é implementado um algoritmo não linear aproximado.

Vários exemplos são testados, sem atrito e considerando apenas a análise não linear elástica aproximada. Nos exemplos estudados, são considerados o estado plano de tensão e o estado plano de deformação. São usadas fronteiras com formas arbitrárias, tanto fixas como móveis.

Contents

List of Figures

Abbreviations and symbols

Abbreviations

FDM	Finite Difference Method
FEM	Finite Element Method
FVM	Finite Volume Method
MMS	Meshless Methods
Mfree	Meshfree methods
DEM	Diffuse Element Method
MLS	Moving Least Squares
EFGM	Element Free Galerkin Method
SPH	Smooth Particle Hydrodynamics
RKPM	Reproducing Kernel Particle Method
MLPG	Meshless Local Petrov-Galerkin Method
MFS	Method of the Finite Spheres
FPM	Finite Point Method
RBFM	Radial Basis function Method
PIM	Point Interpolation Method
PAM	Point Assembly Method
RPIM	Radial Point Interpolation Method
RBFs	Radial Basis Functions
MFEM	Meshless Finite Element Method
NNFEM	Natural Neighbour Finite Element Method
NEM	Natural Element Method
NNRPIM	Natural Neighbour Radial Point Interpolation Method
DIM	Direct Imposition Method

Symbols (Latin)

$a_i(\mathbf{x}_I); b_i(\mathbf{x}_I)$	Non constant coefficients of $R_i(\mathbf{x}_I)$ and $p_j(\mathbf{x}_I)$ respectively	
A	xx coordinate of the linear boundary normal vector	
a_h	Radius of hole	$[m]$
a, b, c, d	Constant parameters of different functions	
$A_{S_{IJ}}$	Area of Voronoï sub-cell	$[m^2]$
A_{V_I}	Area of Voronoï cell	$[m^2]$
b	Body forces	$[N]$
B	Deformable matrix	
B	yy coordinate of the linear boundary normal vector	
b_h	Semi-width of contact surface	$[m]$
$C_s; P$	Multiquadratic constant parameters	
c	Constitutive matrix	
C	Linear boundary constant	
$C_{initial}$	Parameter defining the initial position of a linear boundary	
C_{final}	Parameter defining the final position of a linear boundary	
$d_{initial}$	Parameter defining the initial position of an asymptotic boundary	
d_{final}	Parameter defining the final position of an asymptotic boundary	
D	Height of solid domain	$[m]$
e	Thickness of solid domain	$[m]$
E	Young modulus	$[Pa]$
F	Global force vector	$[N]$
$\mathbf{f}_I$	Local Force vector	$[N]$
G	Shear modulus	$[Pa]$
G	Geometric matrix	
I	Moment of inertia	$[m^4]$
[**I**]	Identity matrix	
K	Global stiffness matrix	
$\mathbf{K}_{IJ}$	Local stiffness matrix	
k	Coefficient for defining plane Stress or plane Strain analysis	

L	Lagrangian functional	
L_c	Position along xx were contact starts	$[m]$
L_{sd}	Length of solid domain	$[m]$
$\mathbf{N}$	Voronoï diagram of a set of N nodes	
p	Hydrostatic pressure	$[Pa]$
$\mathbf{p}(\mathbf{x}_I)$	Vector with the monomials of the polynomial basis	
$p_j(\mathbf{x}_I)$	Monomials of the polynomial basis	
$\mathbf{P}_m$	Moment matrix of the polynomial basis	
q	Load per unit length	$[Nm^{-1}]$
Q	Concentrated load	$[N]$
r	Radial distance to point P	$[m]$
r_c	Circumference radius	$[m]$
r_f	Regress factor	
r_{Ii}	Multiquadratic Radial Basis Function	
R	Radius of the solid domain	$[m]$
$\mathbf{R}(\mathbf{x}_I)$	Vector of Radial Basis Functions	
$R_i(\mathbf{x}_I)$	Radial Basis Function	
$\mathbf{R}_Q$	Moment matrix of the Radial Basis Functions	
S	Slope of linear boundary	
T	Kinetic energy	$[J]$
$\bar{\mathbf{t}}$	Boundary forces	$[N]$
$[\mathbf{T}]$	Transformation matrix	
$[\mathbf{t}]$	Local transformation matrix	
$\mathbf{u}$	Displacements vector	$[m]$
u	Displacement along xx direction	$[m]$
$u(x)$	Interpolation function	
U	Strain energy	$[J]$
v	Displacement along yy direction	$[m]$
V	Imposed vertical displacement	$[m]$
V_I	Voronoï-cell	
W_f	Work produced by external forces	$[J]$
$\mathbf{x}$	Node coordinates	$[m]$

$x_{boundary}$	Coordinate along xx of a point in the boundary	$[m]$
x_{final}	Coordinate along xx of a node after deformation	$[m]$
$x_{initial}$	Coordinate along xx of a node before deformation	$[m]$
$\mathbf{x}_I$	Point of interest	
$y_{boundary}$	Coordinate along yy of a point in the boundary	$[m]$
y_{final}	Coordinate along yy of a node after deformation	$[m]$
$y_{initial}$	Coordinate along yy of a node before deformation	$[m]$
$y_{intercept}$	Linear equation intersection with yy axis	$[m]$

Symbols (Greek)

β	Angle of line connecting the origin to point P	$[rad]$
γ_{xy}	Distortion xy	
γ_{yz}	Distortion yz	
γ_{zx}	Distortion zx	
Γ_t	Boundary were external forces are applied	
δ	Distance between the beam and the rigid foundation	$[m]$
δ_{ij}	delta Kronecker property	
$\boldsymbol{\epsilon}$	Deformation tensor	
ϵ_{xx}	Linear strain along xx	
ϵ_{yy}	Linear strain along yy	
ϵ_{zz}	Linear strain along zz	
ν	Poisson ratio	
ξ	Variable of derivation	
π	Irrational number	
ρ	Mass density	$[kgm^{-3}]$
$\boldsymbol{\sigma}$	Stress tensor	$[Pa]$
σ_o	Stress magnitude	$[Pa]$
σ_{xx}	Normal stress along xx direction	$[Pa]$
σ_{yy}	Normal stress along yy direction	$[Pa]$
σ_{zz}	Normal stress along zz direction	$[Pa]$
τ_{xy}	Shear stress in face x along yy direction	$[Pa]$

τ_{yz}	Shear stress in face y along zz direction	$[Pa]$
τ_{zx}	Shear stress in face z along xx direction	$[Pa]$
$\phi_i(x)$	Shape function	
Ω	Function domain	
$\boldsymbol{\mathcal{L}}$	Differential operator	

Chapter 1

Introduction

An analysis of propagation of errors by John von Neumann and Herman Goldstine, published in 1947 [1], is generally considered the first work on modern numerical analysis. Seventy years have passed, and with the introduction of digital computers, the complexity of the calculations increased [2].

1.1 Numeric methods in engineering

1.1.1 Finite Difference method (FDM)

For a long time, engineering and physics have been using numerical calculations to solve their problems [1].

The reason behind this is the need to approximate solutions to differential equations that: either do not have an analytic formula for the solution; or the formula is very complex to be solved.

One of the most frequently used methods in the literature, is the Finite difference method (FDM). This method replaces the derivatives in the differential equations with finite difference quotients (or expands the function in Taylor series), creating large but finite algebraic systems. These systems can easily be solved with a computer [3, 4].

1.1.2 Finite Element method (FEM)

In the last decades, the Finite Element Method (FEM) evolved to become the most used numerical methods, being applied to several and distinct engineering and science fields. The essence of a finite element solution is that, a governing algebraic equation is established and solved, and its most distinctive feature is the division of a considered domain into a set of subdomains, called finite elements [3, 5, 6].

1.2 Meshless methods

FEM has been developed through the years, to be capable of making different types of analysis (from static and dynamic analysis, to fluid flows, etc.). However, besides the satisfactory results obtained with the FEM, in recent years some disadvantages become

notorious. One of those disadvantages is the loss of accuracy when handling large deformations [7].

Also the analysis of crack propagation in fatigue processes and interface propagation in casting processes, originates discontinuities that may not be align with the original mesh lines. Therefore, methods that rely on an underlying mesh structure (FDM; FEM; Finite Volume Method (FVM)) are not well suited to the analysis of these problems. The so-called Meshless Methods (MMs) or Meshfree methods (MFree), attempt to overcome those issues, by eliminating (completely or partially) the dependency of the mesh [8].

1.3 Shape Functions

Meshless methods use two types of shape functions: approximation functions and interpolation functions.

The first meshless methods used approximation functions and the background integration scheme was nodal dependent; the influence domain was easier to implement and the produced solution was smoother [9].

1.3.1 Approximation functions

In the group of approximation functions one of the first numerical methods was the Diffuse Element Method (DEM) [10], which uses the moving least squares approximants (MLS) [11] to construct the shape functions. MLS was originally proposed for smoothing and interpolating scattered data. Belytschko introduced some key features in the DEM, to increase its accuracy, creating the Element Free Galerkin Method (EFGM) [12], one of the most popular meshless methods.

One of the oldest methods is, the Smoothed Particle Hydrodynamics (SPH) [13, 14]. This method was created to study problems in astrophysics and later in fluid dynamics [15–18]. SPH is also in the basis of the Reproducing Kernel Particle Method (RKPM) [19].

Meshless Local Petrov-Galerkin Method (MLPG) [20, 21] is another very popular method, created to solve linear potential problems. This method is in the basis of the Method of the Finite Spheres (MFS) [22], which can be viewed as a special case of the MLPG.

The Finite Point Method (FPM) was proposed to construct the basis functions through a local Taylor expansion. This method was created to solve convection-diffusion and fluid flow problems [23, 24].

Radial Basis Function Method (RBFM) was used first for interpolation of geographical scattered data [25, 26] and later to the analysis of differential equations [27–30].

1.3.2 Shape functions properties

Shape functions are required to satisfy the *partition of unity property*,

$$\sum_{i=1}^{n} \phi_i(x) = 1 \tag{1.1}$$

in order to be able to produce rigid motion of the problem domain. Besides this property, shape functions should satisfy (but are not required to) the *linear field reproduction*,

$$\sum_{i=1}^{n} \phi_i(\mathbf{x}_i)\mathbf{x}_i = \mathbf{x} \tag{1.2}$$

This allows the shape function to pass the standard patch test, often used in finite elements for testing purposes. Shape functions that fail the patch test, can be used if they converge to a solution.

One of the most important conditions that a shape function preferable satisfies is the *delta Kronecker property*. A shape function with this property allows the use of a simple procedure to impose essential and natural boundary conditions. Since the interpolation functions possess this property in opposition to the approximation functions, these test functions are easy to use [7].

$$\phi_i(\mathbf{x}_j) = \delta_{ij} = \begin{cases} 1 & (i = j) \\ 0 & (i \neq j) \end{cases} \qquad i, j = 1, \cdots, n \tag{1.3}$$

1.3.3 Interpolation functions

In the group of interpolation functions it is important to refer the Point Interpolation Method (PIM), that uses properly scattered points for the problem domain [31]. The Point Assembly Method (PAM) also uses the scattered points for the problem domain [32].

Radial Point Interpolation Method (RPIM) unlike the previous, uses Radial Bases Functions (RBFs) to construct the shape functions [33–35].

Meshless Finite Element Method (MFEM), changes the FEM to transform it into a meshless method, thus retaining the advantages of the FEM [36].

Natural Neighbour Finite Element Method (NNFEM) uses the Natural Neighbor Interpolant in FEM, by introducing several modifications to both methods [37, 38].

Other method that uses the Natural Neighbour concept is the Natural Element Method (NEM) [38–43].

Recently, the Natural Neighbour Radial Point Interpolation Method (NNRPIM) was developed, combining the NEM with the RPIM [44].

1.4 Natural Neighbour Radial Point Interpolation Method

Natural Neighbour Radial Point Interpolation Method (NNRPIM) is a recent developed meshless method [44], which results from the combination of the Natural Neighbours geometric concept with the Radial Point Interpolators (RPI).

RPI have its origin in the Point Interpolators (PI), which use radial basis functions instead of polynomials, to overcome possible singularity associated with meshless methods, based only on polynomials. Furthermore, the RPI functions possess the *delta Kronecker property*, and use an influence-domain, generating banded stiffness matrices, more adequate for complex problems [33].

In the NNRPIM, the radial basis functions are enhanced, for performance purposes [9].

The Natural Neighbours concept, uses the Voronoï diagram [45] to divide the domain into cells. These cells are created from an unstructured set of nodes. This way, NNRPIM replaces the influence-domain concept by the influence-cell concept.

The governing differential equation used is the Galerkin weak form. The integration is carried out using the Gaussian quadrature. The integration mesh is created, resorting to the Delaunay tessellation [46].

Since the Delaunay tessellation is the dual graph of the Voronoï diagram, the integration mesh is, as well as the influence-cells, node dependently only. The total dependency of the nodal mesh makes NNRPIM one of the "truly" meshless methods.

Through the years, NNRPIM has been extended to many fields in computational mechanics. The previous works include:

- Static analysis of isotropic and orthotropic plates [47];
- Functionally graded material plate analysis [48];
- 3D Shell-like approach for laminated plates and shells [49, 50];
- Dynamic analysis [51–54];
- Large deformation enhanced analysis [55, 56];
- Bone tissue remodeling analysis [57].

1.5 Contact mechanics

Contact is one of the most important problems in many engineering fields, such as civil and mechanical engineering. These problems are also some of the most difficult to simulate, due to the nonlinearities in the mathematical model.

Many known researchers (Da Vinci, Amontons, Newton and Coulomb) have investigated frictional contact problems in the past. Their works shared the assumption of rigid bodies [58, 59].

The most notable researcher of all was Hertz, who solved the contact problem of two elastic bodies with curved surfaces [60], which is considered a milestone in the field of contact mechanics.

Several other authors followed Hertz's work, studying contact problems with elastic bodies, under different circumstances [61]. Examples of these works can be found in [62] and [63].

Unfortunately, only few contact problems can be solved analytically, therefore, for complex geometries, numerical methods must be used. Along these, FEM has been most widely used [61].

Contact problems are computationally demanding, even for the simplest constitutive relations used. They suffer from nonlinearity and non-smoothness; susceptibility to instability and potential ill-conditioning.

Besides this, the boundary conditions of the considered bodies, are not known prior to the analysis, because it depend on the solution variables. Therefore, a contact detection algorithm (namely searching) is needed, increasing computational cost [64, 65].

Early works devoted to searching contact use a master-slave contact algorithm. This and other general and efficient searching algorithms can be found in [61].

The early works on contact problems using FEM, focus on frictionless linearly elastic bodies considering small deformations. The first friction treatments were also limited to elastic response considering small deformations. The need for capable characterizations of the contact problem, lead to several proposed implementations incorporating friction [66].

Unfortunately, it is very difficult to model friction because it is related to many factors, among others the normal contact force, the smoothness of the material involved, and contaminants on contacting surface including lubricants, etc. For a long time, the classical Coulomb friction law has been used to model friction. Its deficiency in both physical aspects and mathematical aspects has been discussed, in which non-classical friction is considered [61].

Some of the previous cited works, share the use of incremental analysis to control nonlinearities due to contact and to model friction effects [67].

In FEM [68–74], contact bodies are approximated by collections of finite elements, and contact boundaries by collections of polygons. The bodies may have complex geometries.

Two formulations are used: the variational inequality and the variational equality.

The variational inequality is mathematically rigorous, and is widely used. Some examples of this formulation can be consulted in [61].

While many authors prefer a variational inequality, many others researchers prefer to work straightforwardly with a variational equality [61].

An important topic when solving contact problems numerically is the conversion of variational inequalities into equalities. The proposed techniques are divided between the Lagrange Multipliers and the Penalty Method. The advantages and disadvantages of both techniques can be consulted in [66].

Based on the basic methods, other constraint methods, such as the augmented Lagrangian method and the perturbed Lagrangian method were derived and applied [61].

Depending on the specific application, contact problems may be solved using either explicit or implicit schemes for time integration of the global equations [66].

In early studies, contact bodies were often discretized in a way that possible contact nodes could only contact with other finite element nodes, the so called node-to-node interface model. This now seems inadequate, even in the case of small displacements. Therefore a more general node-to-segment interface model is preferred, and is peremptory for problems with large displacements and large rotations [66].

In terms of Meshless methods, unlike the FEM, there is not some sort of algorithm that has been thoroughly applied through the years. The meshless method topic is relative new, and in the last years has been used with different algorithms previous referred, in an effort to develop stable and capable algorithms for different problems, that can actually be a better alternative to other numerical methods. Meshless methods are still in a development stage, where rather than persist with one method and extensively develop it, the scientific community tries to diversify as much as possible to test the most number of valid solutions.

1.6 Signorini's Problem

One of the bases for many generalizations is the Signorini problem [75]. This problem describes the contact of a linearly elastic body with a rigid frictionless foundation. The solution to the classical Signorini problem is the solution of a variational inequality that appears naturally from the principle of virtual work [67].

1.7 Motivation and objectives

The motivation to embrace this work by the author comes from three essential reasons.

The first reason that comes into play is the interest of the author in programming. The interest does not lie only in the programming part, but also in the problem object of programming.

Second, is the curiosity about the contact problems, mainly because of their importance in mechanics, but also for their inherent complexity.

The last reason is that from the proposed works in the meshless area, it was the most attractive one.

The objectives of this work are very simple:

- Mainly to extend the contact problem to a meshless method, the NNRPIM (Natural Neighbour Radial Point Interpolator Method) developed at FEUP;
- Develop a simple algorithm spending reduced resources in terms of computational costs;
- Run some simple examples, without friction, considering a large deformation approximation and different boundary shapes that can either be static or dynamic.

The program is written in MATLAB® R2012a from MathWorks®.

1.8 Thesis organization

This thesis is organized in five chapters as follows:

1. **Introduction -** An overview of the numerical methods is presented, with special attention to the meshless ones. The used program is briefly presented and the state of the art of contact analysis is shown. Finally the motivation to embrace this thesis and its objectives are described.
2. **Meshless method -** The used meshless method is presented in detail. Along with the method, the needed solid mechanical fundamentals are presented as well.
3. **Incursion on Contact -** The implemented MATLAB® algorithm is described.
4. **Numerical Examples -** All the examples created are shown here, from linear and non-linear examples to the ones with contact.
5. **Conclusions and future works -** The most important conclusions are compiled and, the future developments presented.

Chapter 2

Meshless method

Numerical methods can be divided in three parts: the field interpolation or approximation (shape functions); the governing differential equation and the integration [9].

In general, a meshless method follows the same rule. Initially the problem domain is discretized using only nodes. The distribution of the nodes, and their quantity, are related with the accuracy of the results and the computational time. Critical areas should have more nodes, however an unbalanced distribution of nodes can deteriorate the results.

The formulation of the various meshless methods can be divided in two groups: the strong form solution and the weak form solution.

The strong form solution uses the partially differential equation, while the weak form solution uses either a variational method or a weighted residual method. There are several forms of variational methods and weighted residual methods, being the last a more general and powerful mathematical tool [7, 9].

Obtaining the exact solution using a strong form system is ideal, however normally, it is very difficult for complex problems. In opposition, equations obtained from the weak form solution, are more stable, and can provide much better results. This is why so many authors prefer the weak form over the strong one [7].

As in FEM, the integration of the weak form cannot be easily evaluated analytically [76].

Therefore, it is commonly used a "Quadrature" (evaluation of an integral numerically), being the most well-known the Gaussian quadrature [77].

One way of applying the Gaussian quadrature is, the creation of a background mesh, covering the entire problem domain, composed by integration points, which have a respective influence area and weight. Nevertheless, this integration mesh is generally nodal independent, making the meshless method that uses it, not completely mesh free, as the denomination (meshless) implies [9].

There are, however, some integration schemes, often used, like the Nodal integration method [78, 79] and the Point Collocation method [80, 81], were the integration point is the node itself. The influence area is the node influence domain, and the weight is the node influence volume. These methods are "truly" meshless methods, because the integration mesh is the nodal mesh.

So, in most cases, the next step is the construction of the integration mesh. This mesh usually is larger than the nodal mesh.

Following the integration points, the nodal connectivity is imposed. FEM uses the concept of elements to do this, while meshless methods (which do not have elements) define areas or volumes around an interest point, making all the nodes inside that area or volume belong to the influence-domain of the considered interest point. In most cases the interest points are the integration points.

The influence-domain size affect the quality of the results, therefore, is recommended that they share the same number of nodes. Their size should be defined in proportion with the node density around the interest point.

In a meshless method whose interest points are the integration points, the field variables can be approximated or interpolated, using the field results of the nodes inside the influence-domain. For example, for the displacements in interest point I, $\mathbf{u}_I = (u; v)$ one can state

$$\mathbf{u}_I = \sum_{j=1}^{n} \phi_j \mathbf{u}_j \tag{2.1}$$

where n is the number of nodes inside the influence-domain, ϕ_j is the approximation / interpolation function value for the node j belonging to the influence domain of interest point I, and $\mathbf{u}_j$ is the displacements vector of the node j.

The system of equations is then created, according to the respective formulation. The system is solved with an appropriate method. The weak form of Galerkin used in this work is solved with the Gauss Elimination method [9].

2.1 Natural Neighbours

The NNRPIM uses the concept of Natural Neighbours to connect the nodes and construct the integration mesh.

Natural Neighbours mathematical concept was firstly introduced by Sibson for data fitting and smoothing purposes [82]. The Natural Neighbours can be applicable to D dimensional space.

The Voronoï diagram of a set **N** of N distinct nodes,

$$\mathbf{N} = \{n_1, n_2, \ldots, n_N\} \in \mathbb{R}^2 \tag{2.2}$$

is the partition of the domain defined by **N** in sub-regions, V_I, so that any point in the interior of V_I is closer to n_I than any other node n_J, where $n_J \in \mathbf{N} \wedge J \neq I$.

These sub-regions V_K are the Voronoï Cells, which together form the Voronoï diagram. The Voronoï cell is defined as,

$$V_I = \{\mathbf{x} \in \mathbb{R}^2 : \mathbf{E}_n(\mathbf{x}, \mathbf{x}_I) < \mathbf{E}_n(\mathbf{x}, \mathbf{x}_J) \quad \forall \quad J \neq I\} \tag{2.3}$$

where $E_n(x, x_I)$is the Euclidean metric norm, i.e., the distance between an interest point and a node I with coordinates **x** and $\mathbf{x}_I$ (see Figure 2.1).

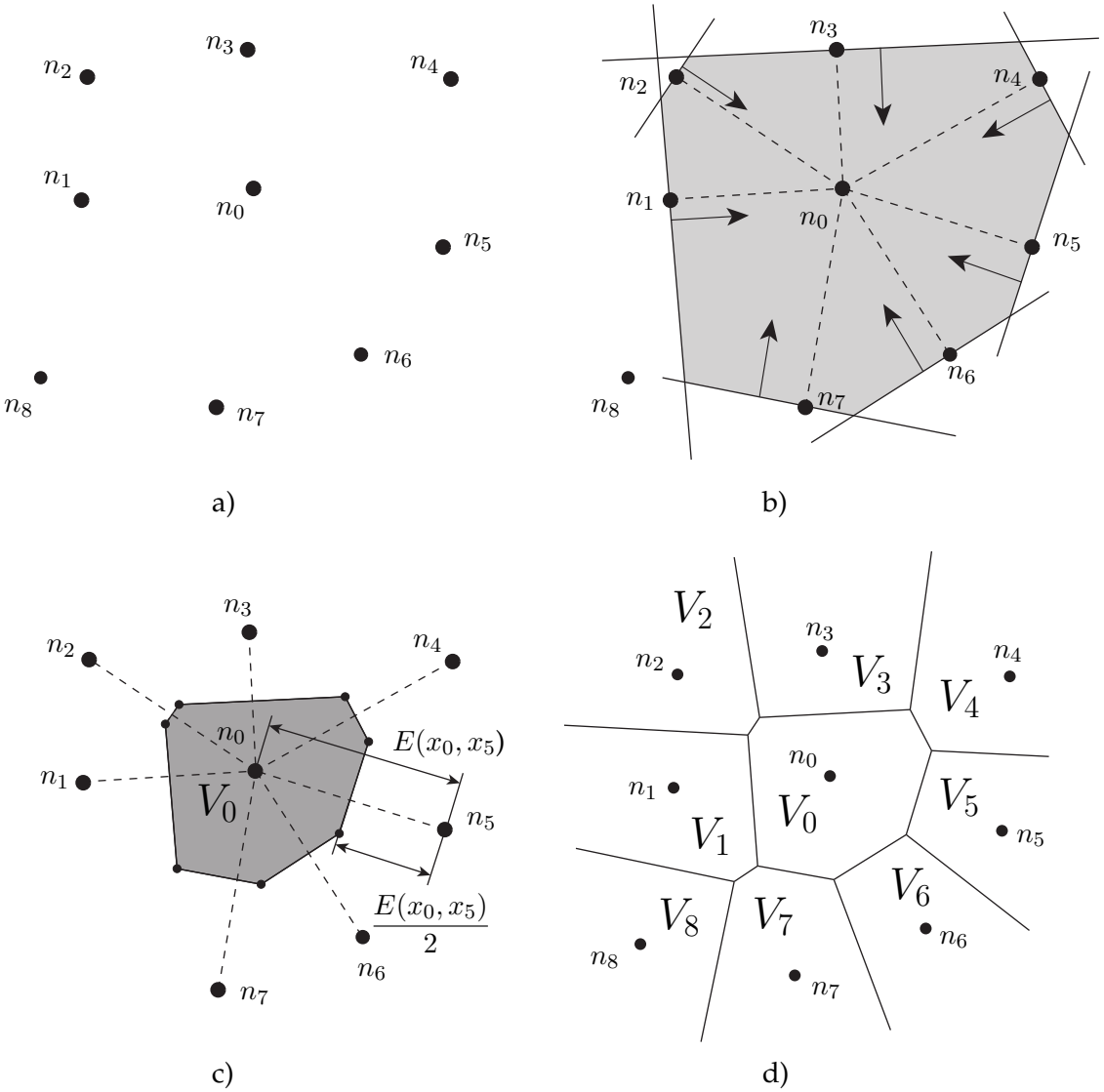

Figure 2.1: Schematic steps in the construction of the Voronoï diagram: a) Indiscriminate node set; b) Determination of the neighbours; c) Voronoï cell; d) Voronoï diagram.

The construction of the Voronoï cell starts with a set of nodes. For each node, it are defined domains whose limits are the line that intersects the potential neighbour node J, and is normal to the line that connects this node, to the interest node or central node. The intersection of the domains permits to obtain the neighbouring nodes, which are by definition, the nodes at the perimeter of the final polygonal. The Voronoï cell is finally obtained, by applying a homothetic transformation to the final domain, with a factor of 0,5. This procedure is repeated for all the nodes, originating the Voronoï diagram.

In the NNRPIM, the Voronoï diagram is used to create the influence-cells, which replaces the influence-domain in the imposition of nodal connectivity.

To construct an integration mesh completely nodal dependent, the Delaunay tessellation is used (see Figure 2.2). Delaunay tessellation is the dual graph of the Voronoï diagram, is constructed by connecting the nodes whose Voronoï cells share common boundaries.

Delaunay tessellation has the property of "empty circumcircle" criterion [83].

This property states that if a set of nodes forms a Delaunay triangle, then the circumcircle formed by the triangle contains only the nodes that are the vertices of the triangle. Also the centre of the circle is a vertex of the Voronoï cell [44].

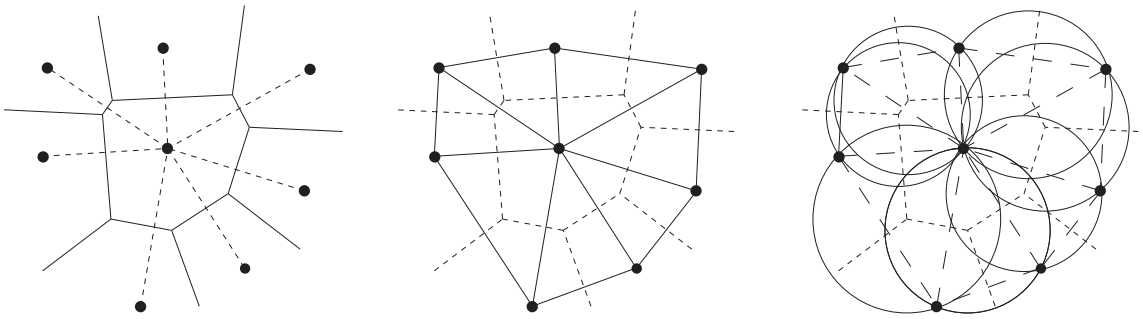

Figure 2.2: a) Voronoï diagram; b) Delaunay tessellation; c) Natural Neighbour circumcircles.

2.1.1 Influence-cells and Nodal Connectivity

It is important that all the influence domains in the problem have a similar number of nodes. Inhomogeneous influence-domains can affect the results, therefore, the use of fixed and regular shaped influence-domains are not appropriate. Also searching for enough nodes inside a fixed area (as in early works using the RPI [32–34, 84]) lead to variations in size and shape influencing the final solution and performance of the method.

The NNRPIM, similar to other meshless methods, impose the nodal connectivity by overlapping the influence-domains, which in the case of the NNRPIM are the influence-cells.

There are two distinct types of influence-cells: first degree cells and second degree cells.

In the first degree cells (Figure 2.3), only the first natural neighbours are considered, while in the second degree cells (Figure 2.4), additionally, also the natural neighbours of the first ones are used.

Through this work, the second degree cells (Figure 2.4) will be used, since it provides more accurate results [44].

2.1.2 Numerical Integration

NNRPIM uses the Gaussian quadrature to integrate the governing differential equation. The location of the integration points is established resorting to the Voronoï diagram and the Delaunay tessellation.

Intersecting the Voronoï diagram with the Delaunay tessellation, divides each Voronoï cell in small areas (sub-cells) see Figure 2.5.

A node n_I with J neighbour nodes, forming a V_I Voronoï cell, have J sub-cells, S_{Ii}. The area of the cell A_{V_I} is obtained with the area of the sub-cells $A_{S_{Ii}}$, using

$$A_{V_I} = \sum_{i=1}^{n} A_{S_{Ii}}, \forall A_{S_{Ii}} \geq 0 \tag{2.4}$$

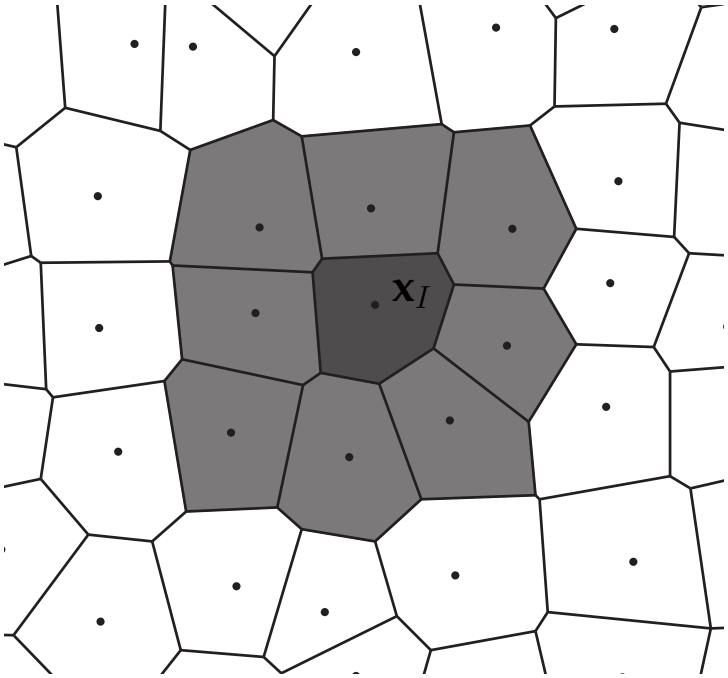

Figure 2.3: First degree cells.

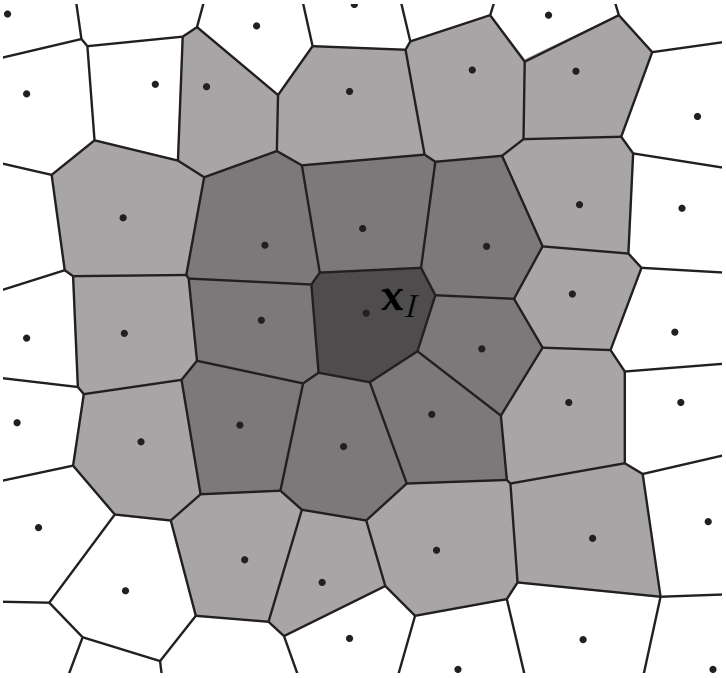

Figure 2.4: Second degree cells.

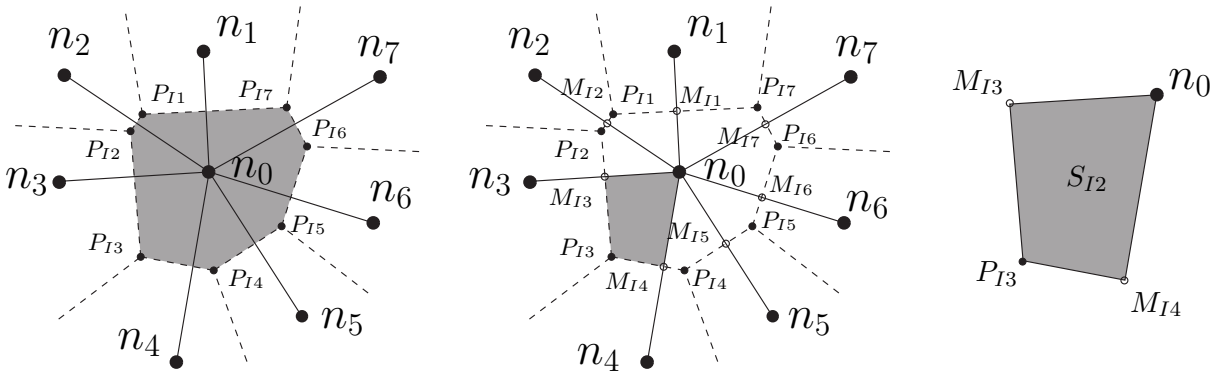

Figure 2.5: a) Voronoï cell intercepted by the Delaunay diagram; b) Generated sub cell (quadrilateral); c) Sub cell.

The integration scheme can be of order 0 or order 1. In the case of order 0, one integration point is placed in the geometric centre of the sub-cell defined above. Its weight is the area of the sub-cell S_{Ii}. The geometric centre is defined as

$$X_I = \frac{1}{4}\sum_{i=1}^{4} X_i \tag{2.5}$$

In the case of order 1, the sub-cell is divided in quadrilateral shapes, and like in the order 0, an integration point is placed in the geometric centre of the new shapes [9]. The two schemes are shown in Figure 2.6.

In this work is used the integration of order 0, since it presents a lower computational cost, without prejudice to the solution

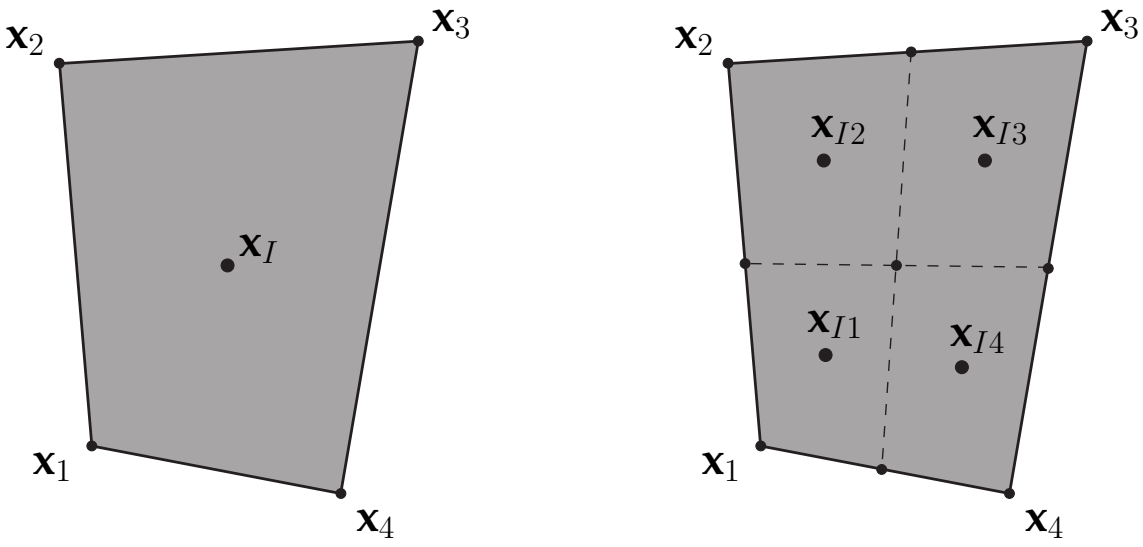

a) b)

Figure 2.6: a) Integration scheme of order 0; b) Integration scheme of order 1.

2.2 Radial Point Interpolators

In the NNRPIM, the interpolation function passes through all the nodes. Consider a function $u(x_I)$ that uses a radial basis function (RBF), defined in the domain Ω and discretised by a set of nodes, only the nodes within the influence-cell of the point of interest x_I are considered on $u(x_I)$. At the point of interest, the value of the function is defined by,

$$\mathbf{u}(\mathbf{x}_I) = \sum_{i=1}^{n} R_i(\mathbf{x}_I)a_i(\mathbf{x}_I) + \sum_{j=1}^{m} p_j(\mathbf{x}_I)b_j(\mathbf{x}_I) = \mathbf{R}^T(\mathbf{x}_I)\mathbf{a}(\mathbf{x}_I) + \mathbf{p}^T(\mathbf{x}_I)\mathbf{b}(\mathbf{x}_I) \tag{2.6}$$

$R_i(\mathbf{x}_I)$ is the RBF, and n is the number of nodes in the influence-cell of $\mathbf{x}_I$. $p_j(\mathbf{x}_I)$ defines the monomials of the polynomial basis, and m is the basis polynomial number. $a_i(\mathbf{x}_I)$ and $b_j(\mathbf{x}_I)$ are non-constant coefficients of $R_i(\mathbf{x}_I)$ and $p_j(\mathbf{x}_I)$ respectively. The vectors are defined as follows:

$$\mathbf{R}(\mathbf{x}_I) = \{R_1(\mathbf{x}_I)\ R_2(\mathbf{x}_I) \cdots R_n(\mathbf{x}_I)\}^T \tag{2.7}$$

$$\mathbf{p}(\mathbf{x}_I) = \{p_1(\mathbf{x}_I)\ p(\mathbf{x}_I) \cdots p_m(\mathbf{x}_I)\}^T \tag{2.8}$$

$$\mathbf{a}(\mathbf{x}_I) = \{a_1(\mathbf{x}_I)\ a_2(\mathbf{x}_I) \cdots a_n(\mathbf{x}_I)\}^T \tag{2.9}$$

$$\mathbf{b}(\mathbf{x}_I) = \{b_1(\mathbf{x}_I)\ b_2(\mathbf{x}_I) \cdots b_n(\mathbf{x}_I)\}^T \tag{2.10}$$

In order to obtain a more stable function, the m should be smaller than n. The reason to add polynomials into the basis function is to ensure the consistency of the RPI functions. However, it was proved that the RPI do not require a polynomial basis function to pass the standard patch test [44, 47].

The variable in the RBF is the distance r_{Ii} between the relevant node x_I and the neighbor node x_i. This distance is defined in a two dimensional space as

$$r_{Ii} = \sqrt{(x_I - x_i)^2 (y_I - y_i)^2} \tag{2.11}$$

There are several RBFs. NNRPIM uses the Multiquadratic (MQ), proposed by Hardy [25]. MQ-RBF is defined as:

$$R(r_{Ii}) = (r_{Ii}^2 + C_s^2)^P \tag{2.12}$$

being P and C_S two shape parameters that need to be optimized. This was already done in [9] and the optimal values are

$$\begin{aligned} C_s &= 0,0001 \\ P &= 1,0001 \end{aligned} \tag{2.13}$$

These values are used throughout this work.

Like the RBF, several polynomials are available for 2D analysis:

$$Null\ basis\ (m = 0) : \mathbf{p}_I^T(\mathbf{x}) = \{1\} \tag{2.14a}$$
$$Constant\ basis\ (m = 1) : \mathbf{p}_I^T(\mathbf{x}) = \{1\} \tag{2.14b}$$
$$Linear\ basis\ (m = 3) : \mathbf{p}_I^T(\mathbf{x}) = \{1 \quad x \quad y\} \tag{2.14c}$$
$$Quadratic\ basis\ (m = 6) : \mathbf{p}_I^T(\mathbf{x}) = \{1 \quad x \quad y \quad x^2 \quad xy \quad y^2\} \tag{2.14d}$$

In this work only the constant basis is used.

To obtain an unique solution, the polynomial basis has to satisfy a requirement:

$$\sum_{i=1}^{n} p_j(\mathbf{x}_i) a_i(\mathbf{x}_i) = 0 \ \Leftrightarrow\ \mathbf{p}^T(\mathbf{x}_i)\mathbf{a}(\mathbf{x}_i) = 0 \tag{2.15}$$

were $j = \{1, 2, \cdots, m\}$. Combining equation (2.6) with equation (2.15), one can write

$$\begin{Bmatrix} \mathbf{u}_S \\ \mathbf{0} \end{Bmatrix} = \begin{bmatrix} \mathbf{R}_Q & \mathbf{P}_m \\ \mathbf{P}_m^T & \mathbf{0} \end{bmatrix} \begin{Bmatrix} \mathbf{a} \\ \mathbf{b} \end{Bmatrix} = \mathbf{G} \begin{Bmatrix} \mathbf{a} \\ \mathbf{b} \end{Bmatrix} \tag{2.16}$$

$\mathbf{u}_S$ is defined by

$$\mathbf{u}_S = \{u_1, u_2, \cdots, u_n\}^T \tag{2.17}$$

The moment matrix $\mathbf{R}_Q$ of the RBF is

$$\mathbf{R}_Q = \begin{bmatrix} R(r_{11}) & R(r_{12}) & \cdots & R(r_{1m}) \\ R(r_{21}) & R(r_{22}) & \cdots & R(r_{2m}) \\ \vdots & \vdots & \ddots & \vdots \\ R(n_{I1}) & R(r_{n2}) & \cdots & R(r_{nm}) \end{bmatrix} \tag{2.18}$$

The moment matrix $\mathbf{P}_m$ of the polynomial basis is defined as

$$\mathbf{P}_m = \begin{bmatrix} P_1(\mathbf{x}_1) \\ P_1(\mathbf{x}_2) \\ \vdots \\ P_1(\mathbf{x}_n) \end{bmatrix} \tag{2.19}$$

By solving equation (2.16)

$$\begin{Bmatrix} \mathbf{a} \\ \mathbf{b} \end{Bmatrix} = \mathbf{G}^{-1} \begin{Bmatrix} \mathbf{u}_s \\ \mathbf{0} \end{Bmatrix} \tag{2.20}$$

Substituting in equation (2.6), it is achieved

$$\mathbf{u}(\mathbf{x}_I) = \{\mathbf{R}^T(\mathbf{x}_I), \mathbf{p}^T(\mathbf{x}_I)\}\, \mathbf{G}^{-1} \begin{Bmatrix} \mathbf{u}_S \\ \mathbf{0} \end{Bmatrix} = \phi(\mathbf{x}_I)\mathbf{u}_S \tag{2.21}$$

The interpolation function, $\phi(x_I)$ on interest point x_I is defined as

$$\phi(\mathbf{x}_I) = \{\mathbf{R}^T(\mathbf{x}_I), \mathbf{p}^T(x_I)\}\, \mathbf{G}^{-1} = \{\phi_1(\mathbf{x}_I), \phi_2(\mathbf{x}_I), \cdots, \phi_n(\mathbf{x}_I)\} \tag{2.22}$$

The partial derivative of $\phi(x_I)$ in order to a variable ξ is obtained with

$$\phi(\mathbf{x}_I) = \{\mathbf{R}^T(\mathbf{x}_I), \mathbf{p}^T(x_I)\}\, \mathbf{G}^{-1} = \{\phi_1(\mathbf{x}_I), \phi_2(\mathbf{x}_I), \cdots, \phi_n(\mathbf{x}_I)\} \tag{2.23}$$

The partial derivative of the MQ-RBF in order to the same variable is defined by

$$\phi_\xi(\mathbf{x}_I) = \{\mathbf{R}_\xi^T(\mathbf{x}_I), \mathbf{p}_\xi^T(\mathbf{x}_I)\}\, \mathbf{G}^{-1} \tag{2.24}$$

A more detailed description on the RPI formulation can be found in [9].

2.2.1 Properties of the RPI function

Many properties make the RPI attractive [7].

One of the most important is the *delta Kronecker property*,

$$\phi_i(\mathbf{x}_j) = \delta_{ij} = \begin{cases} 1\,(i=j) \\ 0\,(i\neq j) \end{cases} \quad i,j = 1,\cdots,n \tag{2.25}$$

for easier imposition of essential and natural boundary conditions. The RPI function also possess the *partition of unity property*,

$$\sum_{i=1}^{n} \phi_i(\mathbf{x}_i) = 1 \tag{2.26}$$

as long as the constant is included in the polynomial basis, and the interpolation function possesses reproducing properties (equation (2.27)). Therefore if at least the first order monomial is included in the polynomial basis.

$$\sum_{i=1}^{n} \phi_i(\mathbf{x}_i)\mathbf{x}_i = \mathbf{x} \tag{2.27}$$

If $\mathbf{G}$ is invertible, $\phi(\mathbf{x}_I)$ depends uniquely on the distribution of the nodes.

By using only the nodes within the influence-cell, the interpolation function has a compact support, which creates sparse and banded system matrices [9].

2.3 Solid Mechanics implementation

2.3.1 Fundamental equations

Consider a solid infinitesimal volume with dimensions $dx\ dy\ dz$. The Cartesian stress components on the infinitesimal volume can be organized in the tensor form,

$$\boldsymbol{\sigma} = \begin{bmatrix} \sigma_{xx} & \tau_{xy} & \tau_{xz} \\ \tau_{yx} & \sigma_{yy} & \tau_{yz} \\ \tau_{zx} & \tau_{zy} & \sigma_{zz} \end{bmatrix} \wedge \boldsymbol{\sigma}_{ij} = \boldsymbol{\sigma}_{ji} \quad if \quad i \neq j \tag{2.28}$$

The tensor could be represented in a vector form,

$$\boldsymbol{\sigma} = \{\sigma_{xx} \quad \sigma_{yy} \quad \sigma_{zz} \quad \tau_{xy} \quad \tau_{yz} \quad \tau_{zx}\}^T \tag{2.29}$$

To each one of the stress components, corresponds a deformation component

$$\boldsymbol{\epsilon} = \{\epsilon_{xx} \quad \epsilon_{yy} \quad \epsilon_{zz} \quad \gamma_{xy} \quad \gamma_{yz} \quad \gamma_{zx}\}^T \tag{2.30}$$

The components of the deformation tensor are defined as

$$\begin{aligned} \epsilon_{xx} &= \frac{\delta u}{\delta x} \quad \gamma_{xy} = \frac{\delta u}{\delta y} + \frac{\delta v}{\delta x} \\ \epsilon_{yy} &= \frac{\delta v}{\delta y} \quad \gamma_{yz} = \frac{\delta v}{\delta z} + \frac{\delta w}{\delta y} \\ \epsilon_{zz} &= \frac{\delta w}{\delta z} \quad \gamma_{zx} = \frac{\delta w}{\delta x} + \frac{\delta u}{\delta z} \end{aligned} \tag{2.31}$$

were u, v and w are the displacements along directions xx, yy and zz respectively. The displacements can be stated as follows

$$\boldsymbol{\epsilon} = \boldsymbol{\mathcal{L}}\mathbf{u} \tag{2.32}$$

were for 2D analysis the differential operator $\mathcal{L}$ is

$$\boldsymbol{\mathcal{L}} = \begin{bmatrix} \frac{\partial}{\partial x} & 0 \\ 0 & \frac{\partial}{\partial y} \\ \frac{\partial}{\partial y} & \frac{\partial}{\partial x} \end{bmatrix} \quad e \quad \mathbf{u} = \begin{Bmatrix} u \\ v \end{Bmatrix} \tag{2.33}$$

2.3.2 Constitutive relations

In linear elasticity the stress and the strain is related through the generalized Hook's law

$$\boldsymbol{\sigma} = \mathbf{c}\boldsymbol{\epsilon} \tag{2.34}$$

being **c** the material constants matrix.

In a 3D space and for an orthotropic material, the inverse of matrix **c** is defined by,

$$\mathbf{c}^{-1} = \begin{bmatrix} \frac{1}{E_x} & -\frac{\nu_{yx}}{E_y} & -\frac{\nu_{zx}}{E_z} & 0 & 0 & 0 \\ -\frac{\nu_{xy}}{E_x} & \frac{1}{E_y} & -\frac{\nu_{zy}}{E_z} & 0 & 0 & 0 \\ 0 & 0 & \frac{1}{E_z} & 0 & 0 & 0 \\ 0 & 0 & 0 & \frac{1}{G_{xy}} & 0 & 0 \\ 0 & 0 & 0 & 0 & \frac{1}{G_{yz}} & 0 \\ 0 & 0 & 0 & 0 & 0 & \frac{1}{G_{zx}} \end{bmatrix} \tag{2.35}$$

For plane stress analysis, the stress along zz direction is considered null. The inverse of **c** matrix for 2D problems considering an isotropic material and plane stress is

$$\mathbf{c}^{-1} = \begin{bmatrix} \frac{1}{E} & -\frac{\nu}{E} & 0 \\ -\frac{\nu}{E} & \frac{1}{E} & 0 \\ 0 & 0 & \frac{1}{G} \end{bmatrix} \tag{2.36}$$

For plane strain analysis, the strain along zz direction is considered null. The inverse of **c** matrix for 2D problems considering an isotropic material and plane strain is

$$\mathbf{c}^{-1} = \begin{bmatrix} \frac{(1+\nu)(1-\nu)}{E} & -\frac{(1+\nu)(-\nu)}{E} & 0 \\ -\frac{(1+\nu)(-\nu)}{E} & \frac{(1+\nu)(1-\nu)}{E} & 0 \\ 0 & 0 & G \end{bmatrix} \tag{2.37}$$

2.3.3 Galerkin weak form

Ideally, it should be possible to achieve the exact solution, by means of the strong form system equations, which corresponds to the partial differential system governing the studied problem.

In several engineering problems, this is a difficult task. Many authors prefer to use weak formulations, which permit to obtain stable algebraic system of equations and accurate results.

The NNRPIM uses a variational method, the Galerkin weak form [85], which is based on the energy principle.

The solution, is the one that minimizes the Lagrangian functional L,

$$L = T - U + W_f \tag{2.38}$$

were T is the kinetic energy, U the strain energy and W_f the work produced by external forces.

The kinetic energy is obtained with

$$T = \frac{1}{2} \int_{\Omega} \rho \dot{\mathbf{u}}^T \dot{\mathbf{u}} d\Omega \tag{2.39}$$

were $\dot{\mathbf{u}}$ is the velocity, ρ the mass density and Ω is the solid volume.

The strain energy for elastic materials is defined by,

$$U = \frac{1}{2} \int_{\Omega} \boldsymbol{\epsilon}^T \boldsymbol{\sigma} d\Omega \tag{2.40}$$

were $\boldsymbol{\epsilon}$ is the strain vector and $\boldsymbol{\sigma}$ the stress vector.

The work produced by external forces can be presented as

$$W_f = \int_\Omega \mathbf{u}^T \mathbf{b} d\Omega + \int_{\Gamma_t} \mathbf{u}^T \bar{\mathbf{t}} d\Gamma \tag{2.41}$$

were $\mathbf{u}$ is the displacement, $\mathbf{b}$ are the body forces, Γ_t the boundary were the external forces are applied and $\bar{\mathbf{t}}$ the boundary forces themselves.

After the manipulation of equation (2.38) (which can be found in detail in [9]) it is possible to obtain,

$$-\rho \int_\Omega (\delta \mathbf{u}^T \ddot{\mathbf{u}}) d\Omega - \int_\Omega \delta \boldsymbol{\epsilon}^T \boldsymbol{\sigma} d\Omega + \int_\Omega \delta \mathbf{u}^T \mathbf{b} d\Omega + \int_{\Gamma_t} \delta \mathbf{u}^T \bar{\mathbf{t}} d\Gamma = 0 \tag{2.42}$$

which is known as the Galerkin weak form.

If the stress-strain relation $\boldsymbol{\sigma} = \mathbf{c}\boldsymbol{\epsilon}$, is considered along the strain-displacement relation $\boldsymbol{\epsilon} = \boldsymbol{\mathcal{L}}\mathbf{u}$, the equation can be rewritten as

$$\int_\Omega \delta(\mathbf{Lu})^T c(\mathbf{Lu}) d\Omega - \int_\Omega \delta \mathbf{u}^T \mathbf{b} d\Omega - \int_{\Gamma_t} \delta \mathbf{u}^T \bar{\mathbf{t}} d\Gamma + \int_\Omega \rho(\delta \mathbf{u}^T \ddot{\mathbf{u}}) = 0 \tag{2.43}$$

In this work only static analysis is considered, therefore, the fourth term in equation (2.43) disappears [9].

2.4 Discrete System Equation

From the principle of virtual work, using the NNRPIM interpolator trial and test functions, the discrete equations are obtained. The domain is discretized, and the imposition of nodal connectivity between the neighbouring nodes is achieved, with the influence-domain of each node.

The NNRPIM trial function is

$$\mathbf{u}(\mathbf{x}_I) = \sum_{i=1}^{n} \phi_i(\mathbf{x}_I) \mathbf{u}_i \tag{2.44}$$

were $\phi_i(\mathbf{x}_I)$ is the NNRPIM C^∞ interpolation function and $\mathbf{u}_i$ is the nodal displacements vector of the n nodes belonging to the influence-domain of interest node x_I. The NNRPIM interpolation function possess the *delta Kronecker property*.

Following equation (2.44), the test functions are defined as

$$d\mathbf{u}(\mathbf{x}_I) = \sum_{i=1}^{n} \phi_i(\mathbf{x}_I) d\mathbf{u}_i \tag{2.45}$$

being $d\mathbf{u}$ the nodal values for the test function.

2.4.1 Stiffness matrix

The global stiffness matrix is defined by

$$\int_{\Omega} \delta \left[\sum_{I}^{n} \mathbf{B}_I \mathbf{u}_I \right]^T c \left[\sum_{J}^{n} \mathbf{B}_J \mathbf{u}_J \right] d\Omega = \sum_{I}^{n} \sum_{J}^{n} \delta \mathbf{u}_I^T \left[\mathbf{K}_{IJ} \right] \mathbf{u}_J \tag{2.46}$$

were K_{IJ} is the local stiffness matrix and n is the number of interest points. Matrix **B** is the deformable matrix, and is defined for 2D analysis as

$$\mathbf{B} = \begin{bmatrix} \dfrac{\partial \phi_I}{\partial x} & 0 \\ 0 & \dfrac{\partial \phi_I}{\partial y} \\ \dfrac{\partial \phi_I}{\partial y} & \dfrac{\partial \phi_I}{\partial x} \end{bmatrix} \tag{2.47}$$

2.4.2 Force vector

The global nodal force vector is defined by

$$\sum_{I}^{n} \delta \mathbf{u}_I^T \mathbf{f}_I = \delta \mathbf{U}^T \mathbf{F} \tag{2.48}$$

were **F** is the global nodal force vector. The local nodal force $\mathbf{f}_I$ is defined as

$$\mathbf{f}_I = \int_{\Gamma_I} \varphi_I^T \bar{\mathbf{t}} d\Gamma \tag{2.49}$$

2.5 Imposition of the boundary conditions

2.5.1 General method

Since NNRPIM uses interpolation functions, which possess the *delta Kronecker property*, the boundary conditions can be directly imposed. There are two types of boundary conditions: the essential conditions (displacement related); and the natural conditions (force related).

The method used to impose the boundary conditions is the Direct Imposition Method (DIM). It is formulated as follows

$$\bar{u}_i = V, \forall\, V \in \mathbb{R} \tag{2.50}$$

$$\mathbf{K} \begin{cases} K_{ij} = 0, & j = 1, \cdots, n \wedge j \neq i \\ K_{ij} = 1, & j = i \end{cases} \tag{2.51}$$

$$\mathbf{F}\{F_i = V \tag{2.52}$$

were i is the restricted degree of freedom, and V is the imposed displacement.

In terms of contact, only the direction perpendicular to the boundary at any given node is restricted. If it is a static boundary, the imposed displacement is null, otherwise is the displacement of the boundary.

2.5.2 Supports with arbitrary directions

In the analysis of contact problems, it is required to be able to reproduce boundaries with an arbitrary shape. To impose boundary conditions in constant boundaries, the DIM is used directly, since the stiffness matrix is defined in the global coordinate system, and the direction of the degree of freedom to affect, coincides with one of the two global (x, y) directions.

In arbitrary directions, the boundary normal direction does not coincides with one of the global directions, but instead with the local $(x^{'}, y^{'})$ directions, defined as the normal direction $(x^{'})$ and the tangent direction $(y^{'})$ of the boundary in the respective node position - see Figure 2.7. Therefore to apply the DIM directly, the degrees of freedom must be transformed from the global to the local coordinate system.

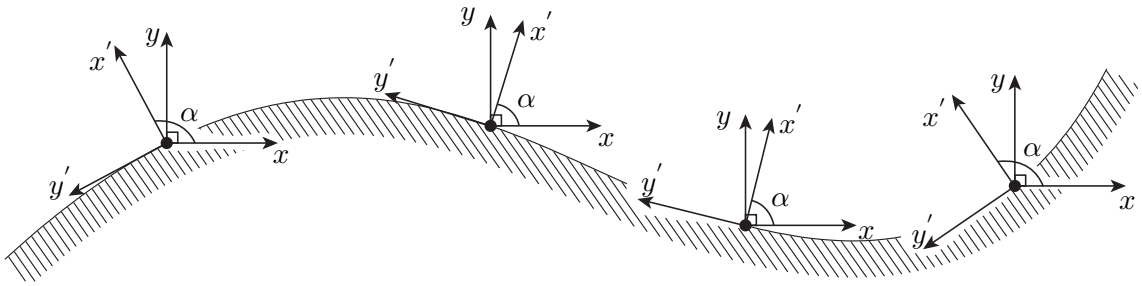

Figure 2.7: Global and local coordinate system for different points in a curved boundary.

This is achieved with the transformation matrix $[\mathbf{T}_{12}]$ as follows

$$[\mathbf{K}^{'}] = [\mathbf{T}_{12}][\mathbf{K}][\mathbf{T}_{12}^{T}] \tag{2.53}$$

$$\{\mathbf{F}^{'}\} = [\mathbf{T}_{12}]\{\mathbf{F}\} \tag{2.54}$$

Then the DIM is applied as before, and the inverse transformation is carried on, so the system is kept in the global reference system.

$$[\mathbf{K}] = [\mathbf{T}_{12}^{T}][\mathbf{K}^{'}][\mathbf{T}_{12}] \tag{2.55}$$

$$\{\mathbf{F}\} = [\mathbf{T}_{12}^{T}]\{\mathbf{F}^{'}\} \tag{2.56}$$

The transformation matrix is the same size as the stiffness matrix and is defined as

$$[\mathbf{T}_{12}] = \begin{bmatrix} [\mathbf{I}] & [\mathbf{0}] & [\mathbf{0}] & [\mathbf{0}] \\ [\mathbf{0}] & [\mathbf{t}_{12}] & [\mathbf{0}] & [\mathbf{0}] \\ \cdots & \cdots & \ddots & \vdots \\ [\mathbf{0}] & [\mathbf{0}] & [\mathbf{0}] & [\mathbf{I}] \end{bmatrix} \tag{2.57}$$

were each sub matrix has the same size as the number of degrees of freedom at each node. $[\mathbf{I}]$ is the identity matrix, and $[\mathbf{t}_{12}]$ is the matrix that transforms the global coordinate system into the local coordinate system of the restricted node.

As so, only the degrees of freedom that are not aligned with the global coordinate system are transformed. Several degrees of freedom, corresponding to various nodes can be transformed simultaneously [86].

Chapter 3

Incursion on Contact

3.1 Base algorithm

The main purpose of this work is to extend the contact mechanics to the NNRPIM, in order to permit the analysis of 2D problems, considering an approximated non linear elastic assumption. The code was developed in a given algorithm, which is presented in Figure 3.1.

In step **A**, all the requested data is loaded. This includes data for geometry, as well as nodal mesh; integration scheme and order; material properties; natural and essential boundaries.

In step **B** the nodal mesh is created. The nodes permit to discretize the problem domain.

After the nodal mesh, the integration mesh is created, in step **C**, and next the influence-domain in step **D**.

In step **E** the interpolation functions are created, and following it the stiffness matrix in step **F**.

With the stiffness matrix created, the boundary conditions can be imposed (both natural and essential), step **G**. The system of equations is then solved and the displacements obtained in step **H**.

Finally, the stress field is determined as well as the nodal equivalent forces, step **I**.

3.2 Incremental approach

Most problems with interest in contact involve forging processes or conformation processes. The key aspect in those processes is the large deformation of the part. In such cases, the relation between the applied load and the displacements is not linear. Therefore, in order to execute examples with large deformation, a non-linear algorithm must be

implemented. To accomplish the primary objective of this work, the extension of the contact problem to the NNRPIM, an approximated non-linear algorithm was implemented.

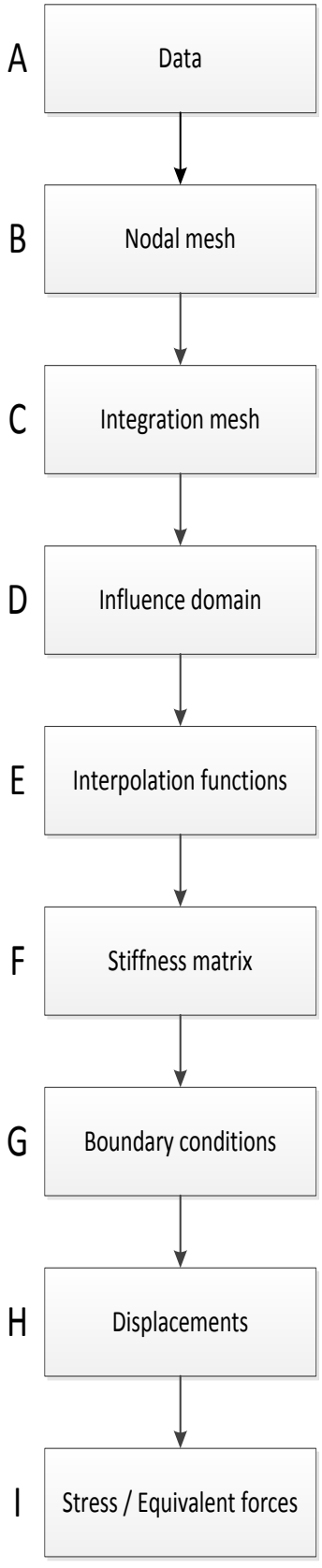

Figure 3.1: Base NNRPIM program algorithm.

The incremental approach, converts the base algorithm into an incremental algorithm. Meaning that, instead of running the linear elasto-static algorithm one time, the algorithm is called several times, being the number of times, the number of increments. In each increment, as the name implies, only an increment of the total load is applied. After the consideration of all the increments, the final solution is obtained. The incremental approach algorithm is presented in Figure 3.2.

In the first increment, the base linear elasto-static algorithm scheme is followed. From the second increment on both the nodal mesh and the integration mesh are updated and the influence-domain used is the one calculated in the first increment.

3.2.1 Nodal mesh update

The update of the nodal mesh consists in using at each increment, the deformed nodal mesh of the previous increment. This is expressed by equation (3.1)

$$\mathbf{x}^{i+1} = \mathbf{u}^{i} + \mathbf{x}^{i} \tag{3.1}$$

were i is the increment, $\mathbf{x}$ are the coordinates of the node $(x; y)$ and $\mathbf{u}$ are the displacements of the node $(u; v)$. This way, the obtained displacements are added increment after increment.

3.2.2 Integration mesh update

In a first attempt the integration mesh was generated in each increment, resorting to the Vornonoï cells and to the Delaunay tessellation as previously presented. But as soon as the solid domain starts to deform, the Delaunay tessellation is unable to follow efficiently the deformation. Consequently in the following increments, some integration points that obviously were inside the solid domain appear outside of it. These points must be deleted, since they not belong to the solid domain anymore but affect the result.

Thus, through the increments, the number of integration points changes (decreases to be more precise) and their distribution also changes, becoming heterogeneous, meaning that a node will not have the same number of integration points around it from the start to the end of the analysis.

As a practical result, the load/displacement curve is completely wrong, making the results useless.

To solve this problem, the integration mesh is updated instead of generated in each increment, much like the nodal mesh. But in order to move the Gauss points to the correct position is not enough to use the displacements directly, so one must use the shape functions also. Thus, the equation (2.44) is used.

The weight of the integration point, since it is the area of the sub-cell, most likely changes. However, for simplicity, it was assumed constant and, therefore is calculated at the first increment and used through the next increments.

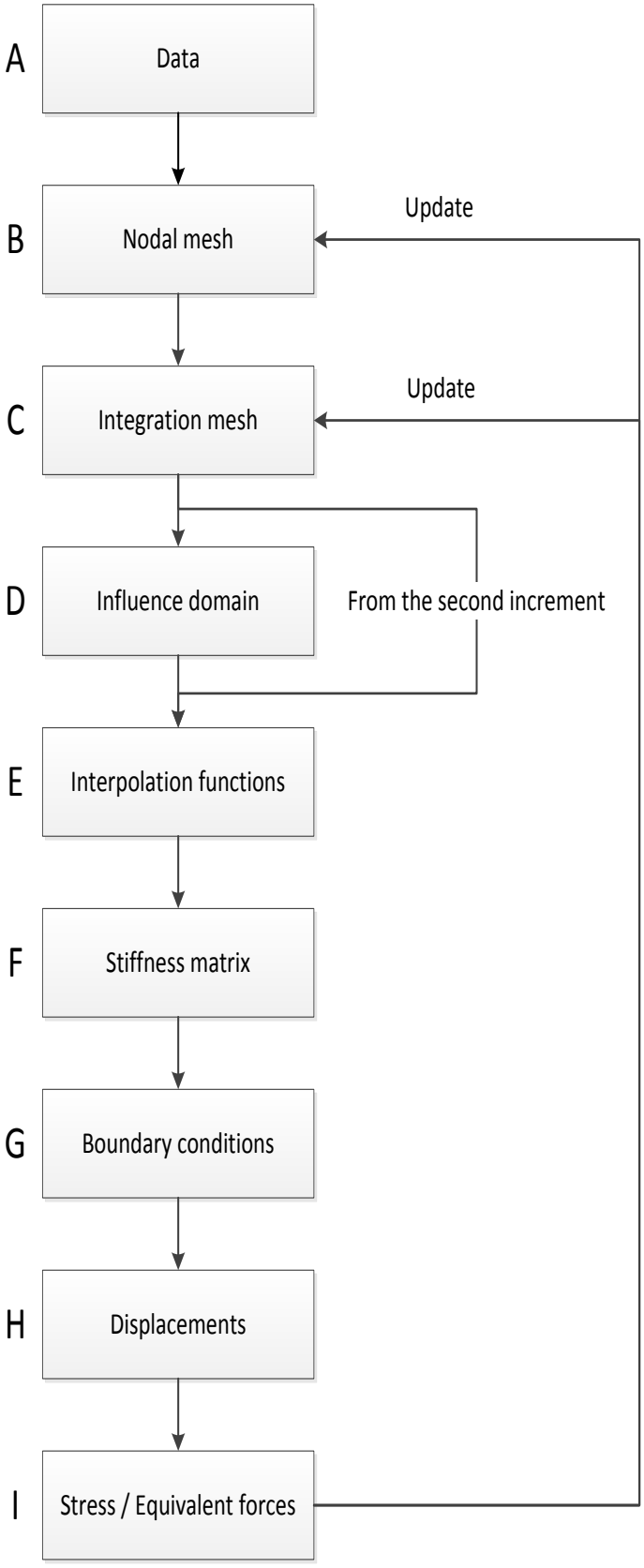

Figure 3.2: Incremental approach algorithm.

The total load value is mandatory so, at the beginning, in step **A** (Figure 3.2) the number of increments is defined, and then the load is equally divided by the number of increments, which means that in each increment the load increment applied is the same.

3.3 Contact approach

3.3.1 General algorithm

The contact method applied in this work is the so-called "a posteriori method". In this method in each increment the displacement field is calculated as if it was just being analyzed a static problem without contact.

After the determination of the displacements, and before the next increment, a contact detection algorithm checks if at least one node passed through one of the existent boundaries (step **K** in Figure 3.3). If some node makes it through the boundary, the analysis is receded by the necessary amount, so that node final position lies in the boundary. The load increment is receded respecting the same ratio.

With the node in the boundary, the process moves to the next increment, now considering this node as a boundary node.

To move the node to the boundary, it is used a regress factor calculated in terms of the distance between the final position and the initial position of the node and, the distance between the initial position of the node and the expected boundary position. Therefore this factor represents a proportion of the distance that the node should have traveled considering the boundary, and the distance actually traveled (because the boundary was not considered).

Since the process recedes every time contact occurs, the total number of increments is not initial predefined value, but higher. The load increment remains the same in each increment (except to the last increment) because the displacements are determined without considering contact. The last increment uses a smaller load increment than the previous, because the real applied load in each increment varies if there is contact, so at the end there will be a residual load smaller than predefined load increment.

The contact with the boundary is not an irreversible situation, for the reason that a node that contacts with a boundary can easily stop contacting.

When contact is detected, and then in the following increment the boundary condition is applied, the node becomes connected to the boundary. The stiffness matrix is recalculated in each increment, and from the moment that the contact is detected, the node is connected to the boundary.

To know if a node continues to be in contact with the boundary, it is required to determine the equivalent forces.

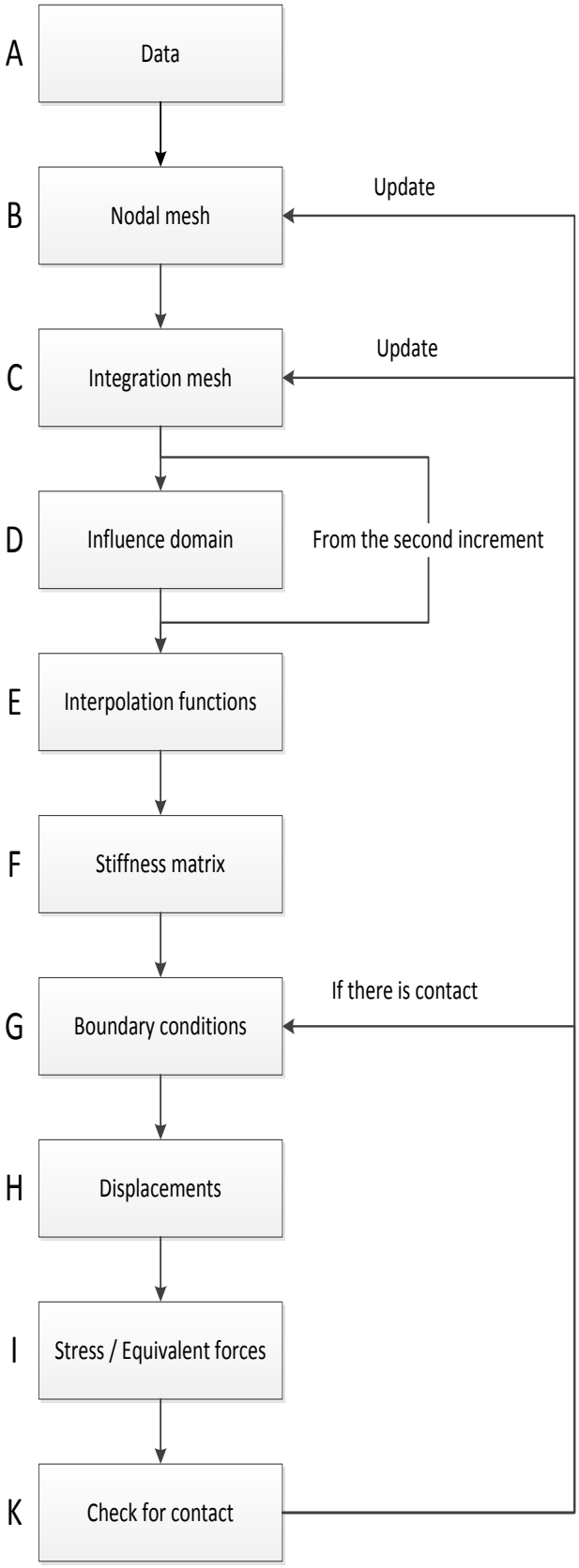

Figure 3.3: Contact approach algorithm.

These equivalent forces are the reaction forces in each node. When the node is not constrained in some way, these values are null, while if it is, the equivalent forces are the reaction forces of the node.

For each boundary, when the first node contacts, in the next increment the contact node reaction force sign is saved. Naturally the sign of the reaction force is positive, considering the boundary normal at that particularly point.

Then in each increment, for all the nodes that are in contact with each boundary, their sign is compared with the saved sign for that boundary. If the sign changes, it means that node is trying to move away from the boundary. From that increment on, that node will be disconnected from the boundary. The node becomes again an ordinary node that can contact with the boundary at any future increment.

The nodes in contact cannot move in the direction perpendicular to the boundary, but can in the tangent direction (freely, because friction is not considered).

When leading with arbitrary shape boundaries, the node is constrained along the boundary normal direction at the point of contact. For the node to be able to follow the boundary, in each increment, when the boundary conditions are imposed, the normal vector used is determined using the final position of the node along xx. It is assumed that for a number of increments sufficient large, the quantity of the displacement in the xx direction is not big enough to separate the node from the boundary. The practical examples show that this assumption is valid.

3.3.2 Determination of the regress factor

In each increment, when contact is verified, generally several nodes pass beyond the boundary and in more than one boundary. The regress factor must be capable of placing one of those nodes in the boundary, and all the others behind it. This means that the factor needs to be calculated for the node that passed the boundary with the highest extent.

In a 2D problem, there are two degrees of freedom per node, therefore each node has two displacement components. Also the relative displacement magnitude between each node and the arbitrary shape of the boundary represent numerical difficulties that must be overcome. For all of this, is difficult to find a criterion that works every time. To guarantee that the correct factor is used, when contact is detected, the factor is calculated for all the nodes that are inside the boundary, and then the smallest one is assumed.

The regress factor is calculated by two different ways, depending if the boundary is static or dynamic.

In the case of static boundaries, the regress factor is defined as

$$r_f = \frac{\sqrt{(x_{boundary} - x_{initial})^2 + (y_{boundary} - y_{initial})^2}}{\sqrt{(x_{final} - x_{initial})^2 + (y_{final} - y_{initial})^2}} \tag{3.2}$$

being the numerator the distance between the point in the boundary where the node should be and the initial position of the node; and the denominator the distance between the initial and the final position of the node.

The node moves from the initial position to the final position through a line as seen in Figure 3.4, so the point in the boundary is determined by intersecting the boundary function with the line defined by the initial and final position of the node.

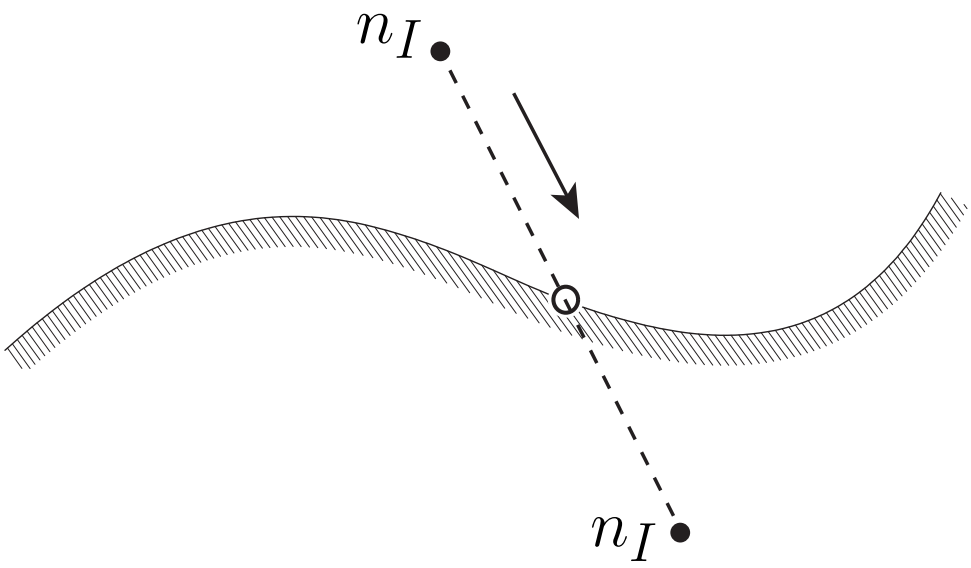

Figure 3.4: Position of a contact node before and after he passed the boundary.

If the boundary is dynamic, the determination of the regress factor is more complex.

In Figure 3.5 it is shown a boundary moving down, and the detected contact node. In this case the node also moves down, because is assumed that some neighbouring nodes already have contacted the boundary (if not, the initial and final position of the node is the same). As so the initial position of the node is below the boundary, while the final position is above the boundary. This means that the boundary overpassed the node.

At some point between the initial and the final position, the node intersected the boundary. The geometrical position indicated with a circle in Figure 3.5 is where the node should be.

To determine the regress factor, equation (3.1) is recalled for a specific increment, in each component

$$x_{final} = u + x_{initial} \tag{3.3}$$

$$y_{final} = v + y_{initial} \tag{3.4}$$

These equations can be parameterized using the regress factor, which is the unknown variable. The new equations are defined by

$$x_{final} = ur_f + x_{initial} \tag{3.5}$$

$$y_{final} = vr_f + y_{initial} \tag{3.6}$$

To determine the regress factor, the coordinates x, y must satisfy equations (3.5) and (3.6) and the equation of the boundary, which depends of the imposed displacement and its initial position.

For details about the intersection with different boundaries, refer to Appendix A to Appendix E.

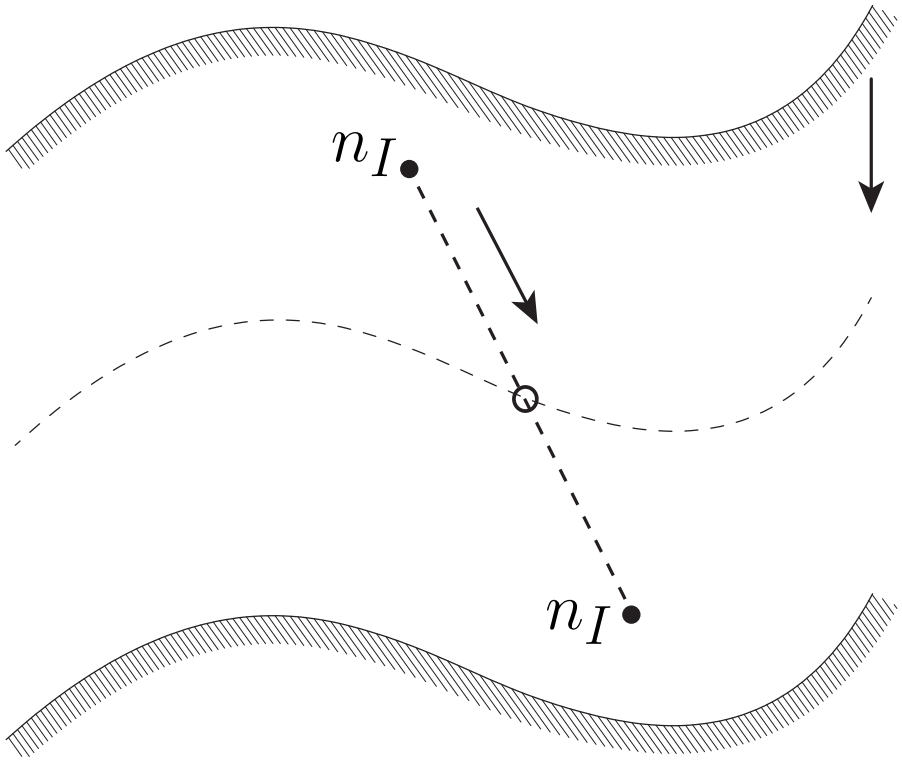

Figure 3.5: Initial and final position of contact node and initial and final position of dynamic boundary.

Chapter 4

Numerical examples

4.1 Linear examples

4.1.1 Cantilever beam

The first example is the classic cantilever beam. The dimensions and the boundary conditions can be seen in Figure 4.1.

The exact solution for the displacements can be defined as [87]

$$u = -\frac{Qy}{6EI}\left[3x(2L_{sd} - x) + (2+\nu)(y^2 - \frac{D^2}{4})\right] \tag{4.1}$$

$$v = \frac{Q}{6EI}\left[x^2(3L_{sd} - x) + 3\nu(L_{sd} - x)y^2 + \frac{4+5\nu}{4}D^2x\right] \tag{4.2}$$

where L_{sd} is the length of the solid domain, D the height, Q the total load applied and I is the moment of inertia,

$$I = \frac{eD^3}{12} \tag{4.3}$$

being e the thickness, which is equal to one, because the problem is analyzed in 2D only.

The stress field is defined by [87]

$$\sigma_{xx} = -\frac{Q(L_{sd} - x)y}{I} \tag{4.4}$$

$$\sigma_{yy} = 0 \tag{4.5}$$

$$\tau_{xy} = \frac{Q}{2I}(\frac{D^2}{4} - y^2) \tag{4.6}$$

The Young modulus E used is 1000 Pa, and the Poisson ratio ν is 0,3. It is considered plane stress analysis. The load per unit length q used is 1 N/m.

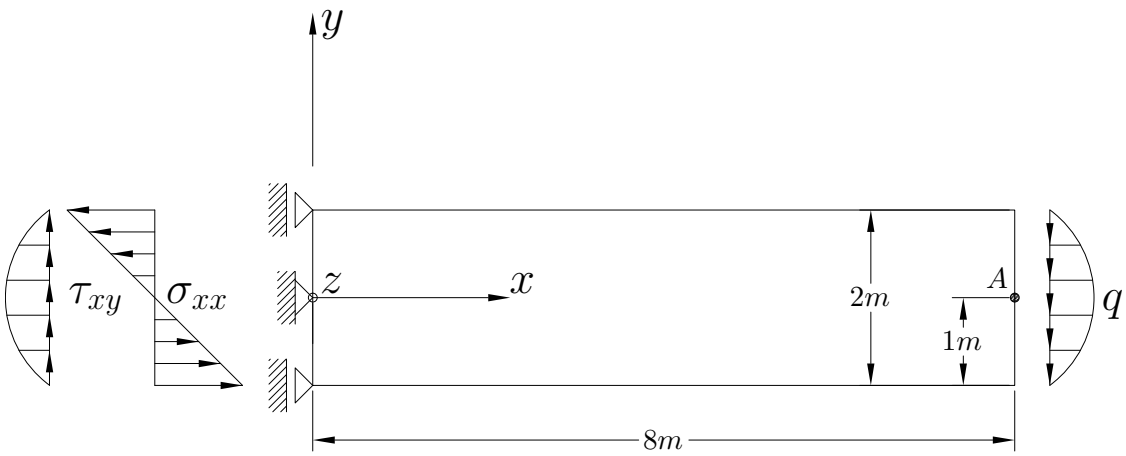

Figure 4.1: Cantilever beam: dimensions and boundary conditions.

A comparison between the displacements obtained with the analytic solution and the NNRPIM solution was carried out, for different number of nodes using the rule 2^n in the divisions. In the NNRPIM solution it was used two types of meshes, regular mesh and irregular mesh. The regular mesh consists on a grid of points evenly distributed. The two types of meshes are compared in Figure 4.2.

The vertical displacement of point A (see Figure 4.1) was analyzed. The results are expressed in Figure 4.3.

The error relative to the analytic solution was calculated (equation (4.7)) to better understand the precision of the NNRPIM, and the difference between regular mesh and irregular mesh.

$$Error(\%) = \left| \frac{v_{NNRPIM} - v_{teórico}}{v_{teórico}} \right| \times 100 \tag{4.7}$$

The error is presented in Figure 4.4. One can note that with few nodes, there is a considerable error, but it is not necessary to increase the number of nodes much to have an error smaller than 1%, both in regular and irregular meshes.

About the mesh types, with the regular mesh, the error decreases continuously with the increase of nodes, while with the irregular mesh, it changes significantly. This makes the irregular mesh not reliable, so it will not be used in future examples.

The stress distribution in a section of the beam was obtained (see Figure 4.5). The section is at 0,1875 m from the origin in the xx direction (see Figure 4.1), therefore the support does not affect the result, as would happen if the stress was obtained in the support section. The results are very close to the analytical value from equations (4.4), (4.5) and (4.6).

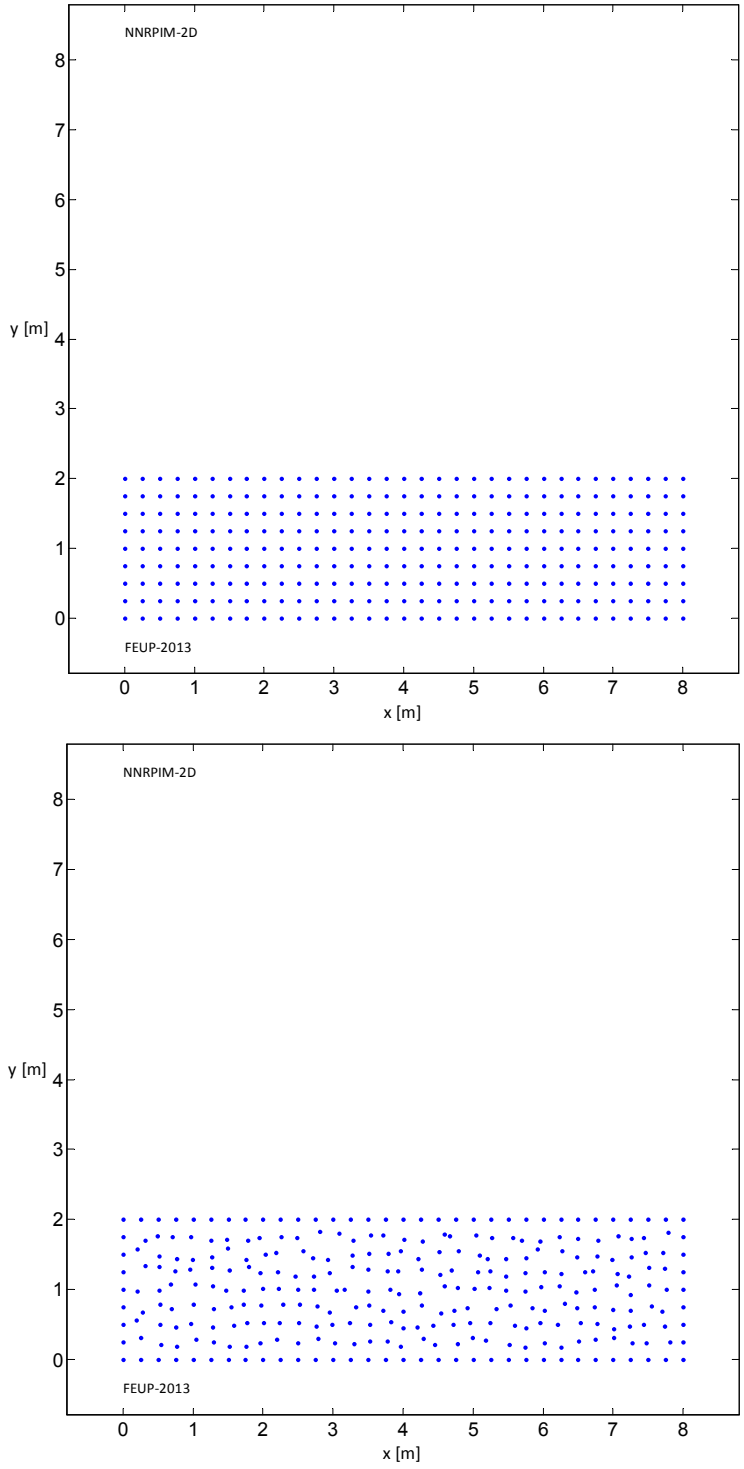

Figure 4.2: Comparison between regular mesh and irregular mesh.

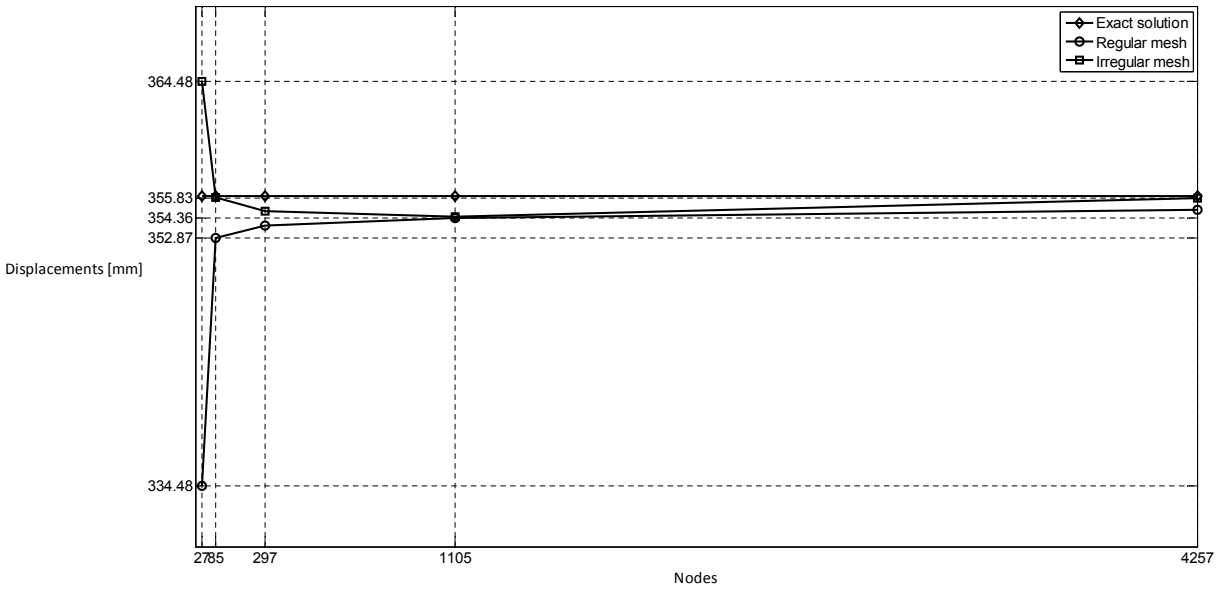

Figure 4.3: Comparison between analytic displacement and NNRPIM displacement in Point A along yy direction.

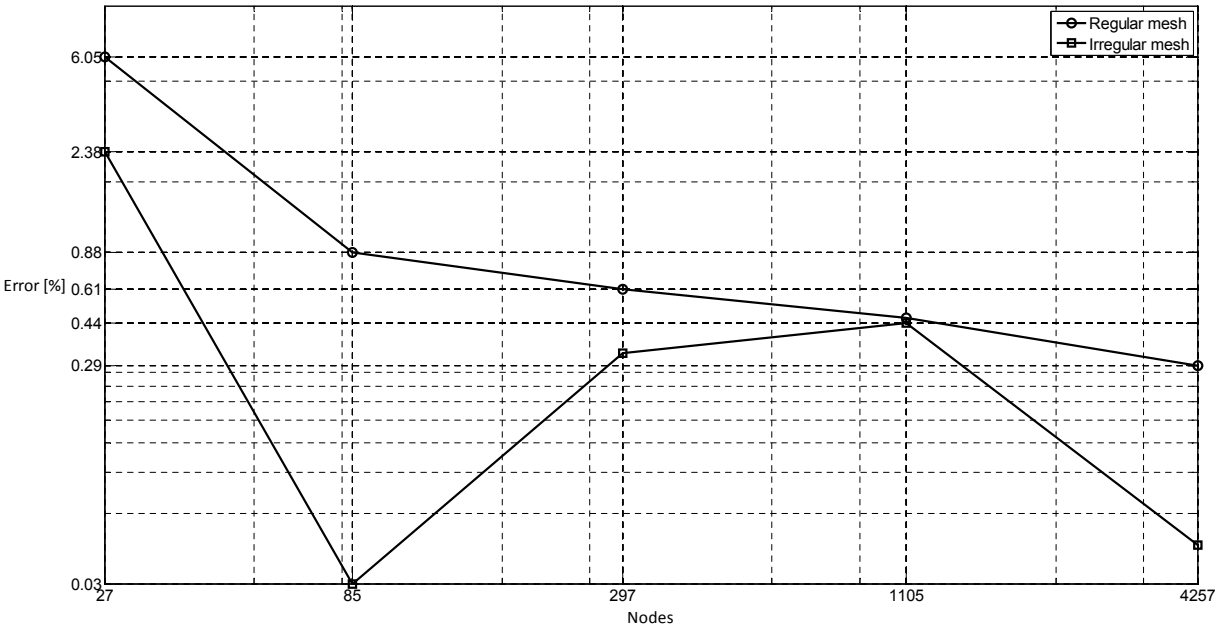

Figure 4.4: Relative error between analytic displacement and NNRPIM displacement in point A along yy direction.

The centre fibre of the beam is represented in Figure 4.6, before and after deformation.

Finally in Figure 4.7, is shown the stress distribution for the entire beam, considering a mesh of 4257 nodes.

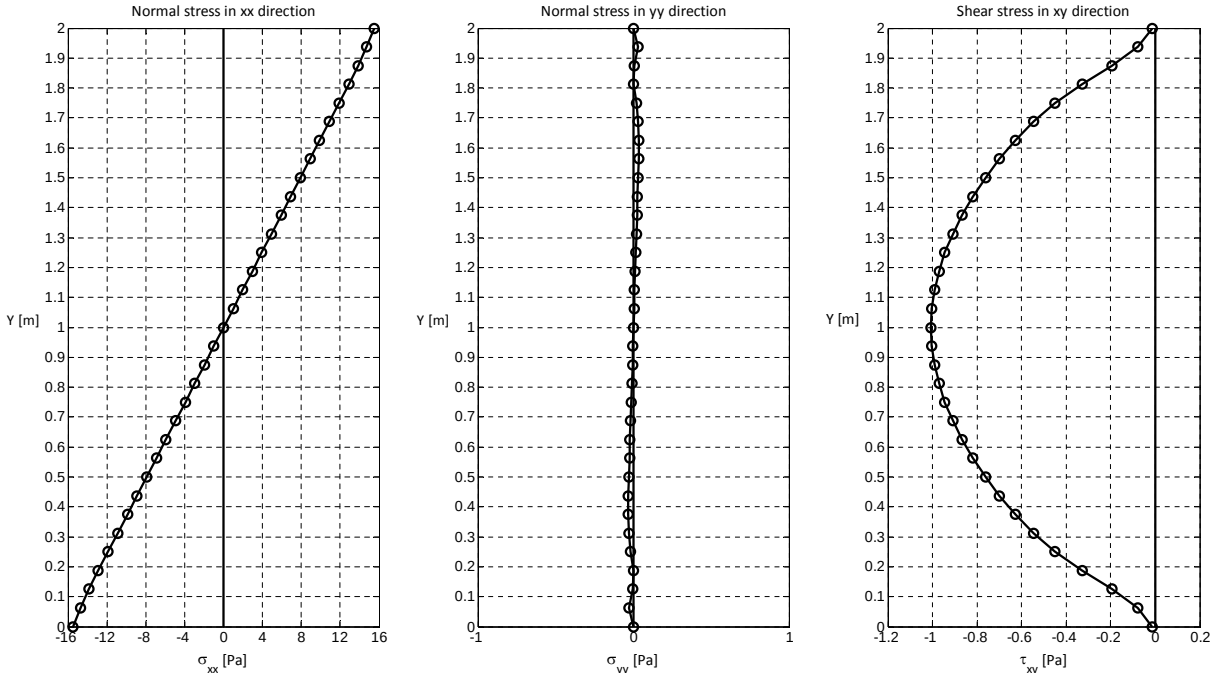

Figure 4.5: Stress distribution in a section at 0,1875 m in the xx direction.

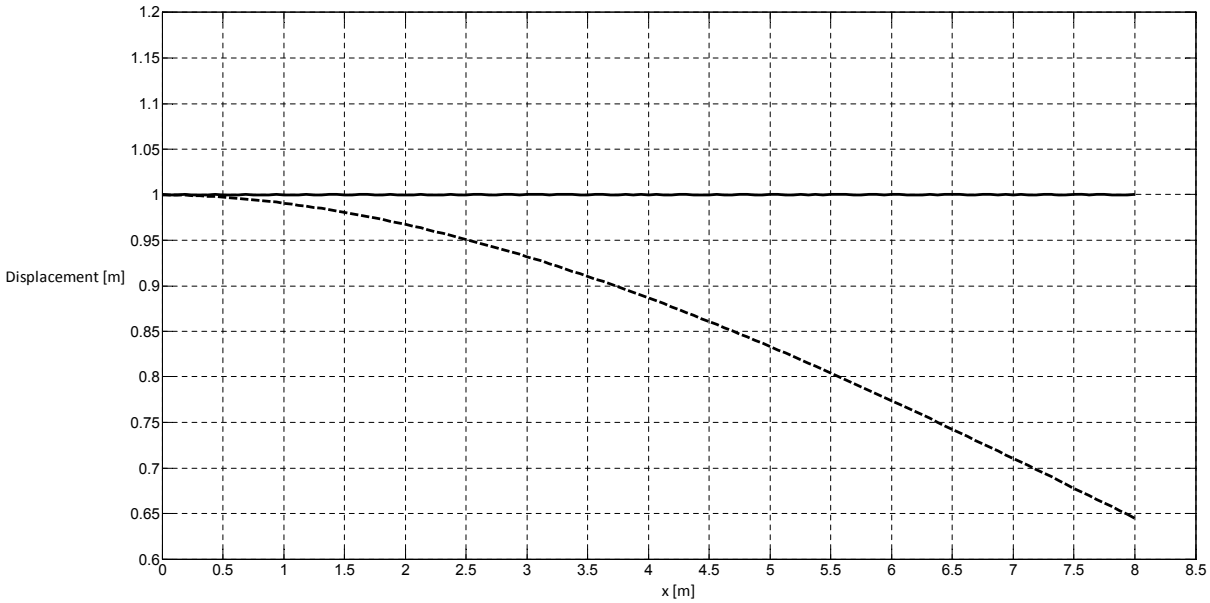

Figure 4.6: Deformed and undeformed centre fibre.

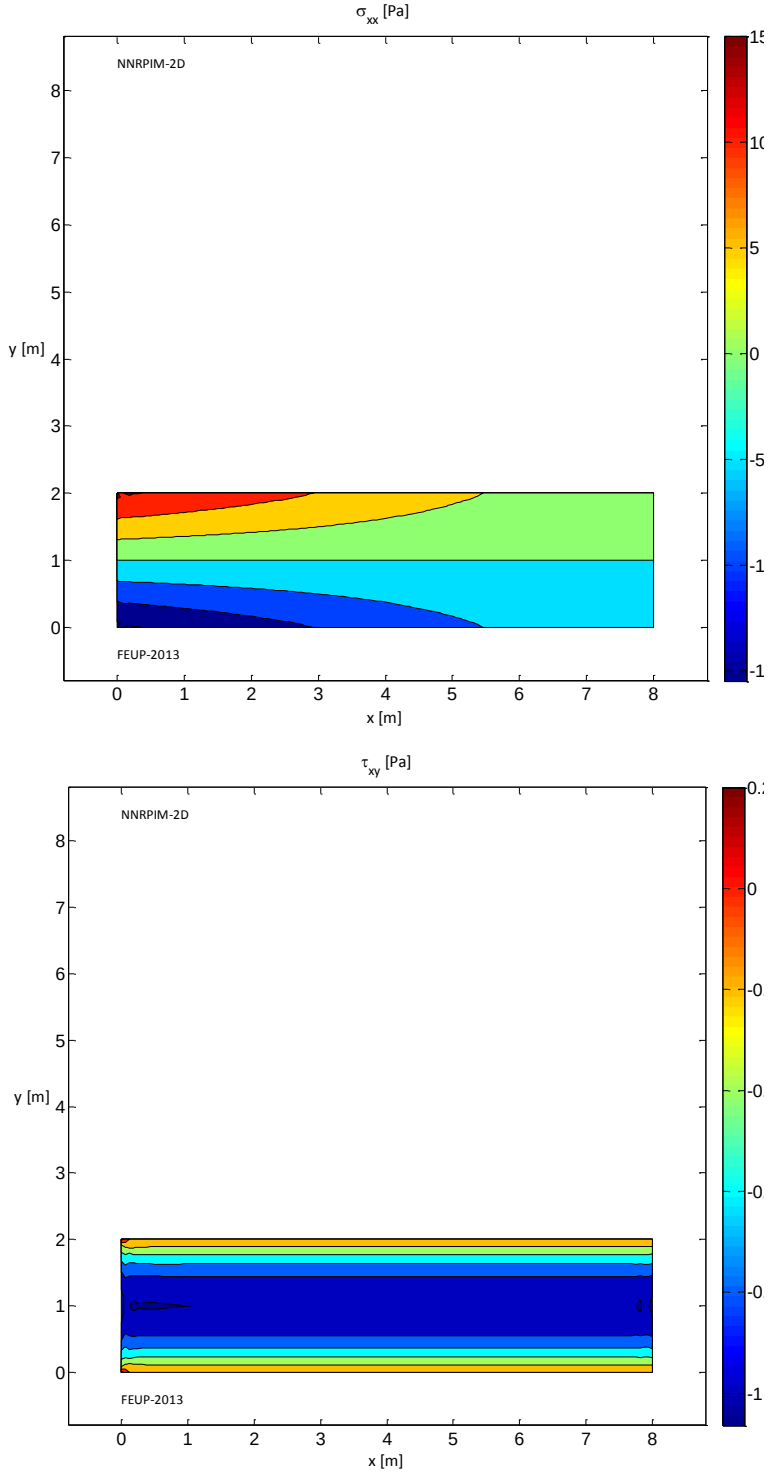

Figure 4.7: Obtained stress field in the cantilever beam.

4.1.2 Plate with centre hole

A plate with a centre hole was analyzed. Due the symmetry of the problem, only a quarter of it was modeled. The dimensions and boundary conditions are shown in Figure 4.8.

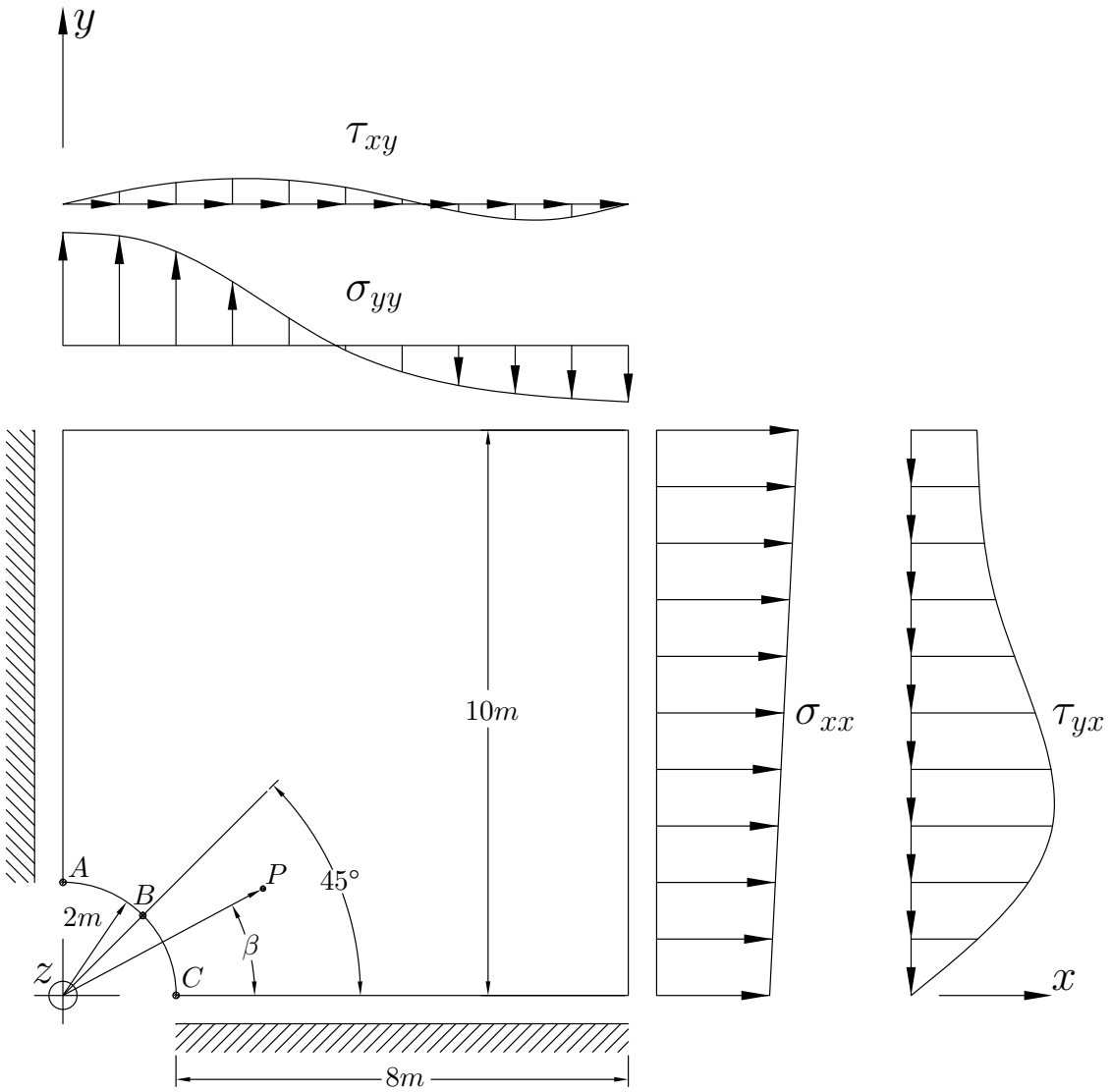

Figure 4.8: Plate with centre hole (right upper part): dimensions and boundary conditions.

The exact solution for the stress field is obtained with [9]

$$\sigma_{xx} = \sigma_o \left[1 - \frac{a_h^2}{r^2}\left(\frac{3}{2}\cos(2\beta) + \cos(4\beta)\right) + \frac{3a_h^4}{2r^4}\cos(4\beta)\right] \tag{4.8}$$

$$\sigma_{yy} = \sigma_o \left[-\frac{a_h^2}{r^2}\left(\frac{1}{2}\cos(2\beta) - \cos(4\beta)\right) - \frac{3a_h^4}{2r^4}\cos(4\beta)\right] \tag{4.9}$$

$$\tau_{xy} = \sigma_o \left[-\frac{a_h^2}{r^2}\left(\frac{1}{2}\sin(2\beta) - \sin(4\beta)\right) + \frac{3a_h^4}{2r^4}\sin(4\beta) \right] \tag{4.10}$$

where σ_o is the stress magnitude, a_h is the radius of the hole and r is the distance from point P to the origin (see Figure 4.8). The Young modulus E used is 1000 Pa, and the Poisson ratio ν is 0,3. It is considered plane stress analysis. The stress magnitude used is 100 Pa. The analytical solution for the displacements is defined as [88]

$$u(r,\beta) = \sigma_o \frac{a_h}{8G}\left(\frac{r}{a_h}(k+1)cos(\beta) + \frac{2a_h}{r}((1+k)cos(\beta) + \cos(3\beta)) - \frac{2a_h^3}{r^3}cos(3\beta) \right) \tag{4.11}$$

$$v(r,\beta) = \sigma_o \frac{a_h}{8G}\left(\frac{r}{a_h}(k-3)sin(\beta) + \frac{2a_h}{r}((1-k)sin(\beta) + \sin(3\beta)) - \frac{2a_h^3}{r^3}sin(3\beta) \right) \tag{4.12}$$

where k is defined as

$$k = \begin{cases} 3-4\nu & PlaneStrain \\ \dfrac{3-\nu}{1+1\nu} & PlaneStress \end{cases} \tag{4.13}$$

and G by

$$G = \frac{E}{2(1+\nu)} \tag{4.14}$$

The error between the analytic displacement and the NNRPIM displacement was determined for three types of mesh: regular mesh, refined mesh with rectangular refinement and refined mesh with circular refinement. The three types of meshes are represented in Figure 4.9. The error was calculated using equation (4.7) for three points, A, B and C (see Figure 4.8). In point A, the displacement v along yy is compared; in point B, both the displacements u and v along xx and yy respectively are compared; in point C only the displacement u is compared. The errors are presented in Figure 4.10 to Figure 4.13.

In the case of the circular refinement, to follow the rule of 2^n, only two points could be obtained due algorithm constraints. With the rectangular refinement in point C at first the error increases with the number of nodes, therefore is not a reliable choice. Also in the transition zone, between the refined part and the unrefined part, even using a smooth transition (in steps), the results in terms of stress and strain are affected (see Figure 4.14). Thus, the regular mesh is assumed to be the best choice of them all.

The stress in xx direction along left boundary is presented in Figure 4.15 and in Figure 4.16 is presented the stress in yy direction along bottom boundary.

In Figure 4.17 is shown the nodal mesh used for this analysis (4125 nodes), as well as the stress distribution for the quarter panel of the plate.

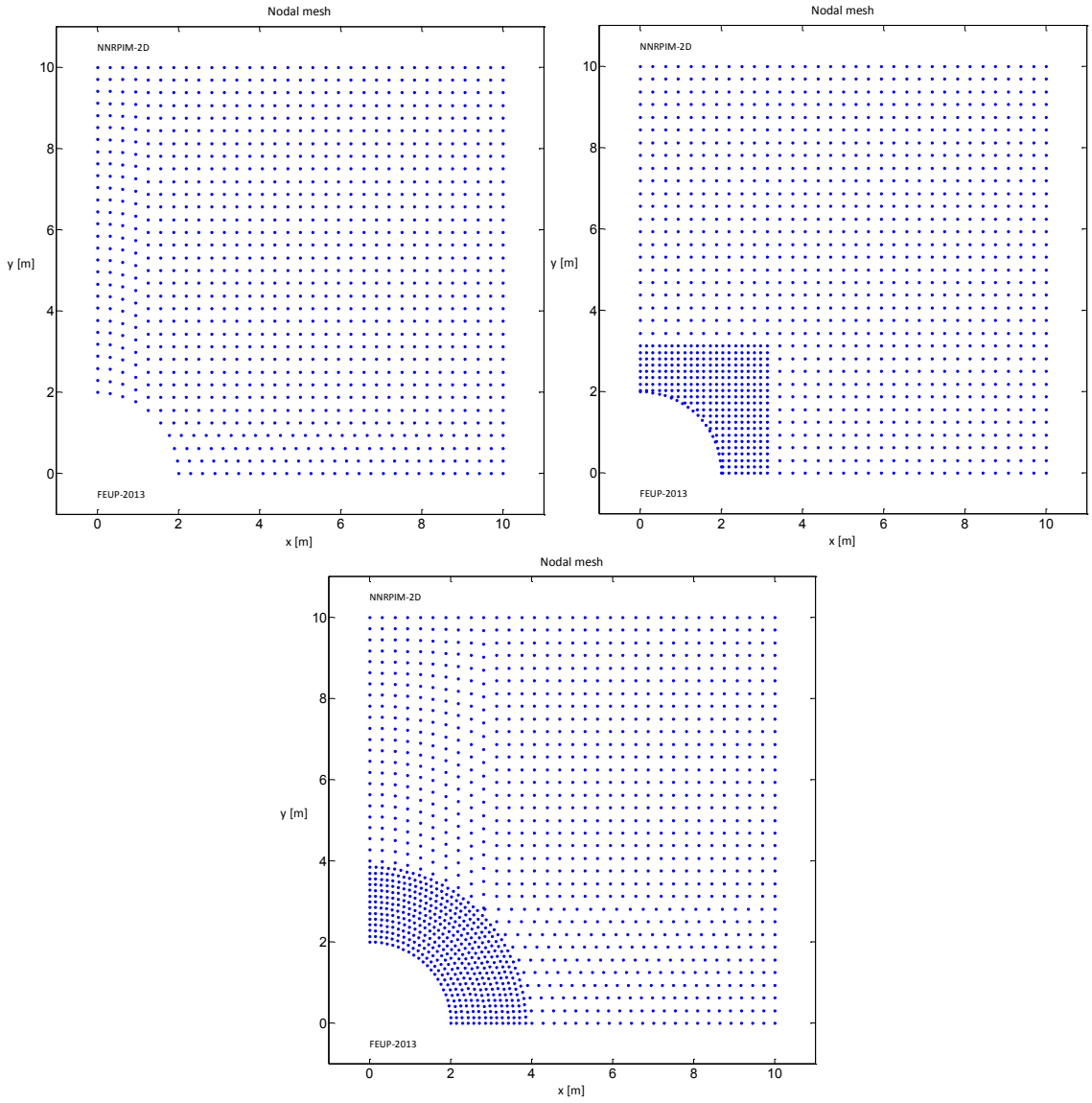

Figure 4.9: Different types of meshes used in the error analysis of the plate with centre hole.

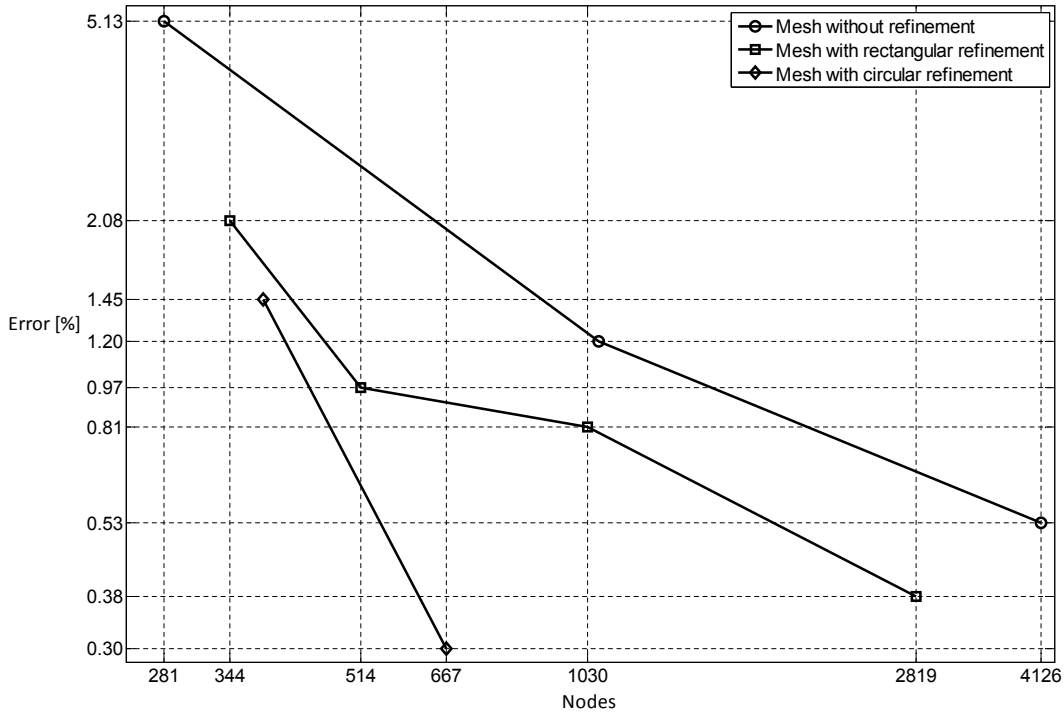

Figure 4.10: Relative error between analytic displacement and NNRPIM displacement in point A along yy direction.

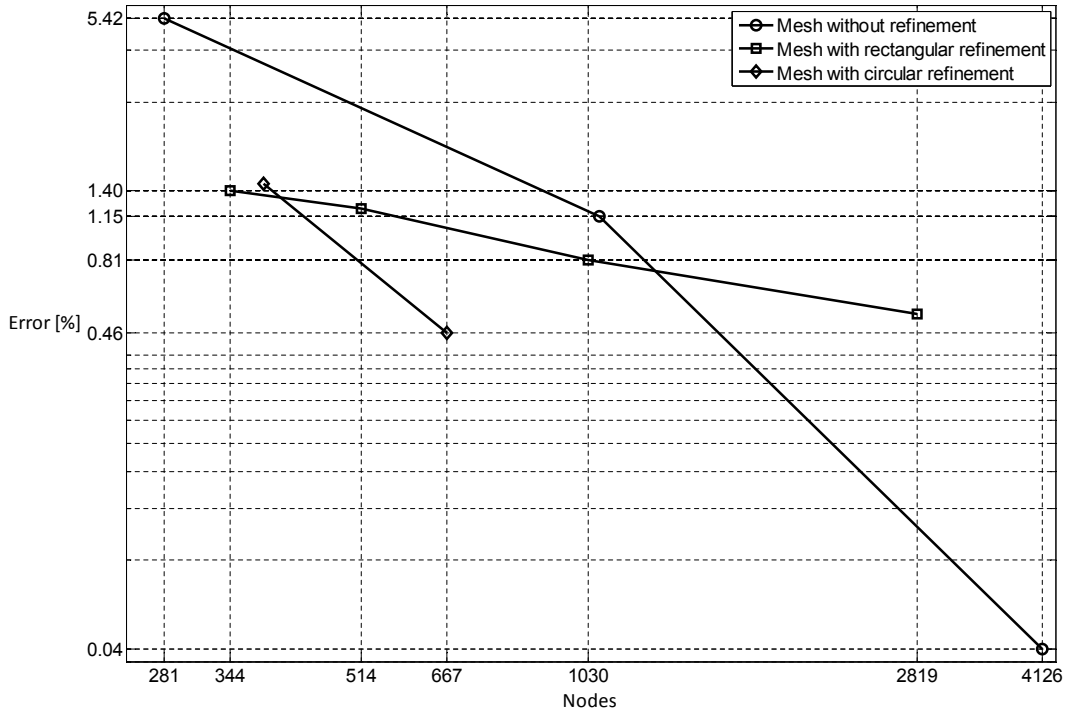

Figure 4.11: Relative error between analytic displacement and NNRPIM displacement in point B along xx direction.

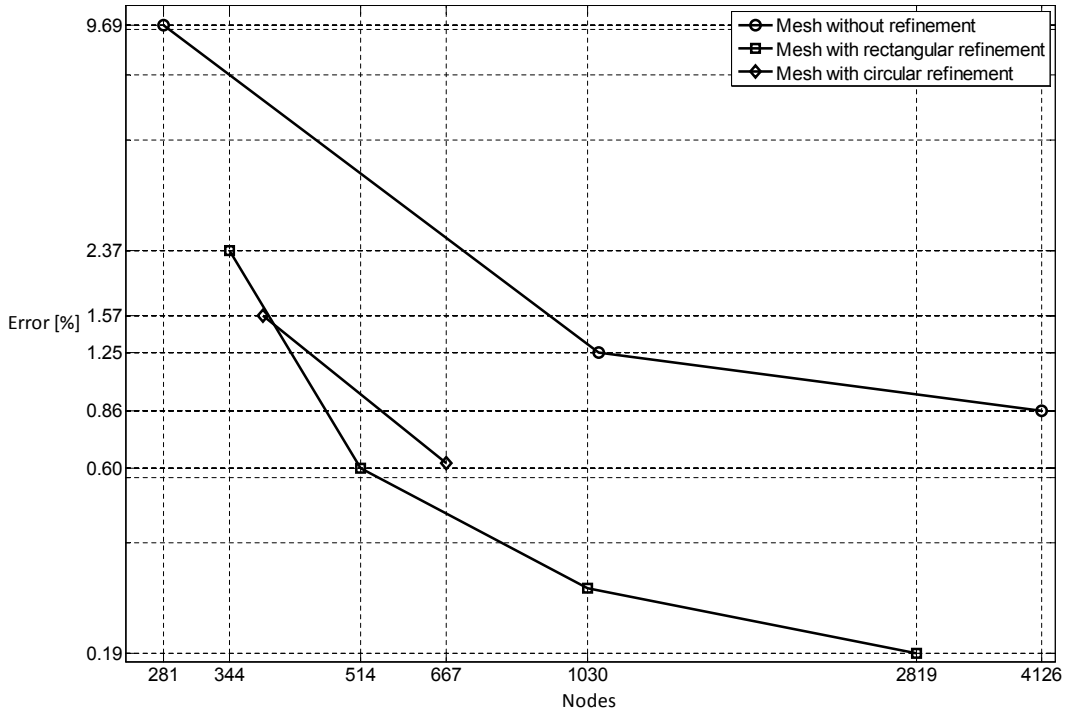

Figure 4.12: Relative error between analytic displacement and NNRPIM displacement in point B along yy direction.

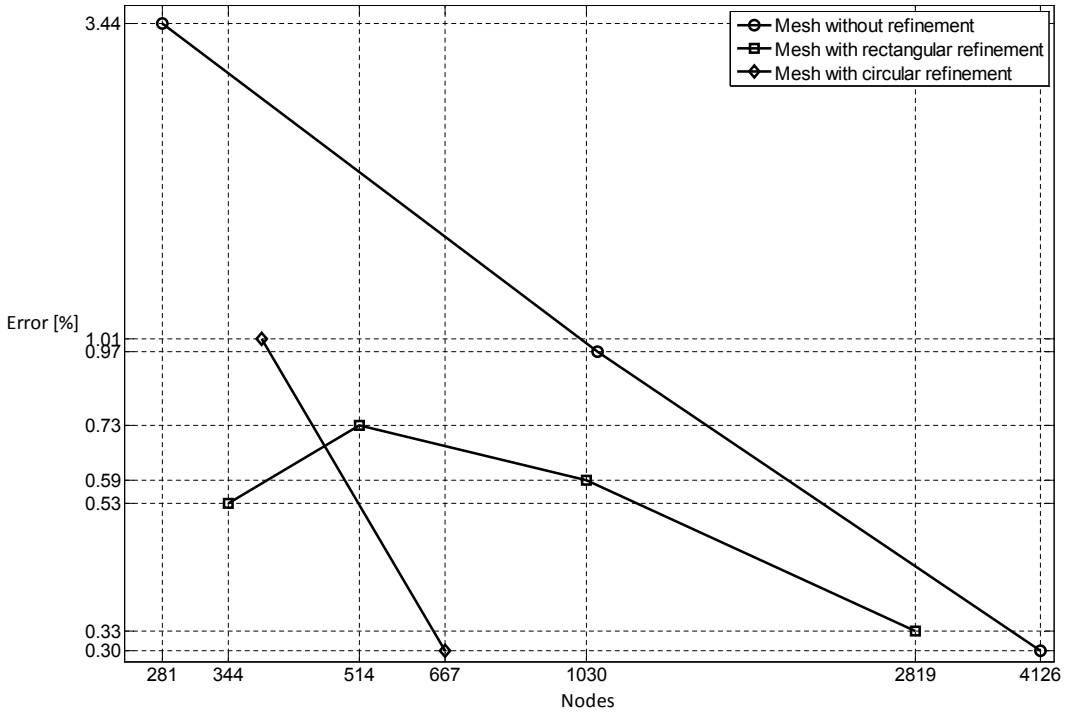

Figure 4.13: Relative error between analytic displacement and NNRPIM displacement in point C along xx direction.

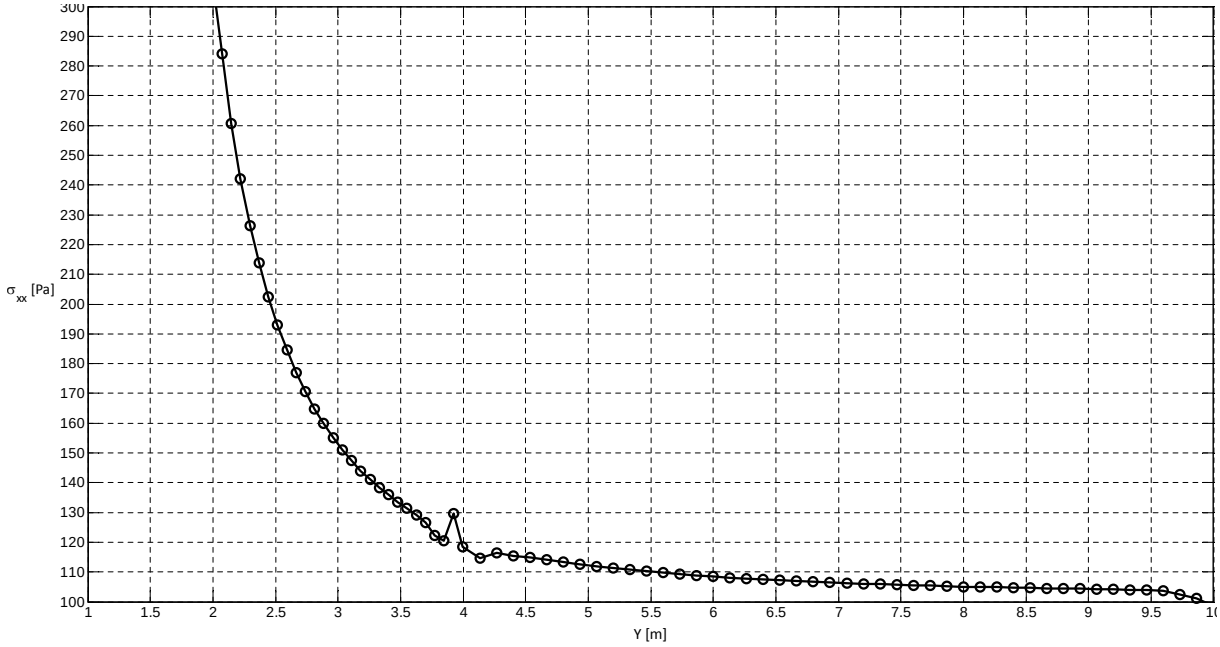

Figure 4.14: Normal stress in xx direction along left boundary considering circular refinement.

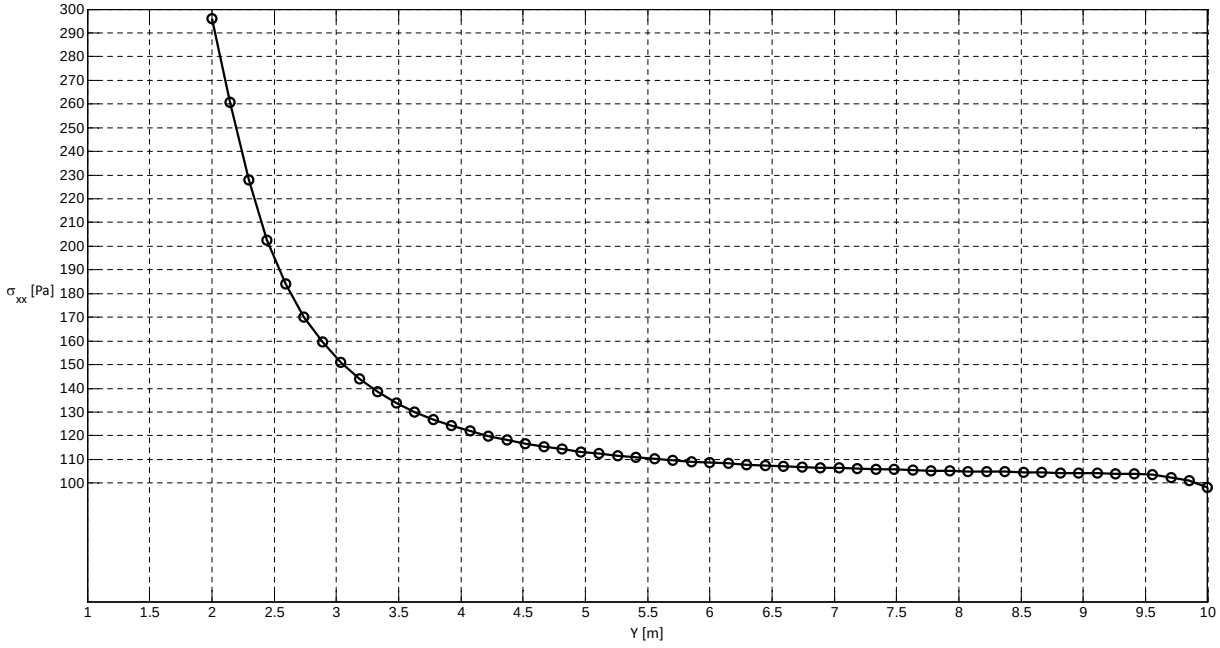

Figure 4.15: Normal stress in xx direction along left boundary.

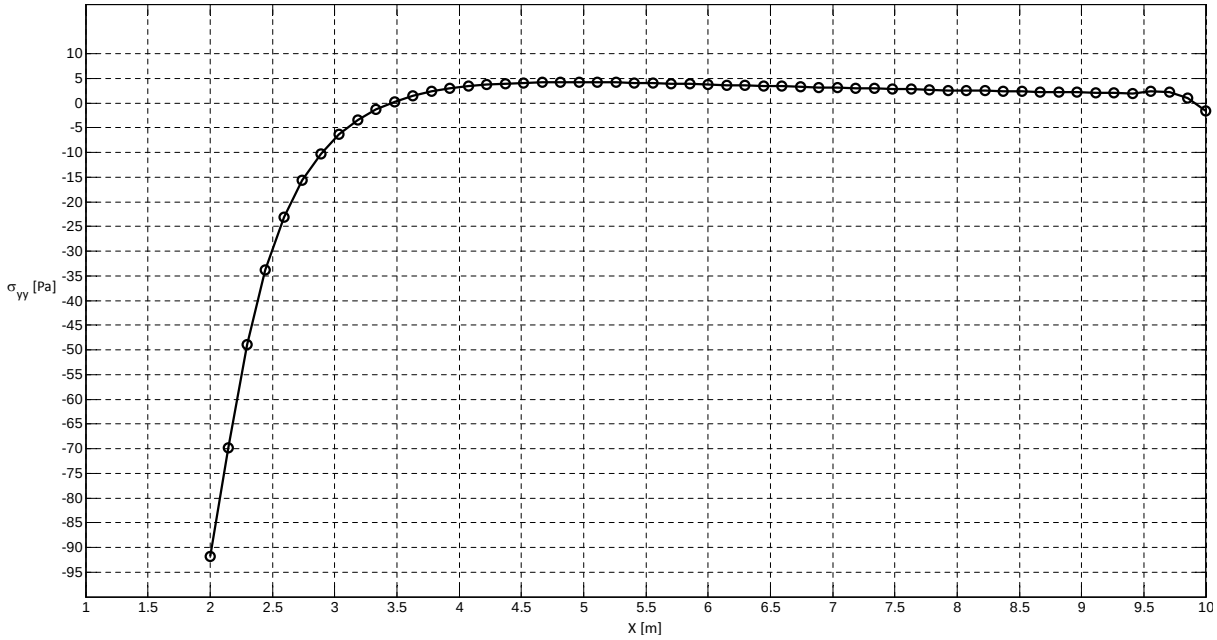

Figure 4.16: Normal stress in yy direction along bottom boundary.

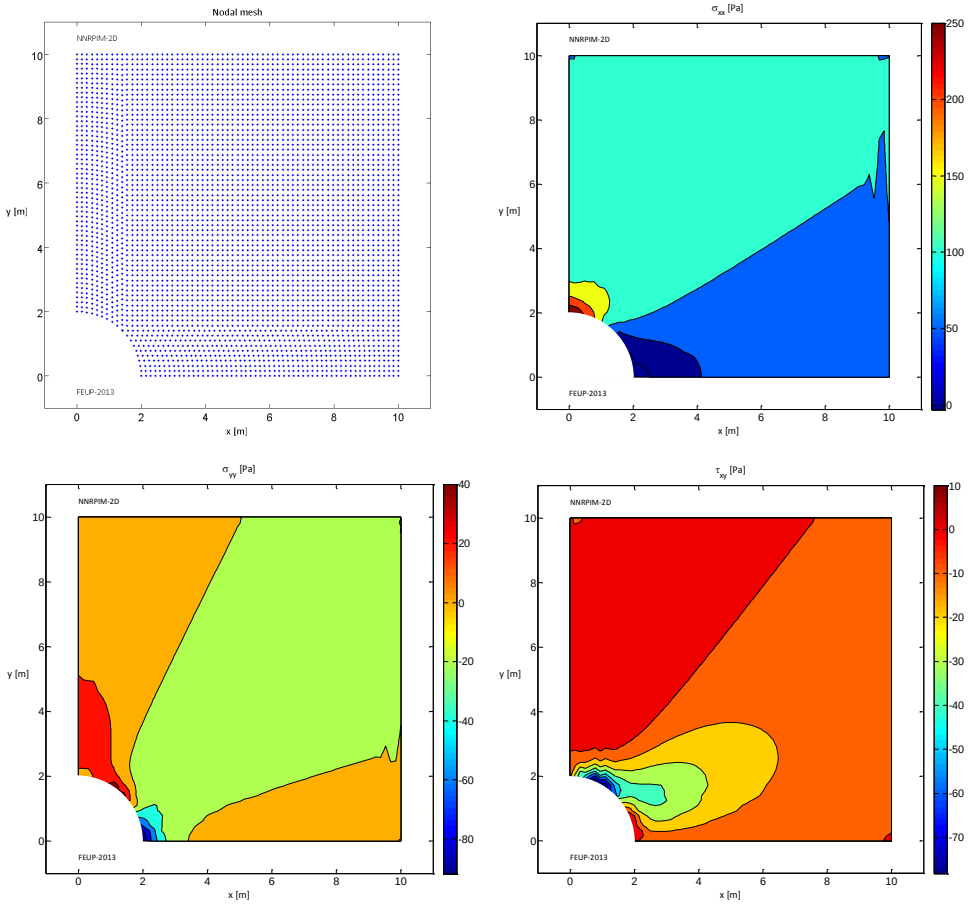

Figure 4.17: Nodal mesh and obtained stress field in the plate with a centre hole.

4.1.3 Diagonal boundary beam

A beam with a diagonal boundary was studied. The dimensions and boundary conditions are shown in Figure 4.18. The Young modulus E used is 1000 Pa, and the Poisson ratio ν is 0,3. It is considered plane stress analysis. The load per unit length q used is 20 N/m.

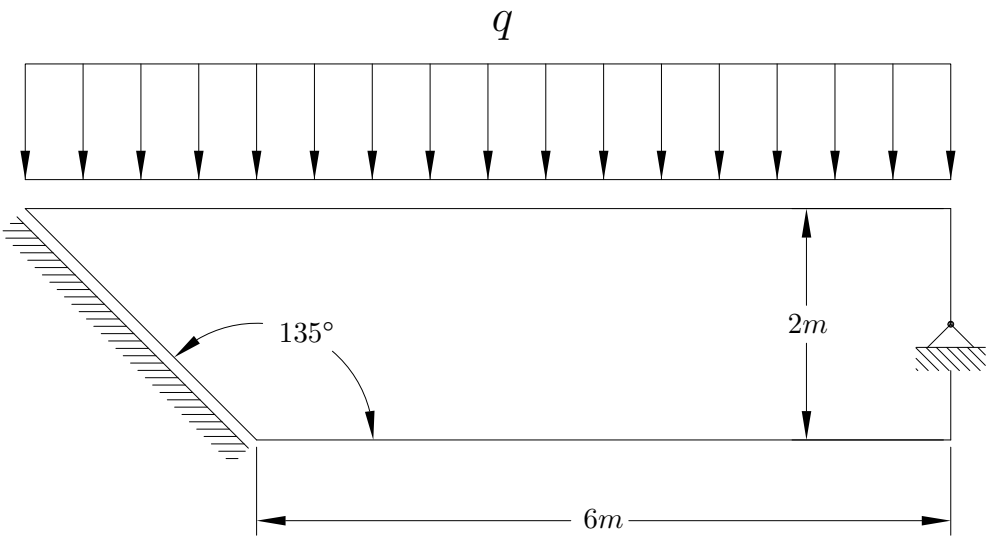

Figure 4.18: Beam with double support and diagonal boundary: dimensions and boundary conditions.

The only purpose of this example was to test a diagonal boundary. The comparison between the deformed and undeformed mesh is presented in Figure 4.19. To easily see the difference, a mesh of 969 nodes was used.

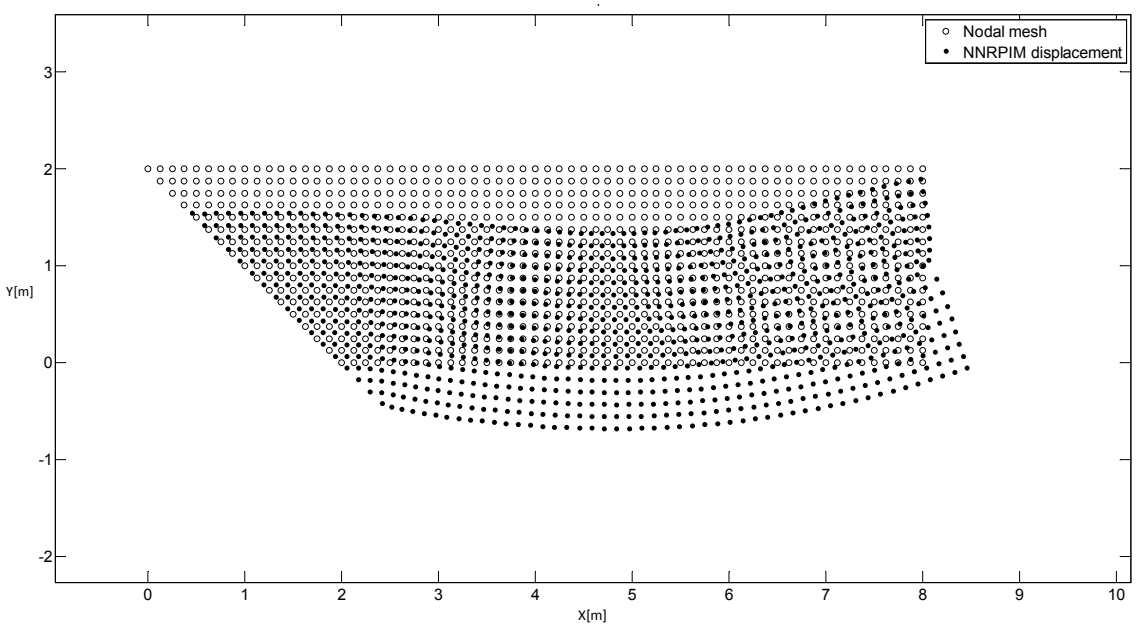

Figure 4.19: Base mesh and deformed mesh for the beam with a diagonal boundary.

4.1.4 Plate with centre hole and diagonal boundary

Another test carried out with a diagonal boundary is a plate with a centre hole, sliced in half. The results are compared with the results obtained for the complete problem. The diagonal boundary is considered to make equivalence with the base problem. The base problem dimensions and boundary conditions are expressed in Figure 4.20. The Young modulus E used is 1000 Pa, and the Poisson ratio ν is 0,3. It is considered plane stress analysis. The load per unit length q used is 100 N/m. It was used a mesh of 4125 nodes.

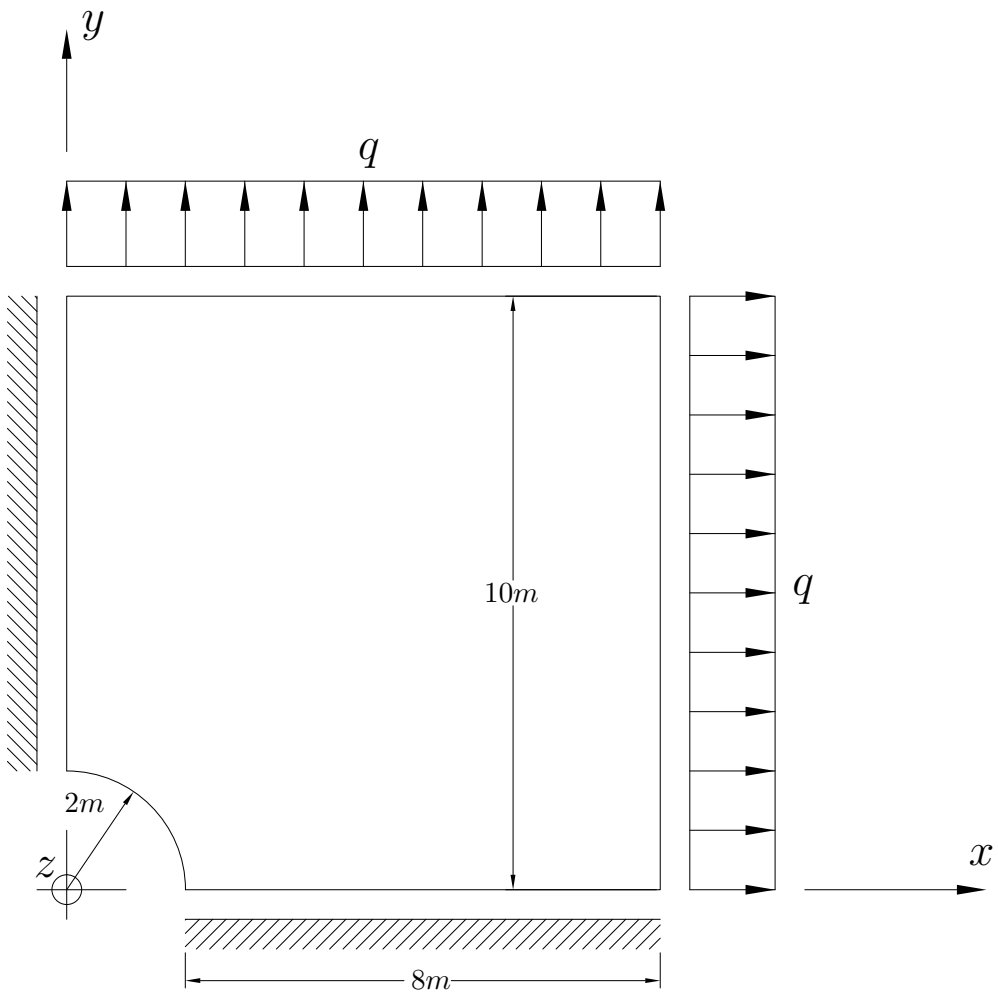

Figure 4.20: Plate with centre hole and diagonal boundary (right upper part – base model): dimensions and boundary conditions.

In Figure 4.21 is the deformed and undeformed mesh for the base problem. The most outer node in the right upper corner had a displacement $u = 0,7486$ m in the xx direction and a displacement $v = 0,7486$ m in the yy direction.

Next, the base problem was sliced in half and a diagonal boundary was added in the slice line. The sliced problem dimensions and boundary conditions are expressed in Figure 4.22.

The mesh used is the same, only now there is just half the mesh.

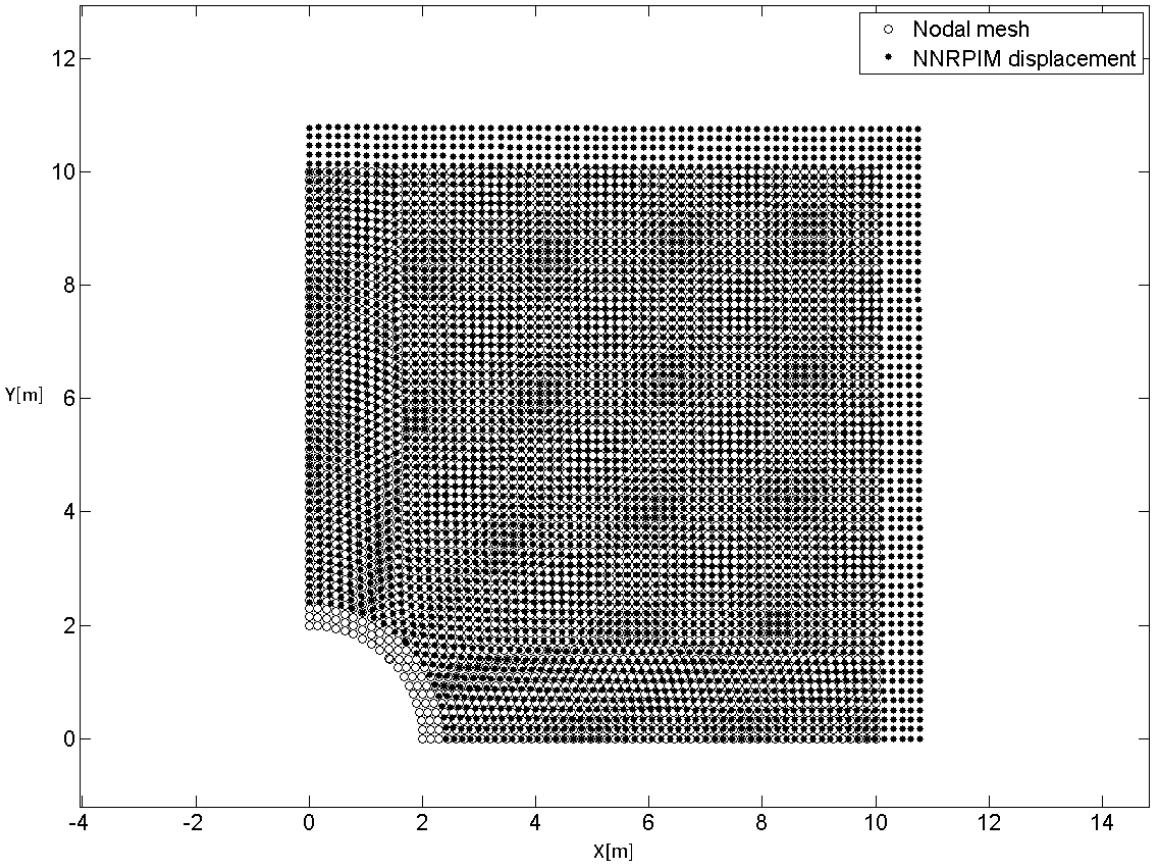

Figure 4.21: Plate with centre hole and diagonal boundary (right upper part – base model) - deformed and undeformed mesh.

The most outer node in the right upper corner had a displacement $u = 0,7487$ m in the xx direction and a displacement $v = 0,7487$ m in the yy direction. The deformed and undeformed mesh can be seen in Figure 4.23.

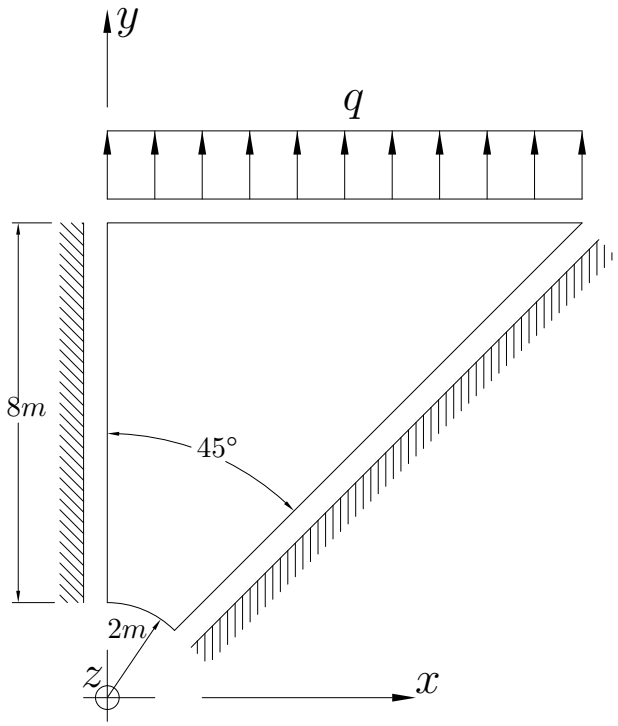

Figure 4.22: Plate with centre hole and diagonal boundary (right upper part – sliced model) - dimensions and boundary conditions.

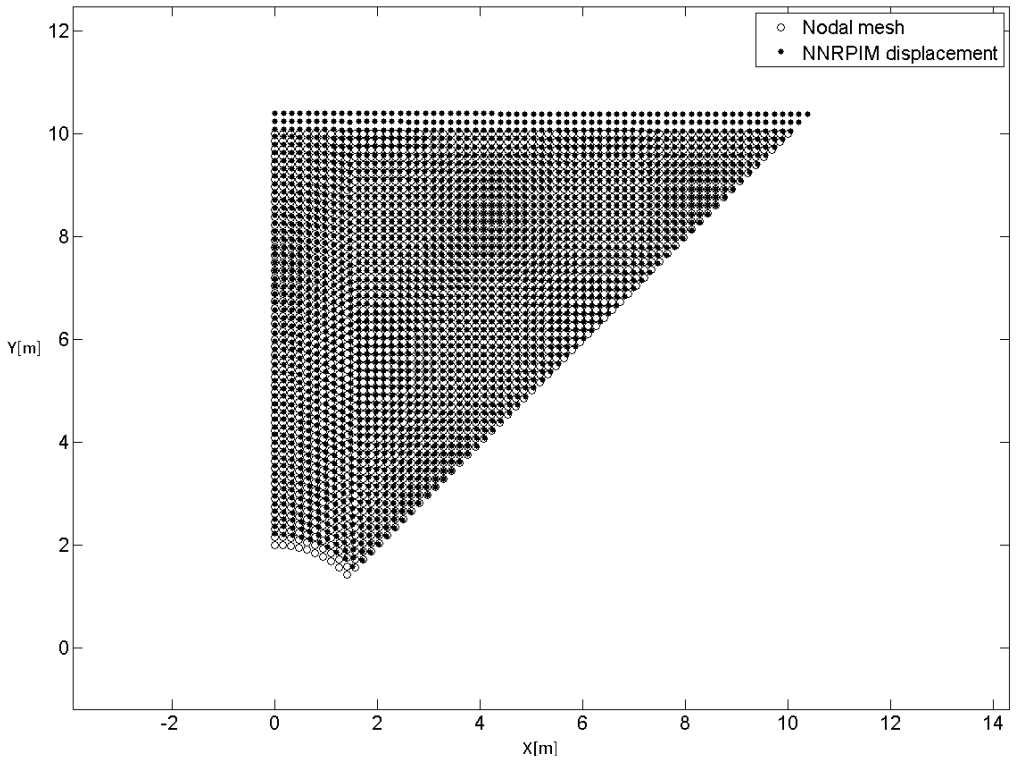

Figure 4.23: Plate with centre hole and diagonal boundary (right upper part – sliced model) - deformed and undeformed mesh.

4.2 Non-linear examples

In this section non-linear examples are analysed, using the incremental procedure.

4.2.1 Cantilever beam

The first problem is the classic cantilever beam. This problem is used to verify the quality of the results, considering the use of an approximate non-linear method.

The dimensions and boundary conditions are shown in Figure 4.24. The Young modulus E used is 10 MPa and the Poisson ratio ν is 0,3. It is considered plane stress analysis. The load per unit length q used is 40 KN/m.

In Figure 4.25, is compared the theoretical displacement [9] with the NNRPIM displacement for different mesh sizes, using 1000 increments. It is clear that the first mesh used (205 nodes) is enough for the problem. It is also clear that the NNRPIM solution converges to a value different from the analytical solution, being the error relative to the exact solution around 14%. Next the increments were studied (see Figure 4.26) for the mesh with 205 nodes. The optimal increment number determined is 500, which will be the reference increment number used from now on.

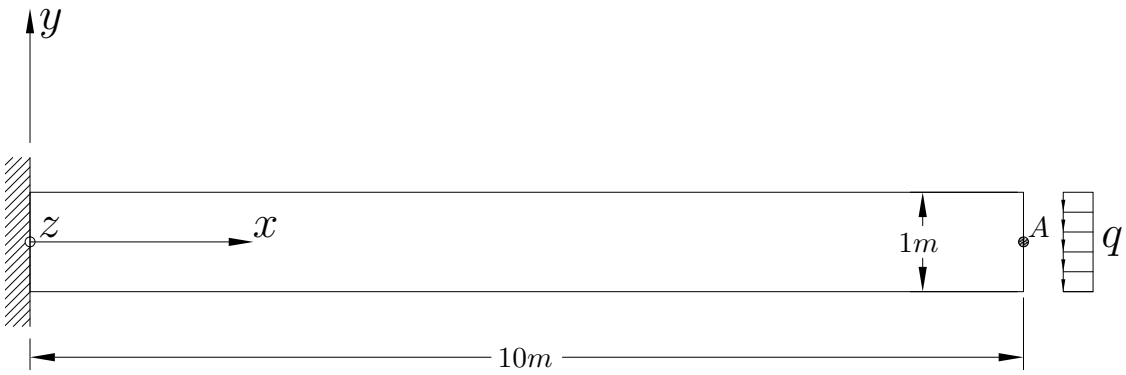

Figure 4.24: Cantilever beam for non-linear analysis: dimensions and boundary conditions.

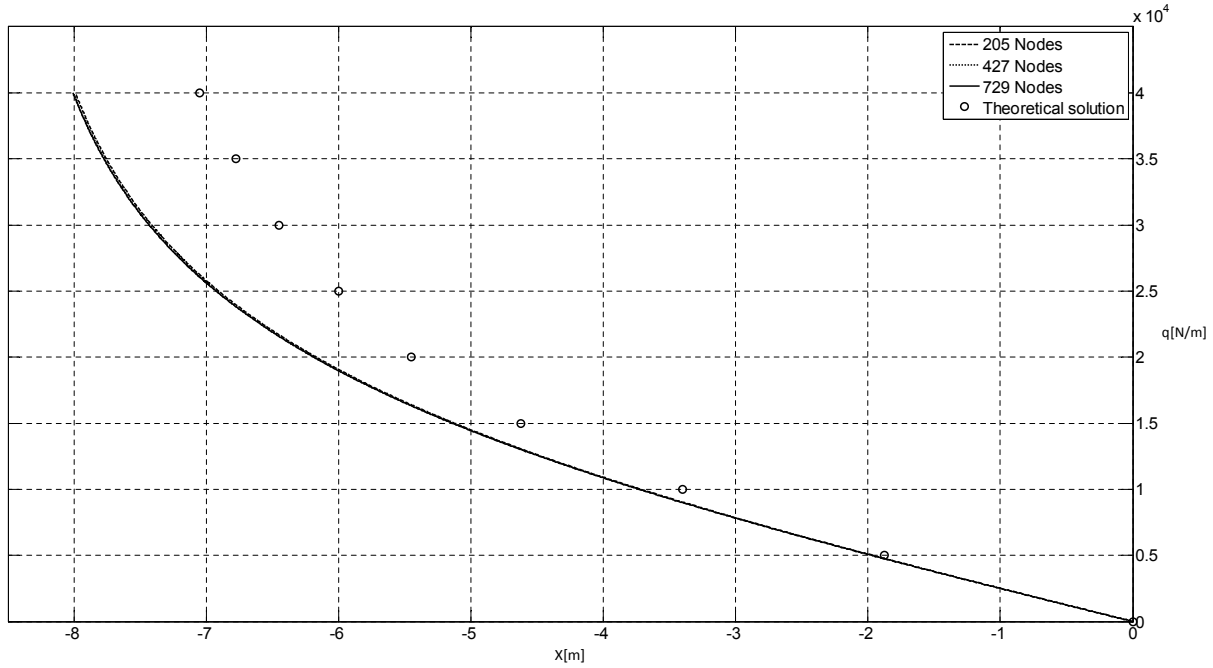

Figure 4.25: Comparison between theoretical displacement and NNRPIM displacement for various mesh sizes using 1000 increments.

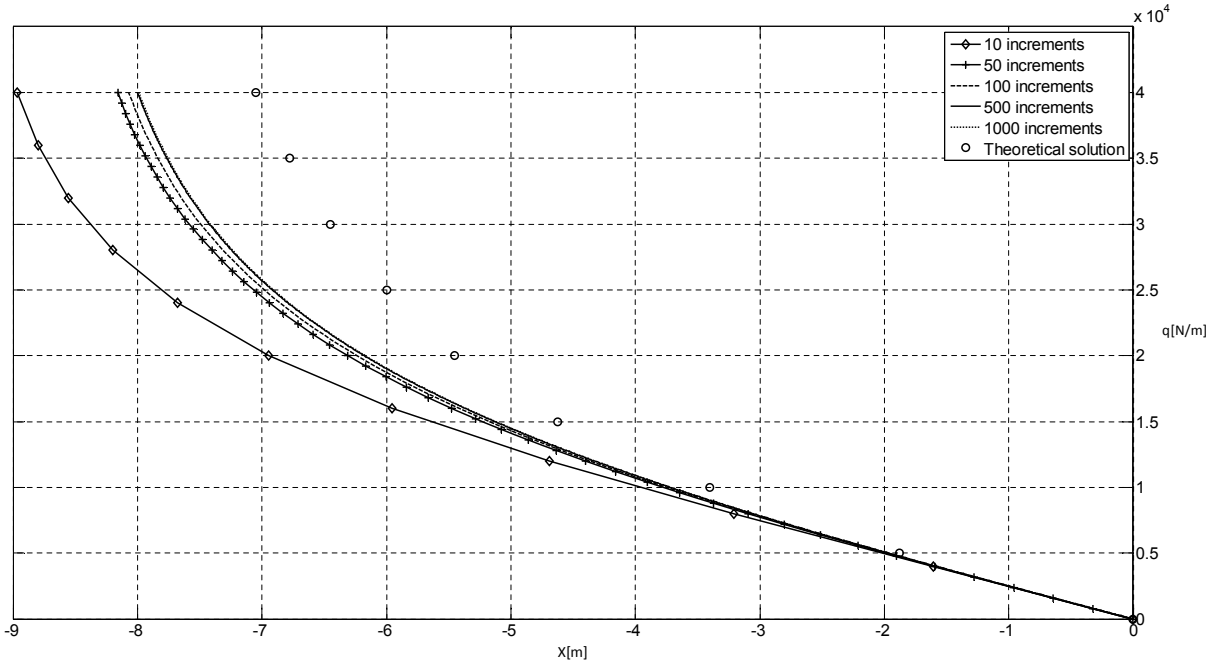

Figure 4.26: Comparison between theoretical displacement and NNRPIM displacement for various numbers of increments with a mesh of 205 nodes.

4.2.2 Extension of perforated plate

The perforated plate example [89] is studied. In [89], the example is analysed using an elasto-plastic deformation model and plain stress assumptions. In this work, it is considered an elasto-static plane stress analysis. It will be used to confirm if the deformation occurs in a similar way. The dimensions and boundary conditions are presented in Figure 4.27.

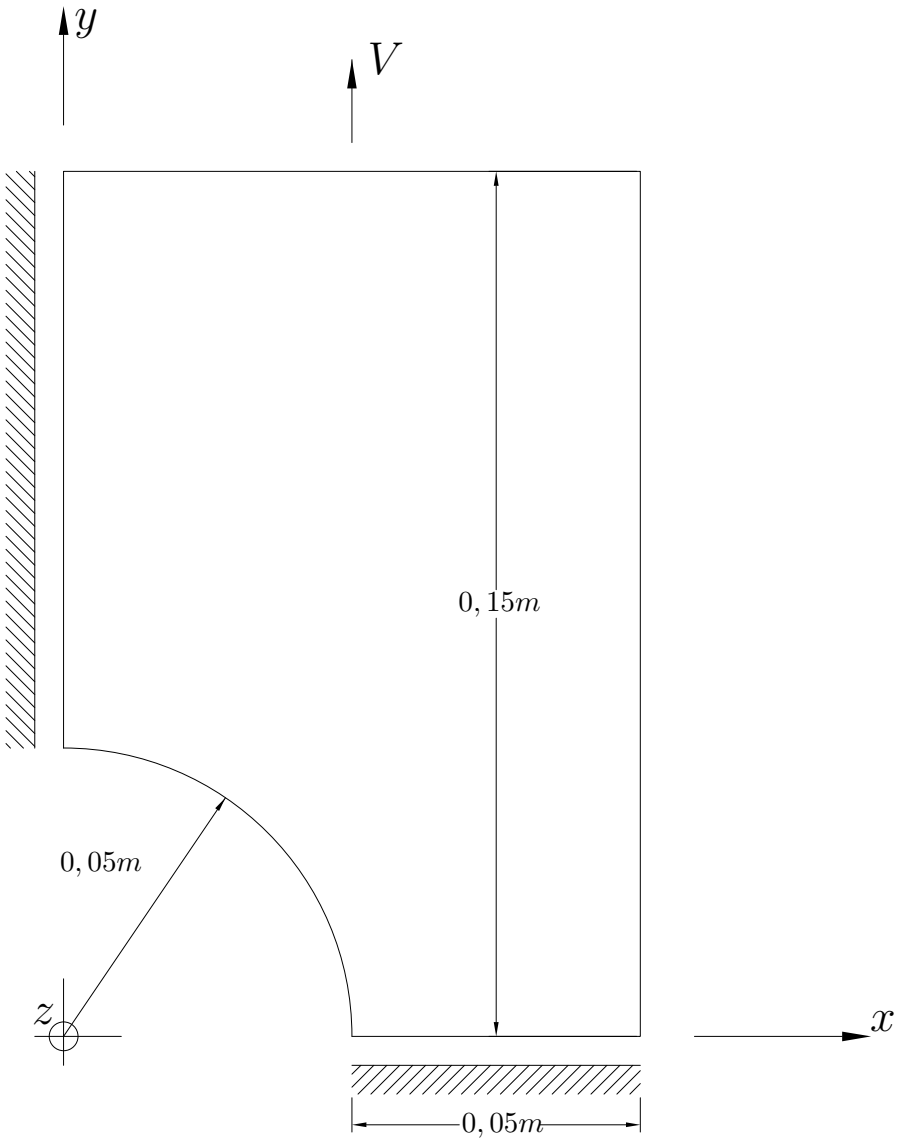

Figure 4.27: Perforated plate for non-linear analysis: dimensions and boundary conditions.

The Young modulus E used is 100 Pa, and the Poisson ratio ν is 0,3. The imposed displacement V is 0,05 m. The mesh applied has 1247 nodes. In Figure 4.28 is shown the evolution of the deformation.

By comparison with the solution obtained in [89], it is possible to visualize that the evolution of the deformation follows the same path, being in general less emphasized.

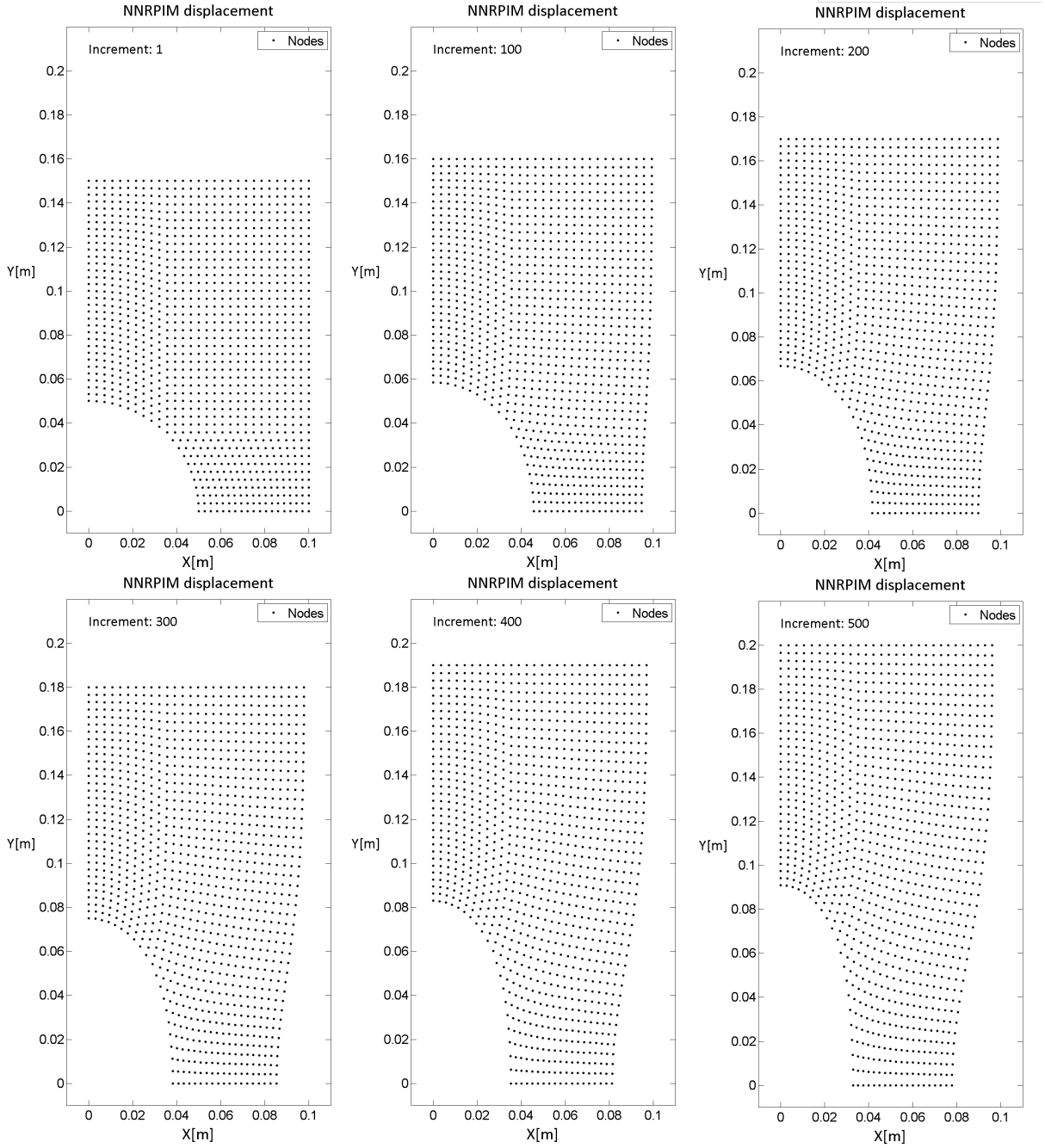

Figure 4.28: Evolution of the deformation on the perforated plate.

4.3 Contact examples

4.3.1 Cantilever beam contacting a rigid foundation

The first problem considering contact is the classic cantilever beam, in this case contacting a rigid foundation [90] – a Signorini problem.

The dimensions and boundary conditions are shown in Figure 4.29. The Young modulus E used is 30 KPa, and the Poisson ratio ν is 0,3. It is considered plane stress analysis. The load per unit length q used is 1 N/m. The distance between the beam and the boundary δ is 0,01 m.

The analytical contact start L_C from thick beam theory [90] is 21,37 m. This value is used as a reference.

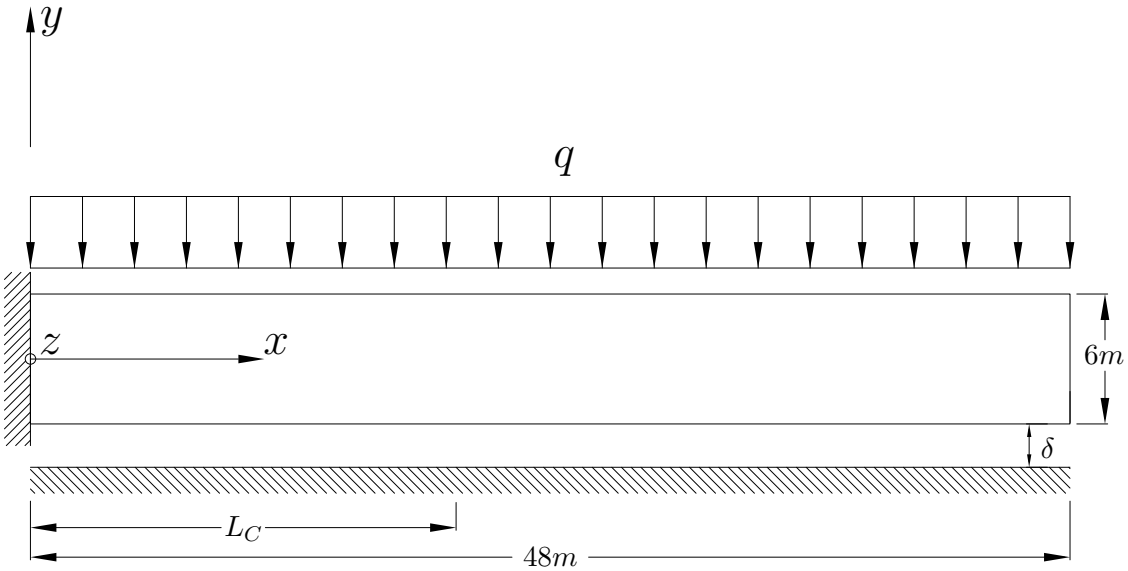

Figure 4.29: Cantilever beam contacting a rigid foundation: dimensions and boundary conditions.

A comparison between the analytical contact pressure [90], and the NNRPIM contact pressure is presented in Figure 4.30. It was used a mesh of 2193 nodes.

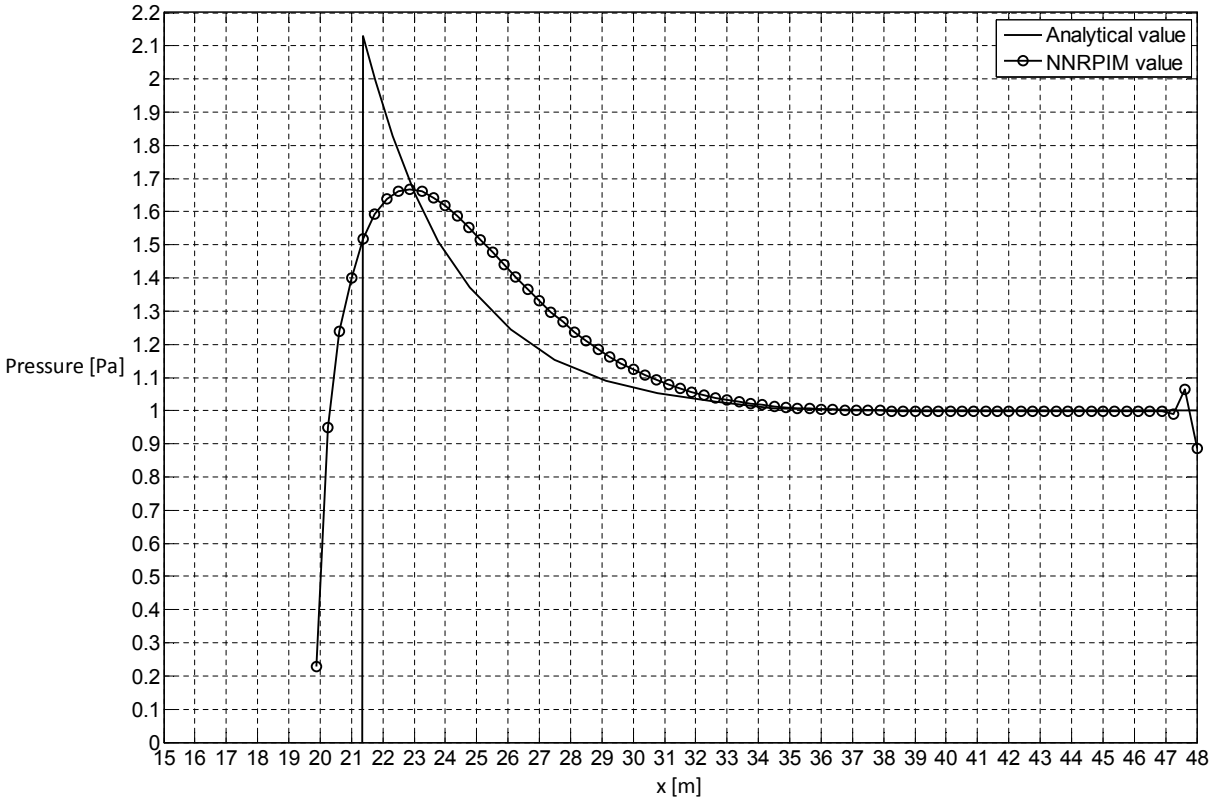

Figure 4.30: Contact pressure for cantilever beam contacting a rigid foundation.

The start of contact obtained with NNRPIM is 19,87 m, 7% less than the reference value.

4.3.2 Cylinder contacting a flat surface

The problem of an infinitely long cylinder, resting in a flat surface is analysed (Signorini problem). Due to the symmetry of the problem only one quarter is analysed. The dimensions and boundary conditions are shown in Figure 4.31. The cylinder is subjected to a concentrated load on top, which is converted to a load per unit length in the quarter analysed.

The Young modulus E used is 2 KPa, and the Poisson ratio ν is 0,3. It is considered a case of plane strain analysis. The concentrated load is 1600 N, so the load per unit length q used is 100 N/m.

The Hertz solution for the contact pressure is [67]

$$P = \frac{2Q}{\pi b_h^2}\sqrt{(b_h^2 - x^2)} \tag{4.15}$$

where Q is the concentrated load and b_h is the semi-width of the contact surface.

The semi-width of the contact surface is defined as [67]

$$b_h = 2\sqrt{\frac{QR(1-\nu^2)}{E\pi}} \tag{4.16}$$

being R the radius of the cylinder.

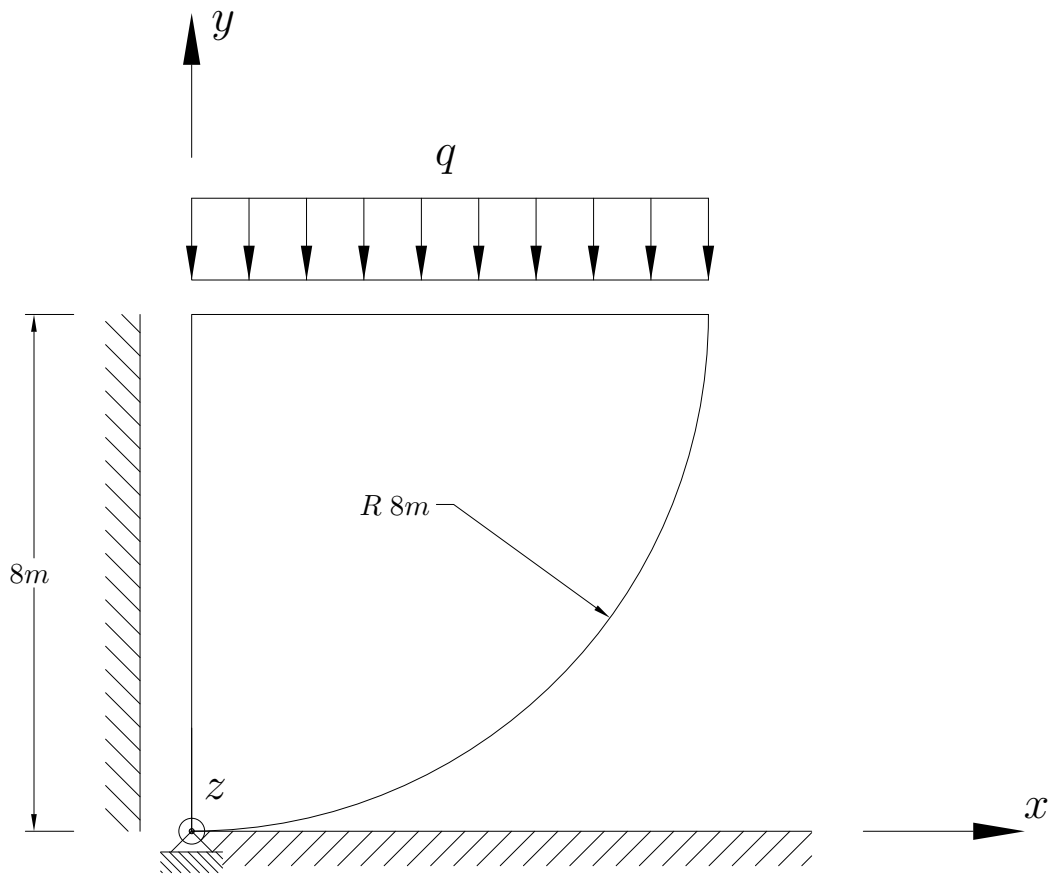

Figure 4.31: Cylinder contacting a flat surface: dimensions and boundary conditions.

The semi-width of the contact surface, calculated from equation (4.16) is 2,723 m.

In Figure 4.32 is represented the analytical contact pressure obtained from equation (4.15), and the contact pressure obtained with the NNRPIM, for a mesh of 3436 nodes. The contact semi-width obtained with NNRPIM is 2,289 m, 16% smaller than the theoretical value.

The applied load per unit length vs. the contact surface semi-width is represented in Figure 4.33, and compared to the analytical value obtained from equation (4.16).

In Figure 4.34 is shown the evolution of the deformation and the contact of the cylinder.

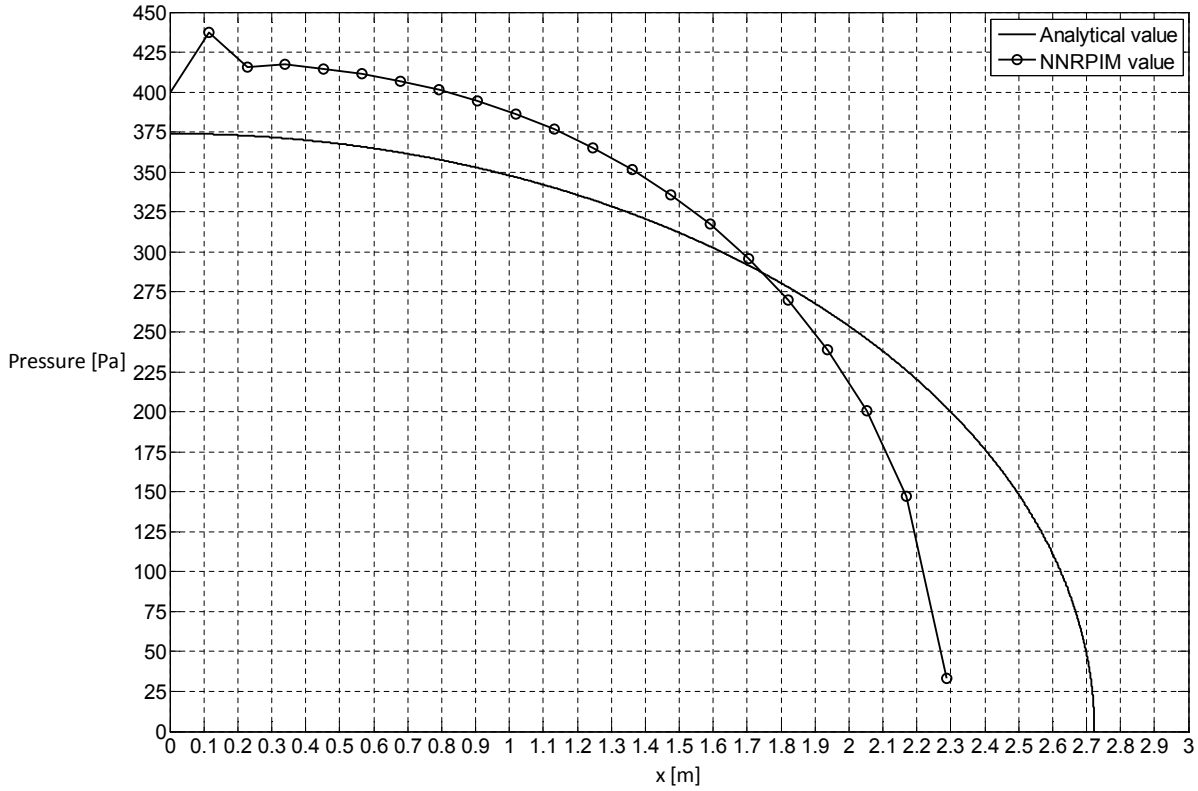

Figure 4.32: Contact pressure for cylinder contacting a flat surface.

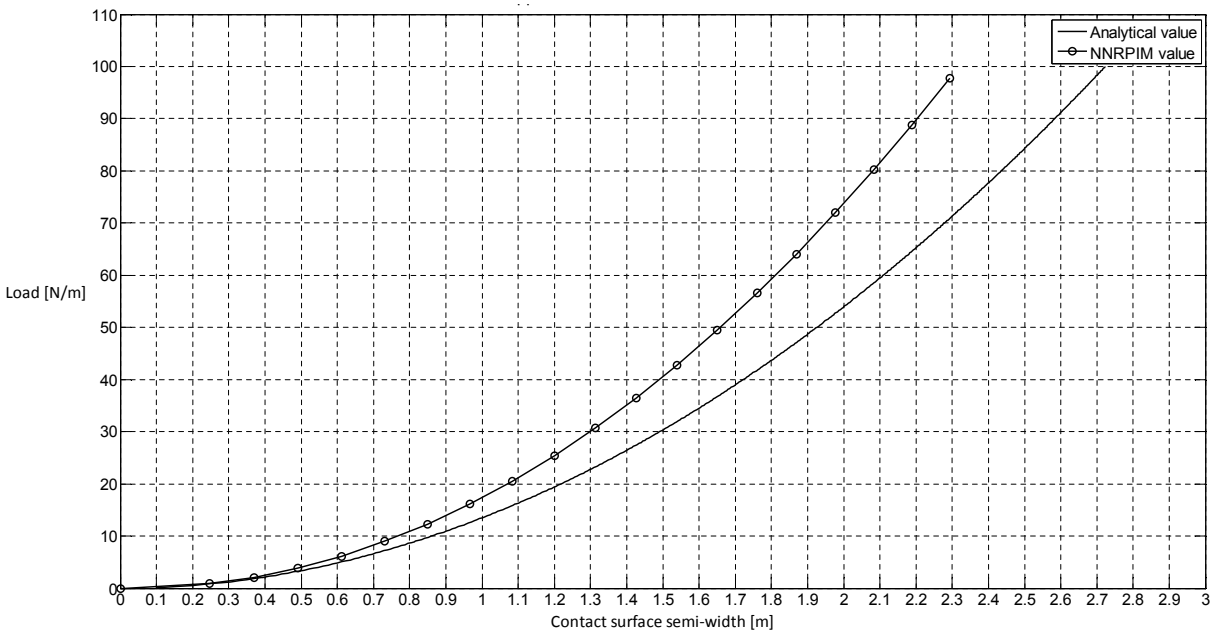

Figure 4.33: Applied load vs. contact surface half-width for cylinder contacting a flat surface.

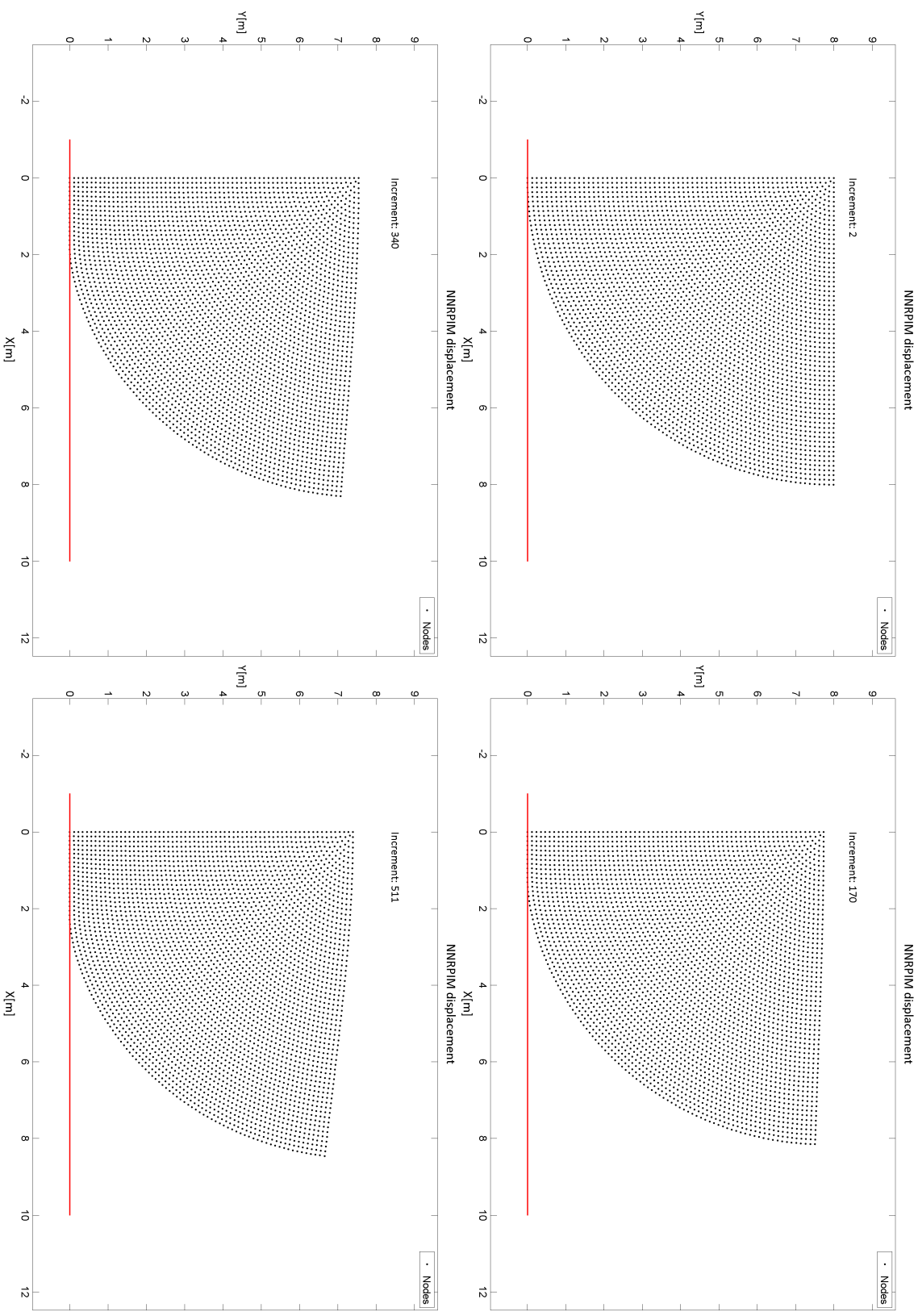

Figure 4.34: Evolution of the deformation and the contact on the cylinder.

4.3.3 Ring confined to a square

This problem was created only with the purpose of testing the implemented hydrostatic pressure in the NNRPIM. A thick ring is constrained inside a square boundary. The dimensions and boundary conditions are exposed in Figure 4.35.

The Young modulus E used is 4 MPa, and the Poisson ratio ν is 0,3. It is considered a case of plane stress analysis. The hydrostatic pressure applied is 1 MPa. It was used a mesh of 1564 nodes. The evolution of the deformation and the contact is shown in Figure 4.36.

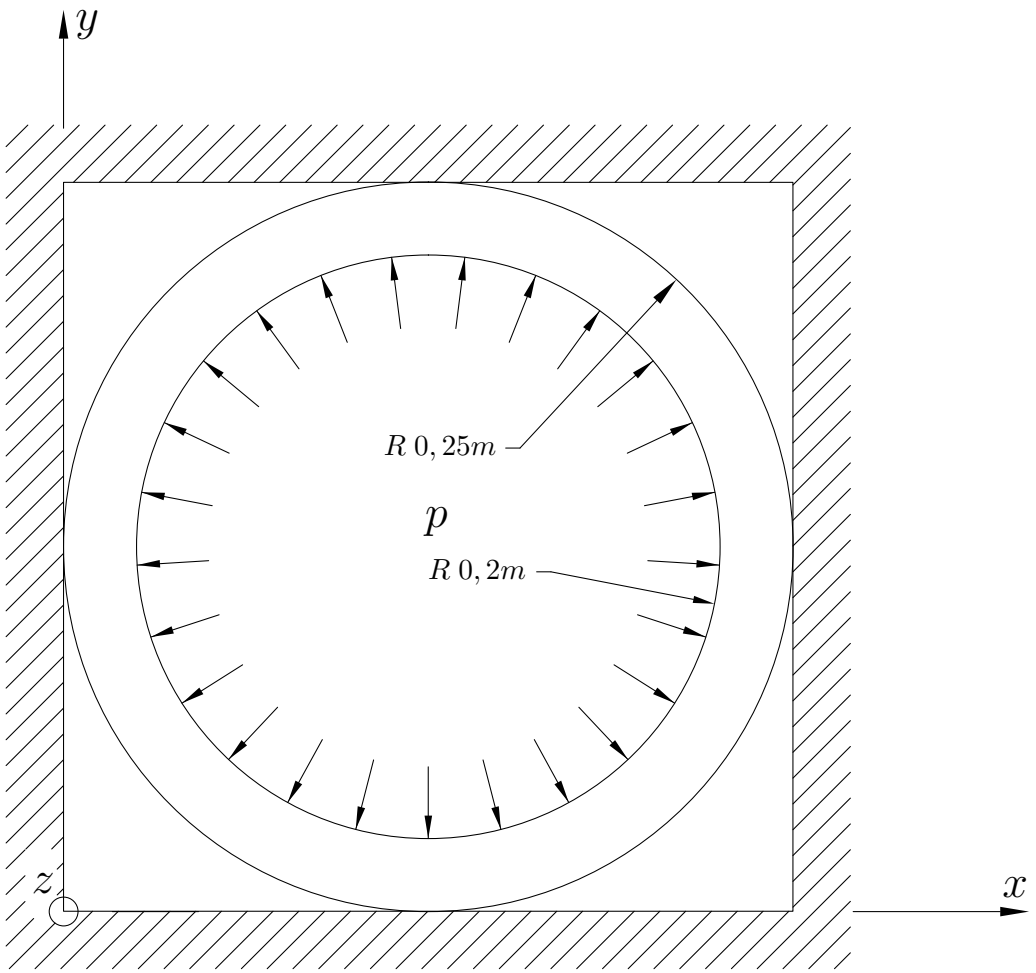

Figure 4.35: Ring confined to a square: dimensions and boundary conditions.

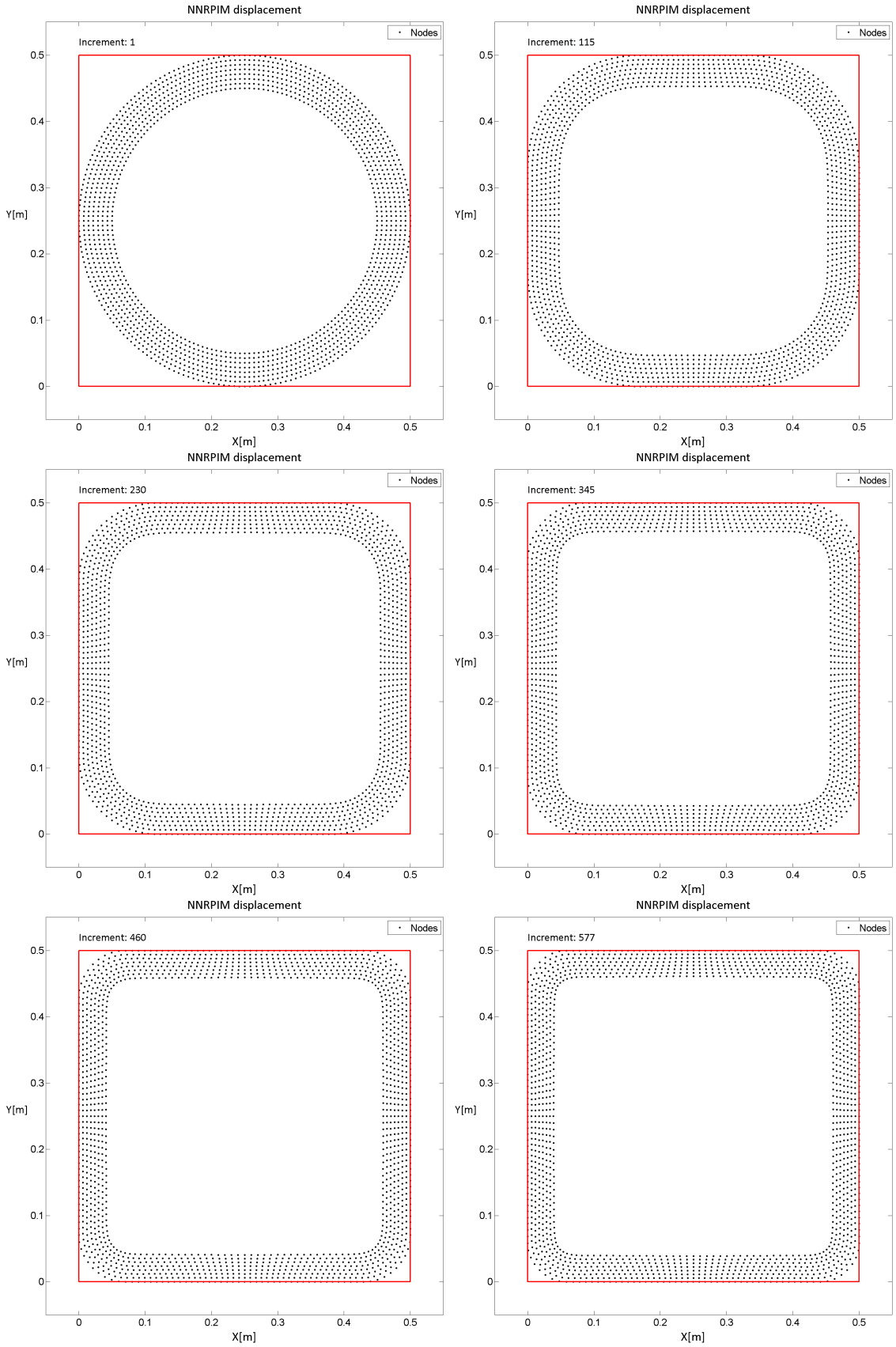

Figure 4.36: Evolution of the deformation and the contact on the ring confined to a square.

4.3.4 Sheet metal stamping

A sheet metal stamping process [91] is analysed. In [91] it is used a finite deformation elasto-plastic model. In this work only the non-linear approximated method considering elasto-static assumptions is used, however this problem is useful for testing the capabilities of the implemented contact detection algorithm.

The dimensions and boundary conditions are shown in Figure 4.37. The Young modulus E used is 206,9 GPa, and the Poisson ratio ν is 0,29. It is considered a case of plane stress analysis. The hydrostatic pressure applied is 1 GPa. In the source article, the pressure applied was 70 MPa, however, since the present analysis is far from the reference study, the results showed slight contact, when in fact the sheet metal should completely conform to the boundary. The value founded for the pressure, so that the sheet metal conforms completely to the boundary in the applied algorithm is 1 GPa.

The boundary is defined resorting to a cubic function $f(x)$ of type

$$y = \left(\frac{(x-b)}{a}\right)^3 - c \tag{4.17}$$

where a, b and c are constant parameters that define the cubic function.

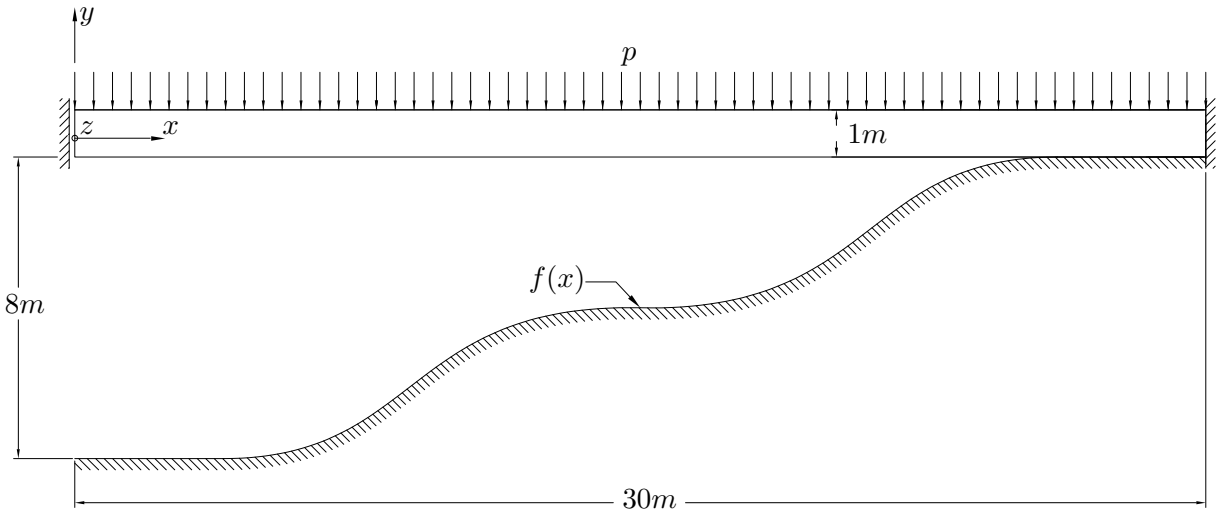

Figure 4.37: Sheet metal stamping: dimensions and boundary conditions.

The boundary is divided in four distinct parts, each one defined by an equation equal to (4.17), where only the constant parameters changes.

As so, the boundary is defined as

$$1st\ section \quad \left(\frac{x-1,5}{6}\right)^3 - \frac{125}{16} \quad x \in [0,9] \tag{4.18a}$$

$$2nd\ section \quad \left(\frac{x-16,5}{6}\right)^3 - \frac{125}{32} \quad x \in [9,15] \tag{4.18b}$$

$$3rd\ section \quad \left(\frac{x-13,5}{6}\right)^3 - \frac{251}{64} \quad x \in [15,21] \tag{4.18c}$$

$$4th\ section \quad \left(\frac{x-28,5}{6}\right)^3 - \frac{1}{64} \quad x \in [21,30] \tag{4.18d}$$

For more information on the determination of the point of contact in this boundary, refer to Appendix C.

In Figure 4.38 is shown the direction of the applied pressure in the final increment. The evolution of the deformation and the contact is presented in Figure 4.39 for a mesh of 605 nodes. It is visible that, besides the complex geometry of the boundary, the contact is well detected.

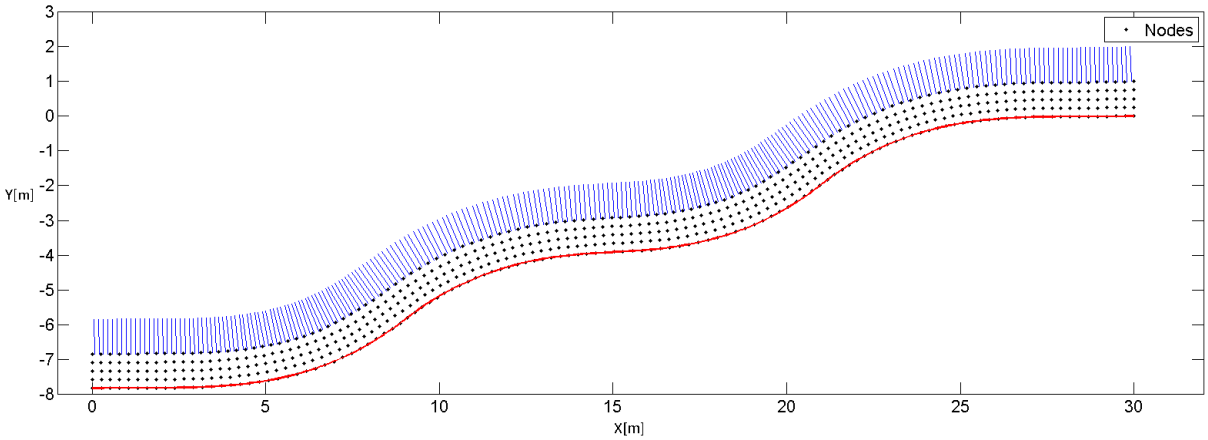

Figure 4.38: Pressure normals in sheet metal stamping in the last increment.

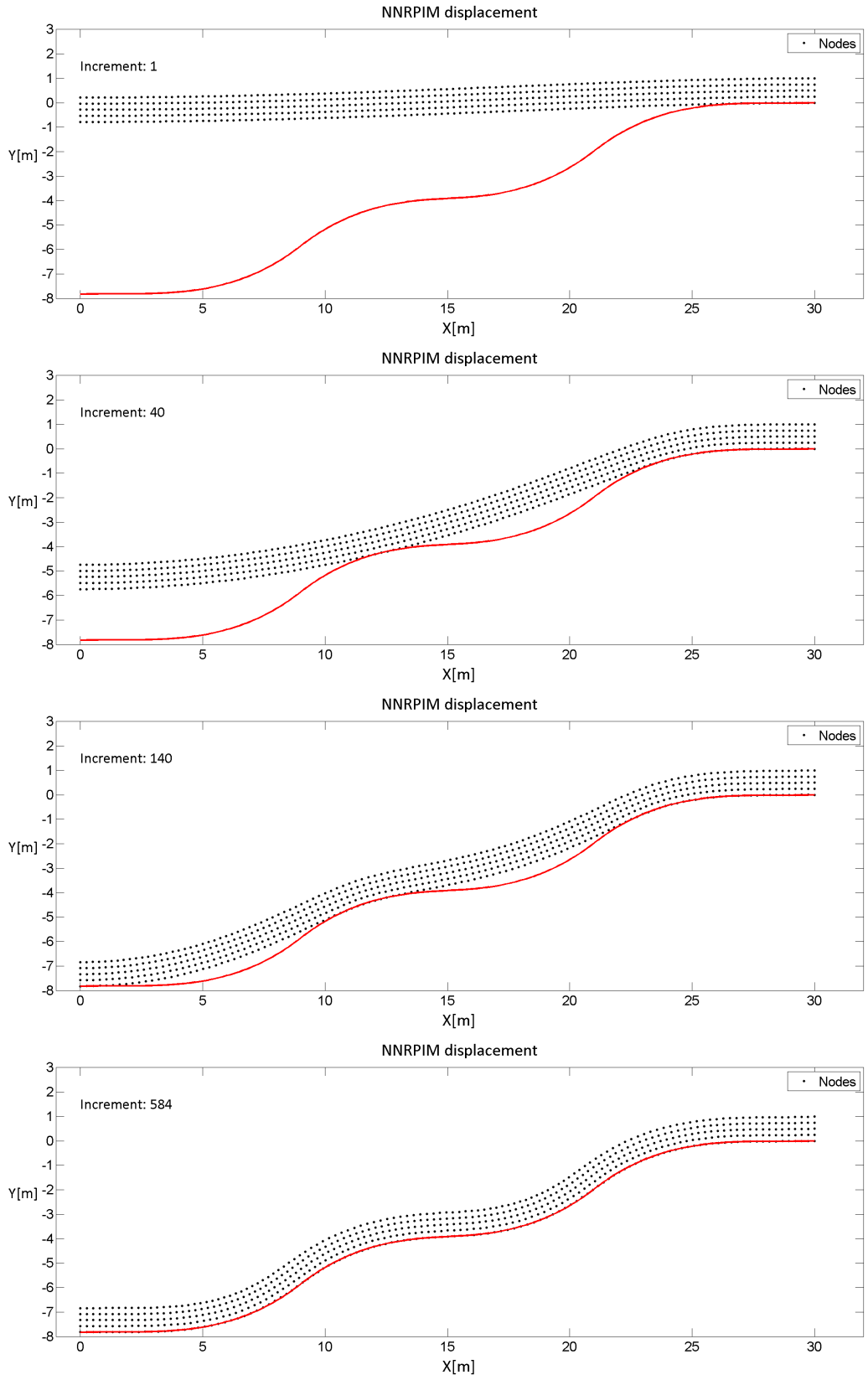

Figure 4.39: Evolution of the deformation and the contact on sheet metal stamping.

4.3.5 Cantilever beam contacting a rigid circular boundary

A node that contacts with a boundary may in future cease to contact with it. Therefore to test the ability of the algorithm to release the nodes when required, this example was created.

It is the classic cantilever beam, but now contacting a rigid circular boundary. Because of the geometry of the boundary, the contact point of the beam has to change with the increments. The dimensions and boundary conditions are presented in Figure 4.40. The boundary is defined using the circumference equation

$$(x-a)^2 + (y-b)^2 = r_c^2 \tag{4.19}$$

where (a, b) are the circumference centre coordinates.

The Young modulus E used is 10 MPa, and the Poisson ratio ν is 0,3. It is considered a case of plane stress analysis. The load per unit length q used is 40 KN/m. The evolution of the deformation and contact is shown in Figure 4.41, Figure 4.42 and Figure 4.43 for a mesh of 891 nodes. For more information about how to determine the position of the contact node, refer to Appendix B.

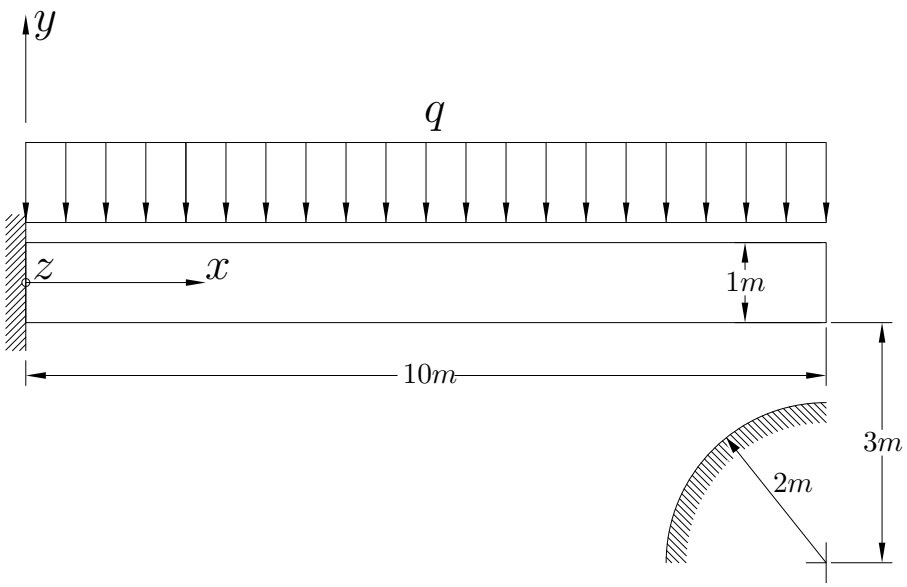

Figure 4.40: Cantilever beam contacting a rigid circular boundary: dimensions and boundary conditions.

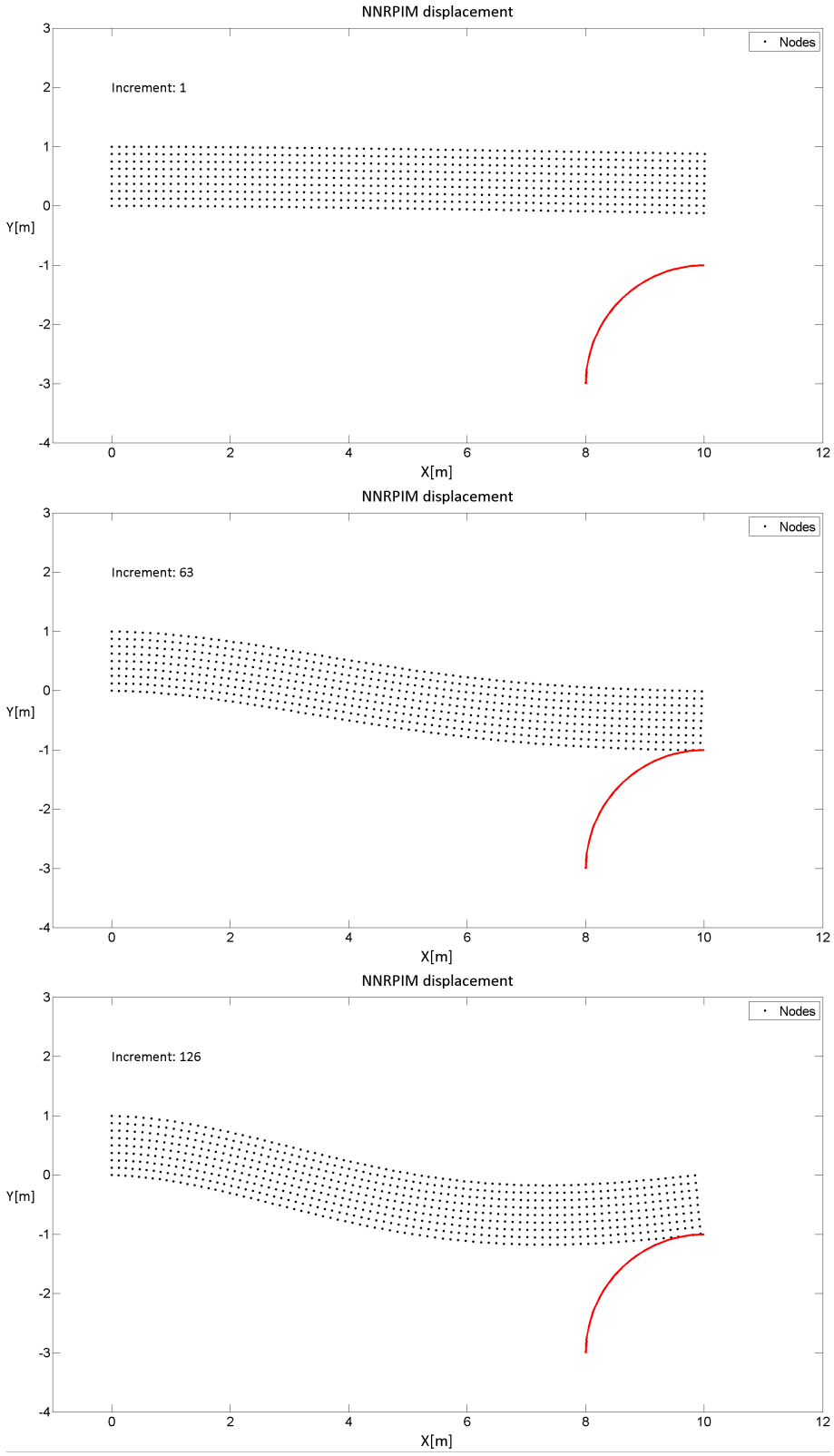

Figure 4.41: Evolution of the deformation and the contact on cantilever beam contacting a rigid circular boundary from first increment to increment 126.

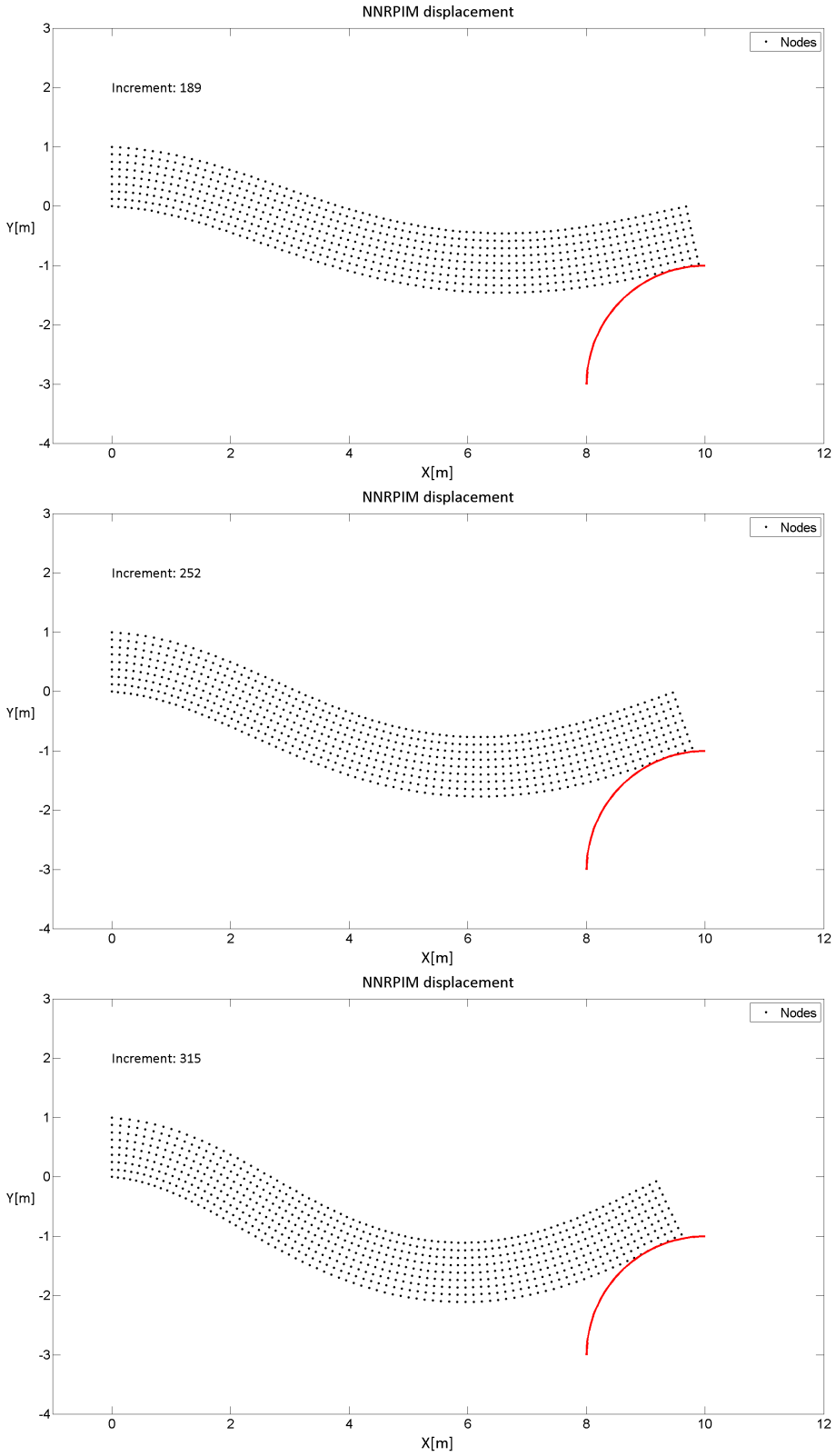

Figure 4.42: Evolution of the deformation and the contact on cantilever beam contacting a rigid circular boundary from increment 189 to increment 315.

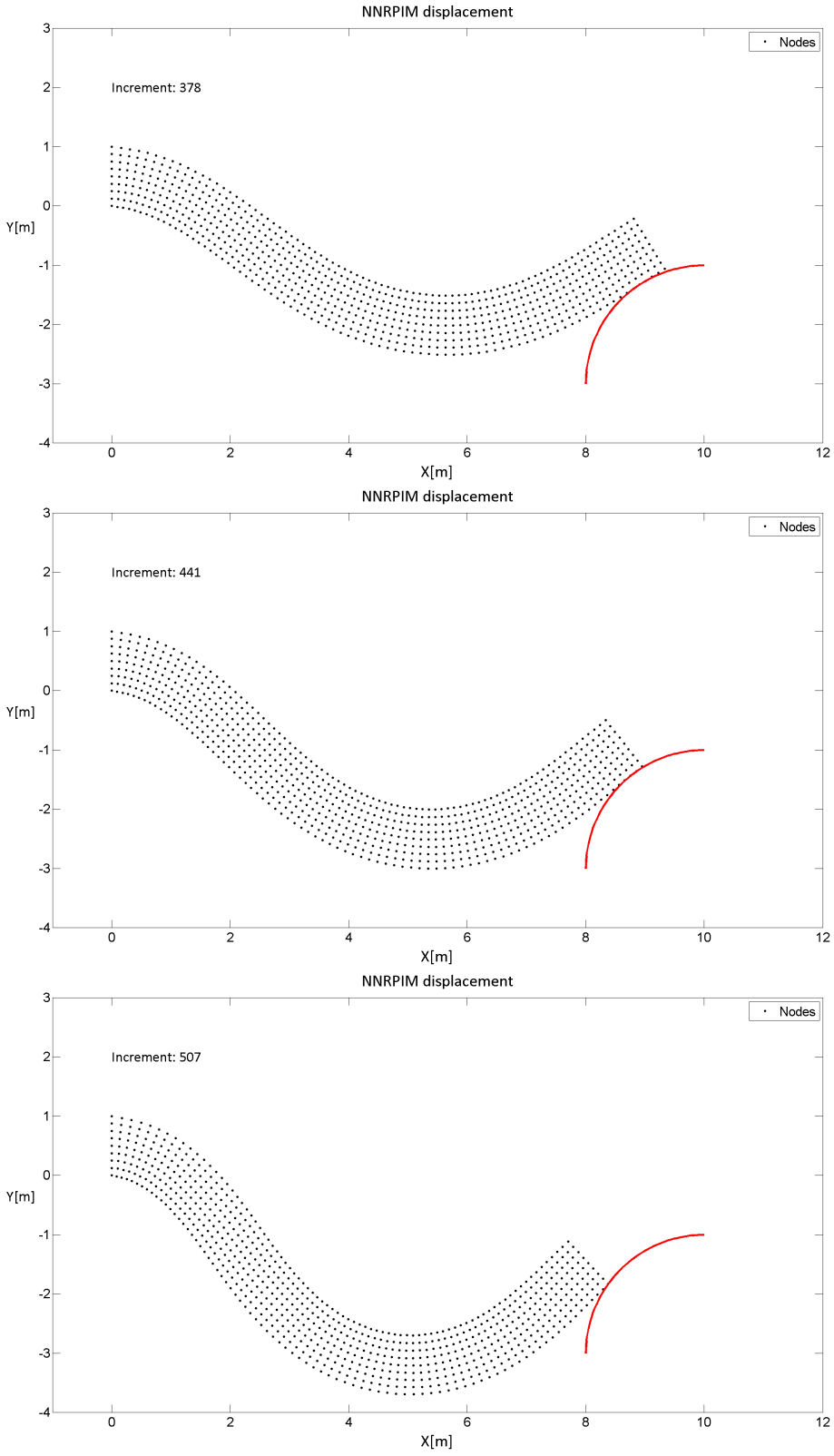

Figure 4.43: Evolution of the deformation and the contact on cantilever beam contacting a rigid circular boundary from increment 378 to last increment.

4.3.6 Block compression

The example of a block compression [92] was analysed. The block is made of rubber, and in the cited article is analysed using a large deformation hyperelastic model. In this work, the block compression will be used for contact purposes only, since the developed algorithm is not prepared for analysing hyperelastic materials.

The dimensions and boundary conditions are shown in Figure 4.44. The Young modulus E used is 4,0679 MPa considering the Saint-Venant Kirchhoff material [93]. The Poisson ratio ν used is 0,3. It is considered a case of plane strain analysis. The imposed displacement V is 0,08 m. Comparing with the problem dimensions the imposed displacement is exaggerated. This is done on purpose to increase the contact nodes. Also the boundaries are limited along xx direction so, the material will eventually deform around the boundaries.

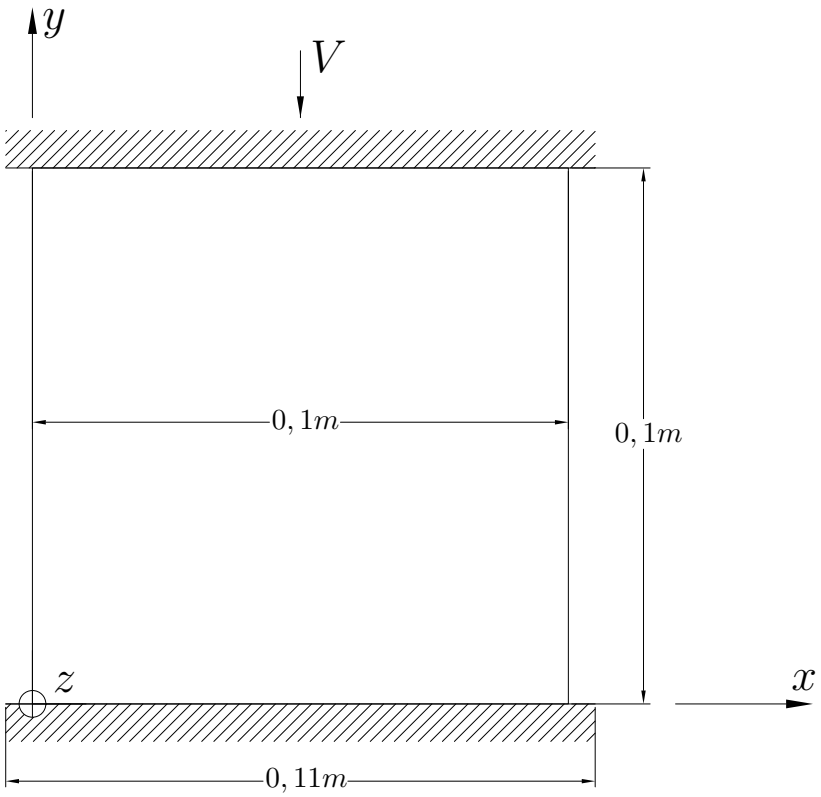

Figure 4.44: Block compression: dimensions and boundary conditions.

Since the proposed algorithm does not consider friction, this analysis would transform the square block into a rectangle block. In order to enforce contact to happen, the initial nodes and the contact nodes are locked along the xx direction. This can be viewed as a case of stick condition.

For more information about how to determine the position of the contact node, refer to Appendix A.

The evolution of the deformation and the contact for a mesh of 2601 nodes is presented in Figure 4.45 and Figure 4.46.

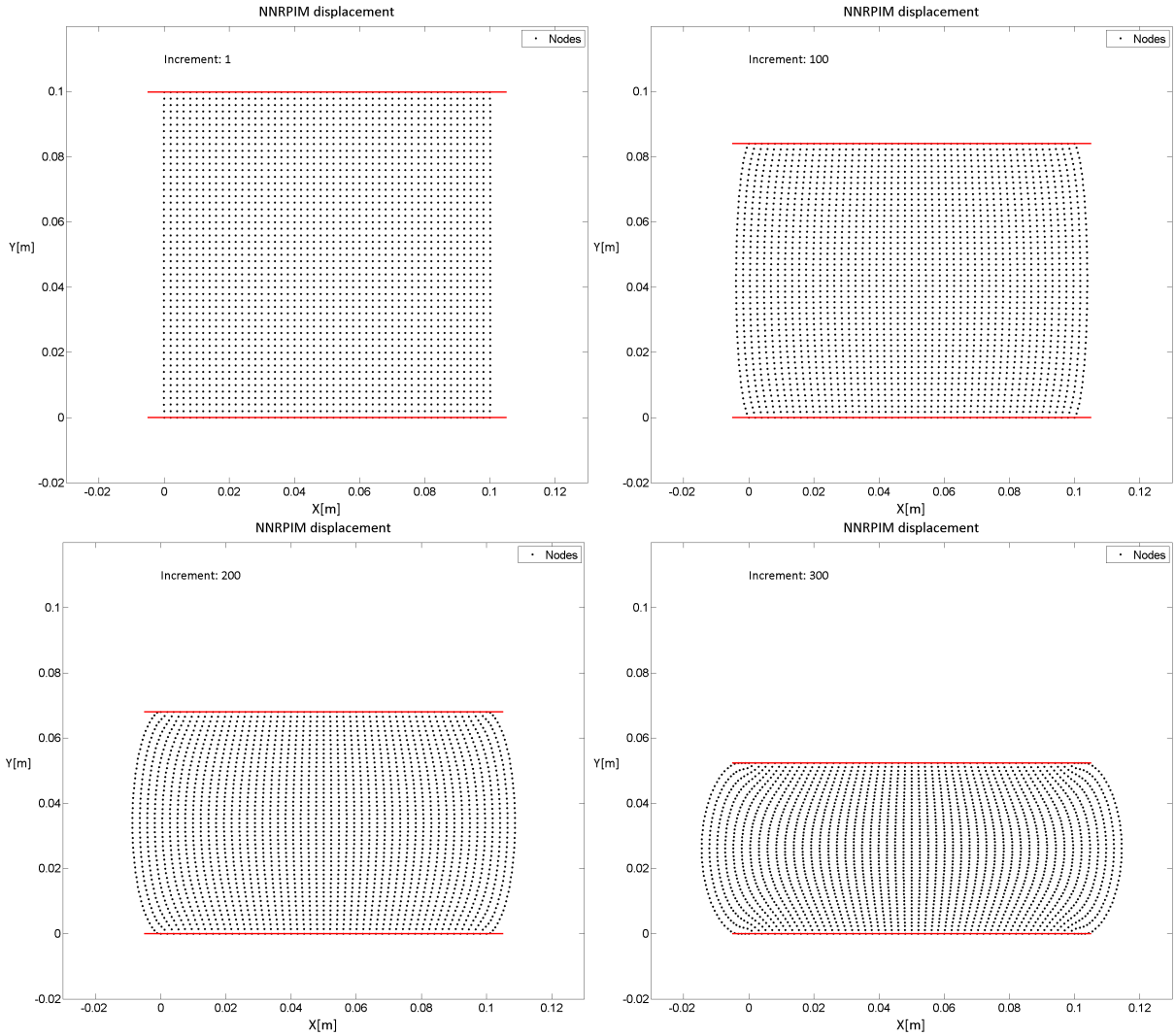

Figure 4.45: Evolution of the deformation and the contact on the block compression from first increment to increment 300.

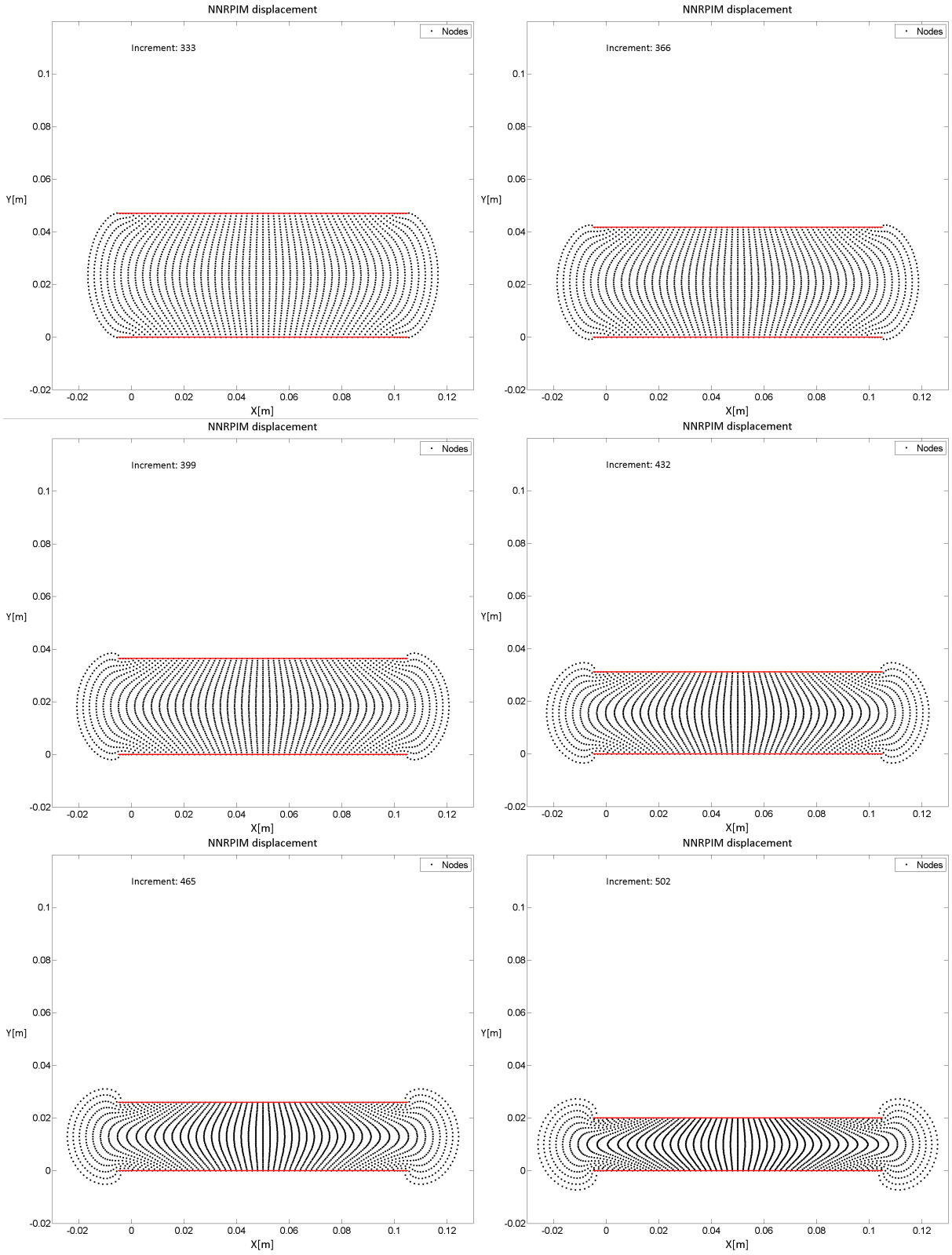

Figure 4.46: Evolution of the deformation and the contact on the block compression from increment 333 to last increment.

4.3.7 Ring compression

Next the rubber ring compression [92] is studied. Exactly as the previous example, it is analysed using a large deformation hyperelastic model in [92], which is not considered in this work. The material properties used are the same as the Block compression, only in this case a plane stress case is assumed. The dimensions and boundary conditions are shown in Figure 4.47.

The imposed displacement of the top boundary V is 0,069 m. Again the objective is to increase the deformation, to have more nodes contacting, and to see if at some point the middle section of the ring leaves the boundary, without touching itself, because the developed algorithm does not consider self-contact.

In this case, only initial nodes are locked along xx direction, in order to make the problem stable, by avoiding a matrix close to singular.

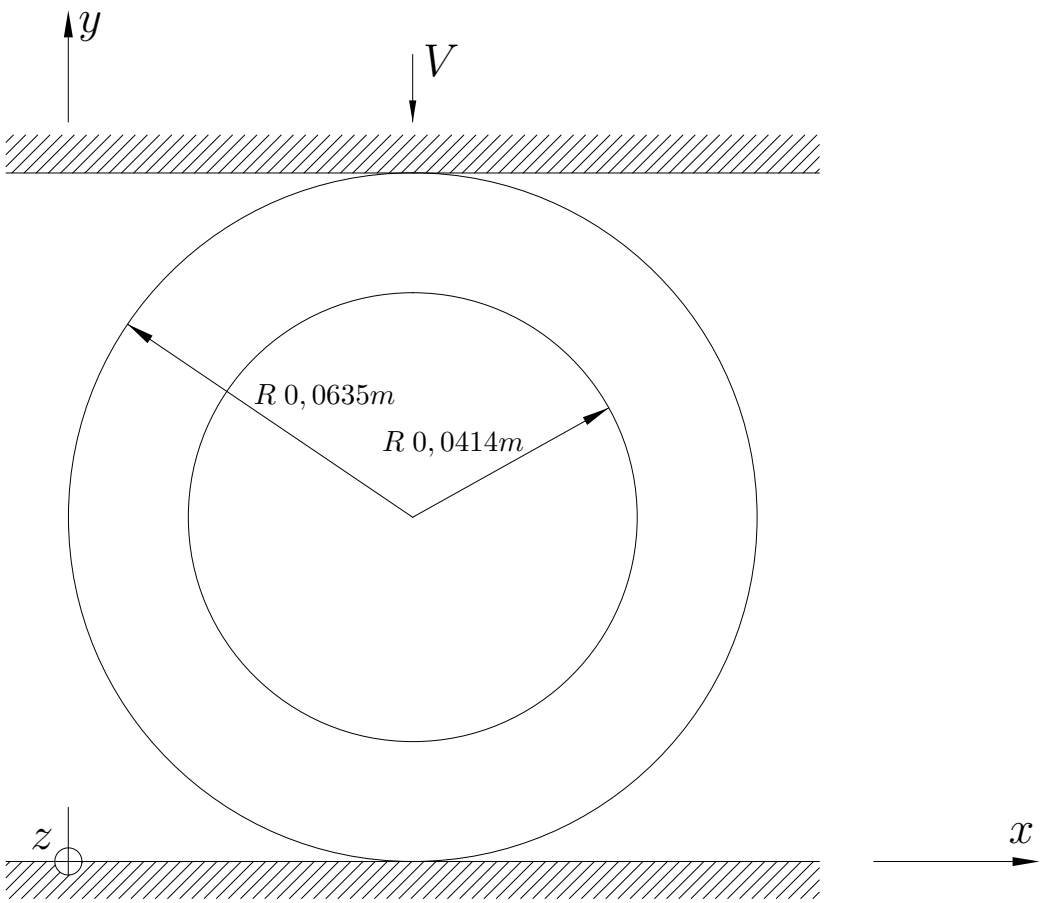

Figure 4.47: Ring compression: dimensions and boundary conditions

The evolution of deformation and contact for a mesh of 2308 nodes is presented in Figure 4.48 and Figure 4.49.

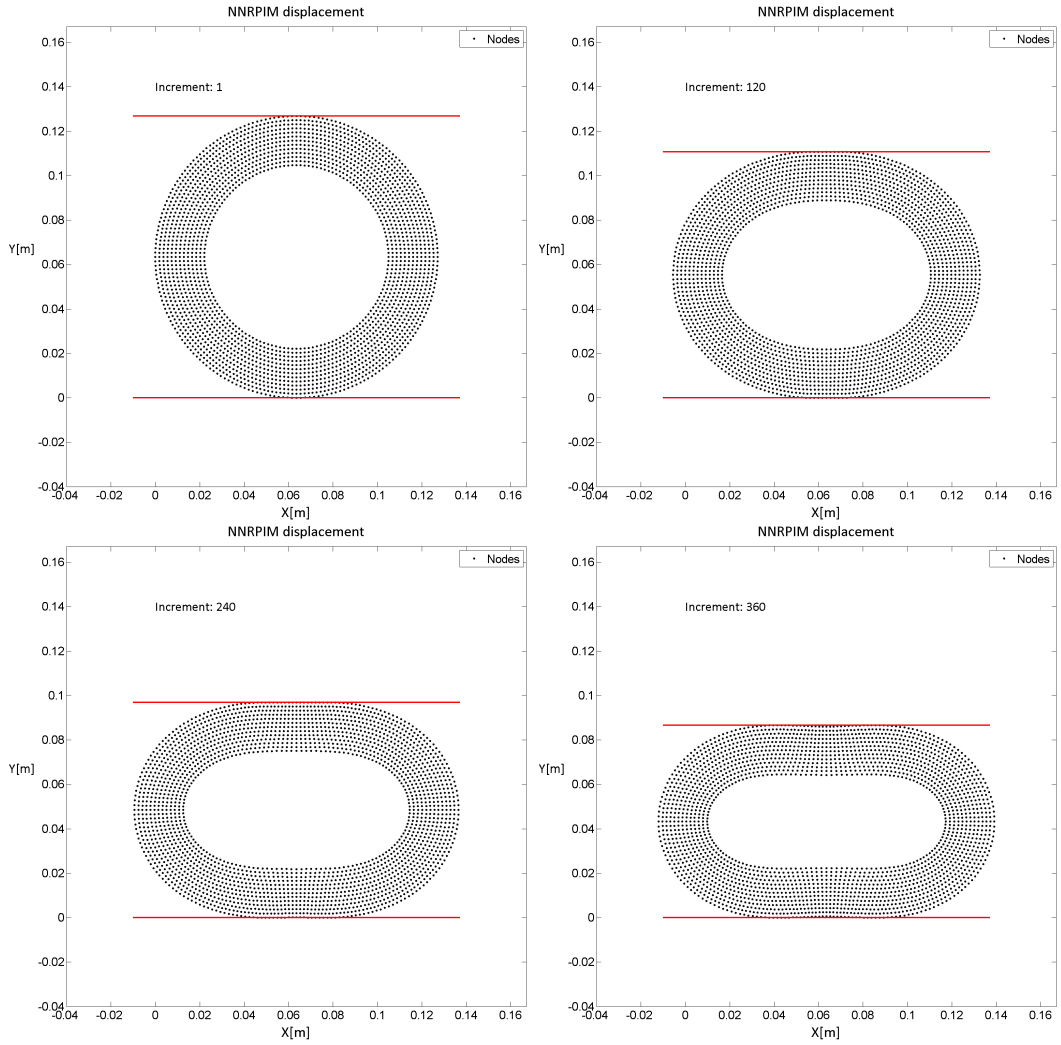

Figure 4.48: Evolution of the deformation and the contact on the ring compression from first increment to increment 360.

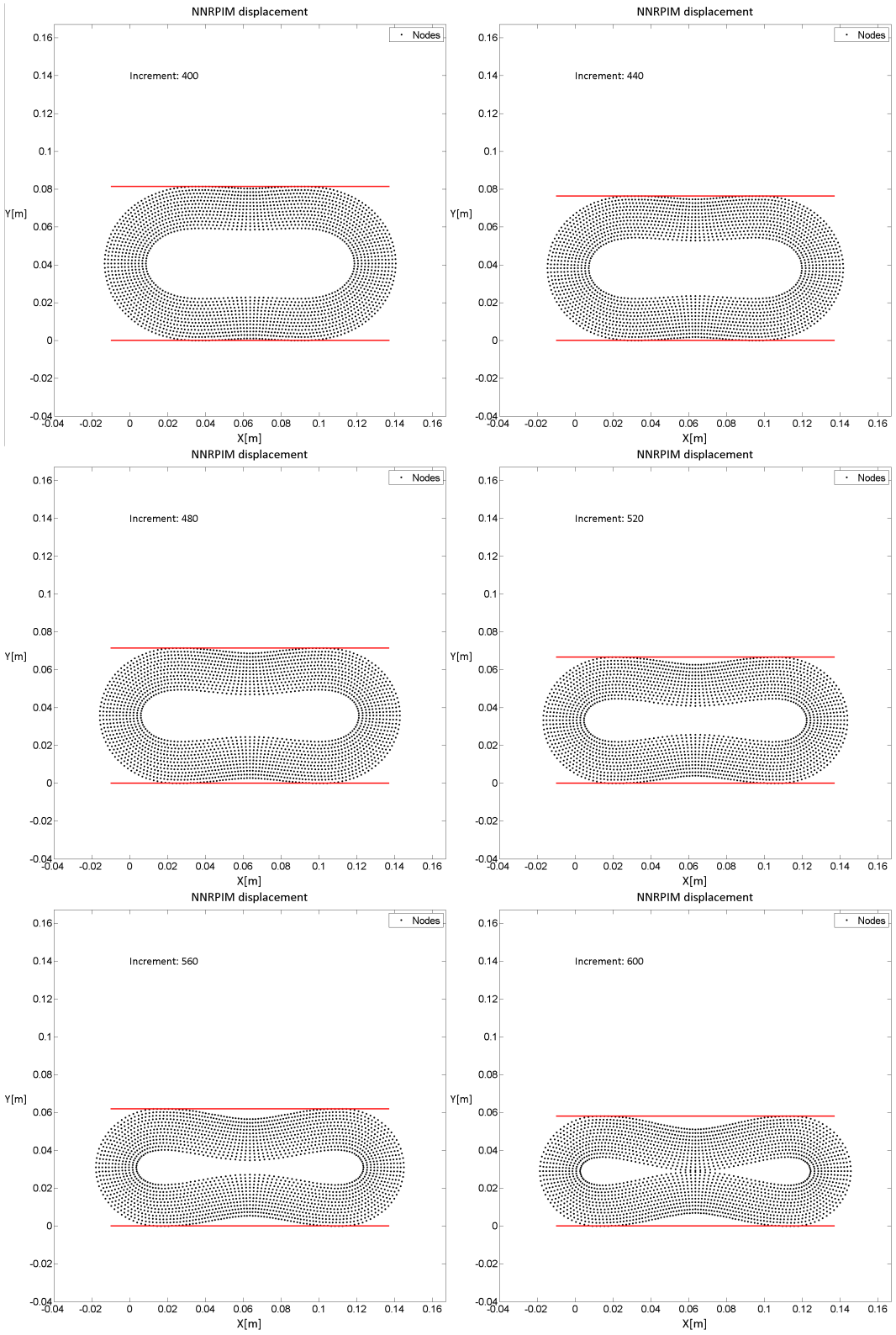

Figure 4.49: Evolution of the deformation and the contact on the ring compression from increment 400 to last increment.

4.3.8 Upsetting

An upsetting process was recreated based in [94], in which was used an axisymmetric formulation and the material considered perfectly plastic. In this work, an elasto-static non-linear approximation analysis will be used. Therefore the example is recreated just because of the contact complexity involved, a linear dynamic boundary and an asymptotic static boundary. The dimensions and boundary conditions are presented in Figure 4.50.

The Young modulus E used is 288 GPa, and the Poisson ratio ν is 0,3. It is considered both plane stress and plain strain analysis. The imposed displacement V is 0,0143 m, which is the necessary value for the top boundary to touch the lower boundary.

The top boundary is composed of three sections, two constant sections and one linear section. The linear section is defined using the linear equation in its standard form.

$$Ax + By = C \tag{4.20}$$

The bottom boundary is composed of three sections, two constants (one vertical and one horizontal) and one asymptotic function $f(x)$ of type

$$y = \frac{1}{-x + a} + b \tag{4.21}$$

where a and b are constant parameters that define the asymptotic function. For scaling purposes, the previous equation will be changed to

$$y = \left(\frac{1}{-1000x + a} + b \right) \frac{1}{1000} \tag{4.22}$$

The parameters a and b used are

$$\begin{cases} a = \dfrac{65}{6} \\ b = 6 \end{cases} \tag{4.23}$$

For further information on how to determine the contact point in the asymptotic boundary, refer to Appendix D.

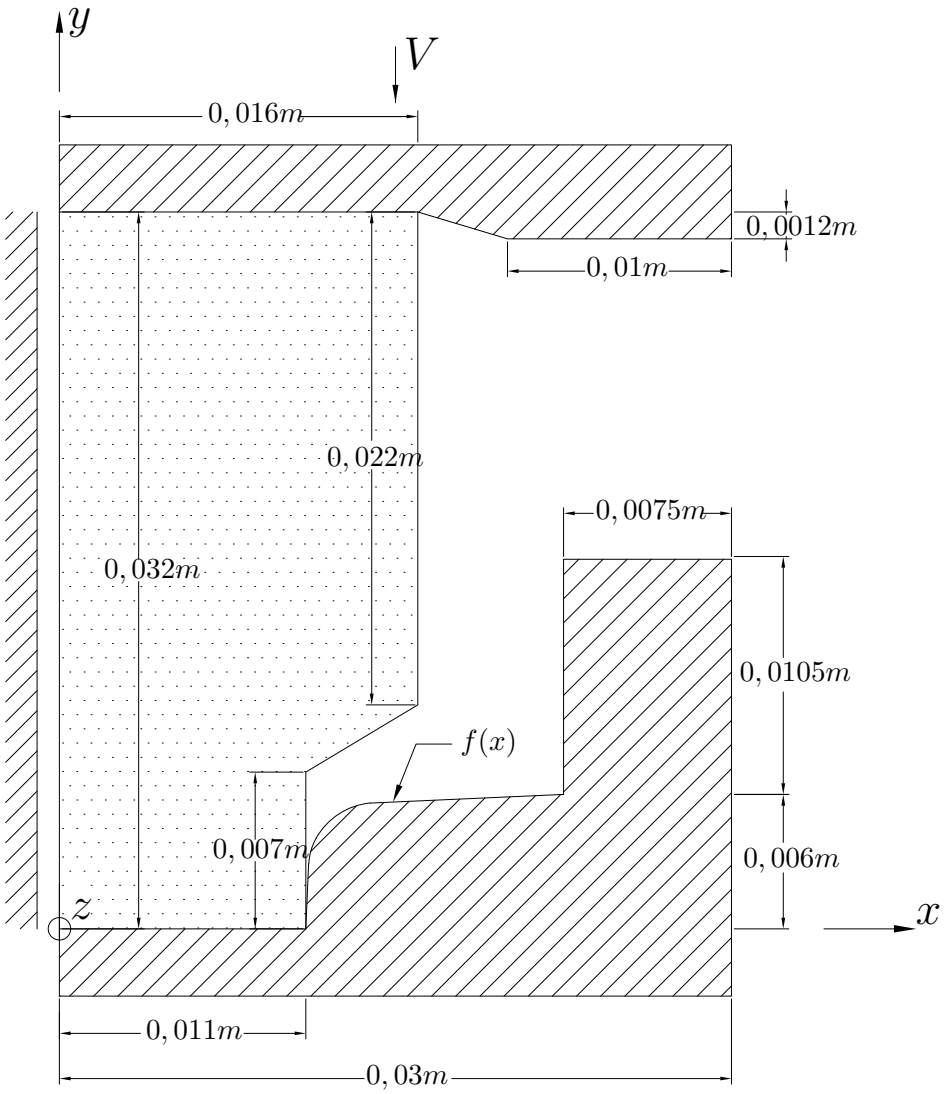

Figure 4.50: Upsetting: dimensions and boundary conditions.

The evolution of the deformation and the contact is presented in Figure 4.51 for plane stress and in Figure 4.52 for plane strain analysis.

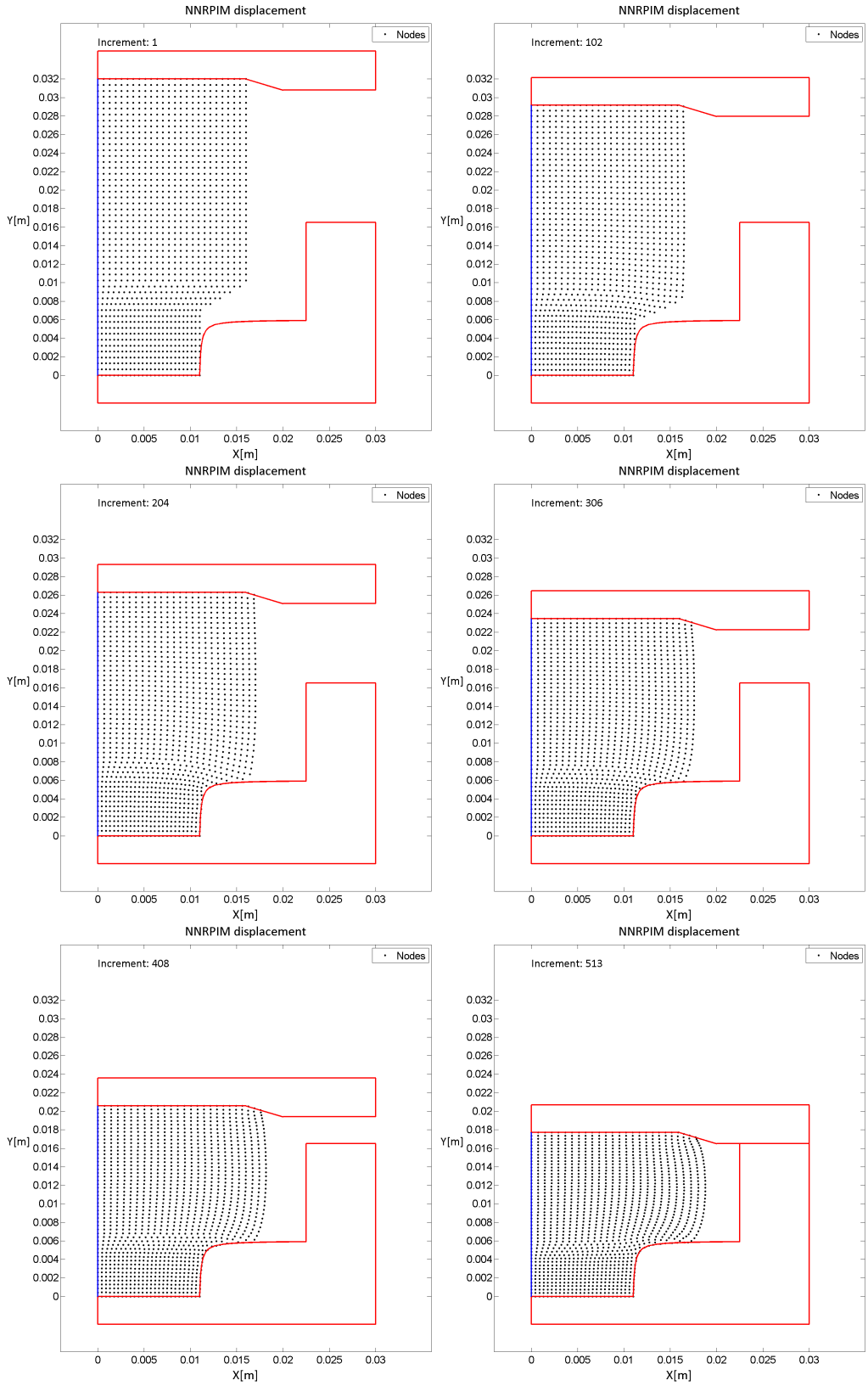

Figure 4.51: Evolution of the deformation and the contact on the upsetting for plane stress analysis.

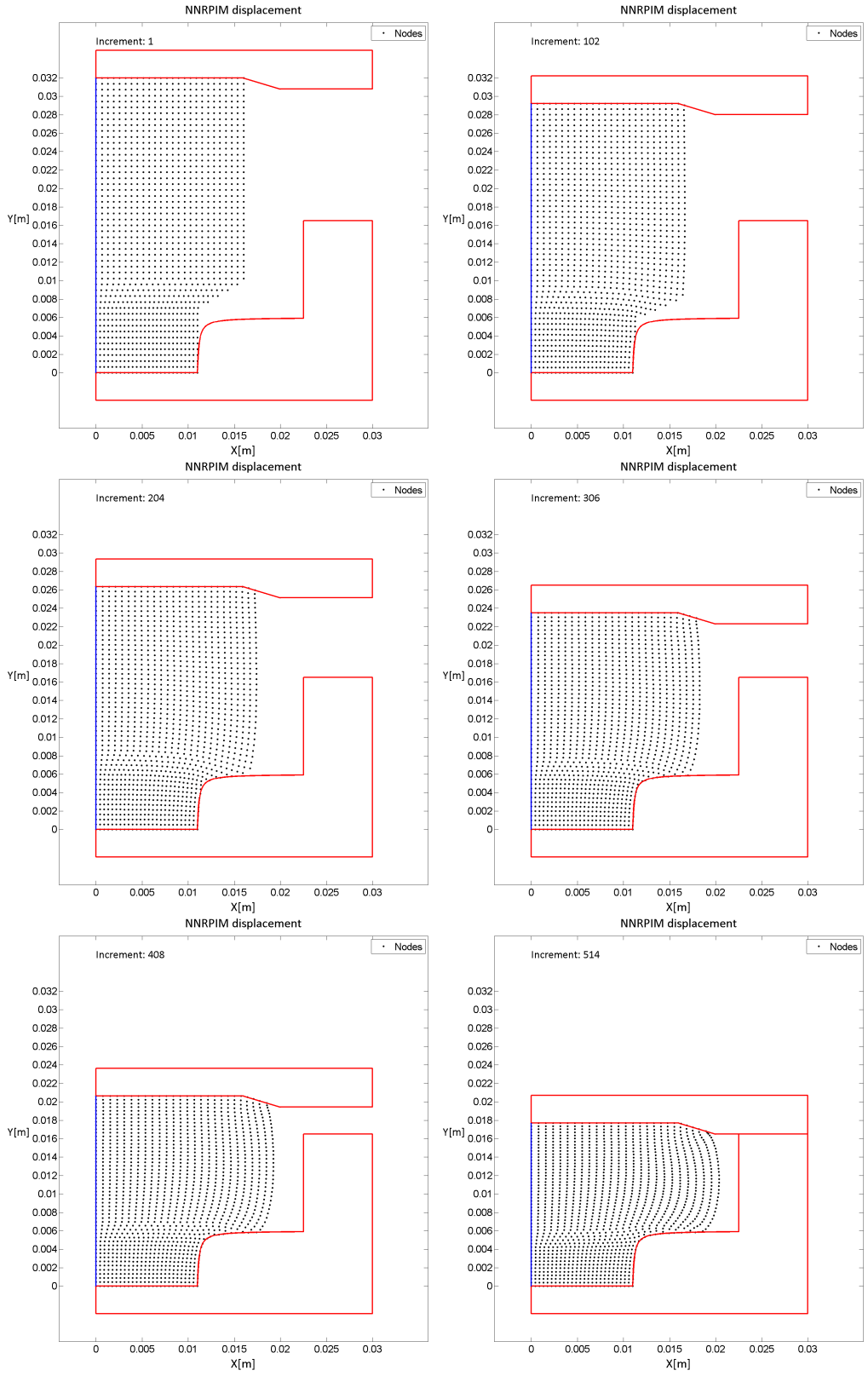

Figure 4.52: Evolution of the deformation and the contact on the upsetting for plane strain analysis.

4.3.9 Forging

The final example undertaken was an axisymmetric forging. The original example [89] used an elastoplastic model. Once again, since the model used in this work is not sufficient to analyze this kind of problems, it is recreated because of the complexity involved in the contact, more specifically a static linear boundary and a dynamic asymptotic boundary. The dimensions and boundary conditions are presented in Figure 4.53.

The Young modulus E used is 200 GPa, and the Poisson ratio ν is 0,3. It is considered both plane stress and plane strain analysis. The imposed displacement V is 0,165 m, which is half the vertical distance between the punch and the die.

The bottom boundary is a simple linear boundary that is defined using the linear equation in its standard form, as mention before.

The top boundary is an asymptotic function $f(x)$ of type

$$y = -a(x-b) + c(x-b)^{-1} + d \tag{4.24}$$

where a, b, c and d are constant parameters. Their values are

$$\begin{cases} a = 0,15 \\ b = 0,0185 \\ c = 5e-4 \\ d = 0,251 \end{cases} \tag{4.25}$$

For further information on how to determine the contact point in the asymptotic boundary, refer to Appendix E.

In Figure 4.54 is presented the evolution of the deformation and the contact, considering a mesh of 1326 nodes for plane stress, and in Figure 4.55 for plane strain analysis.

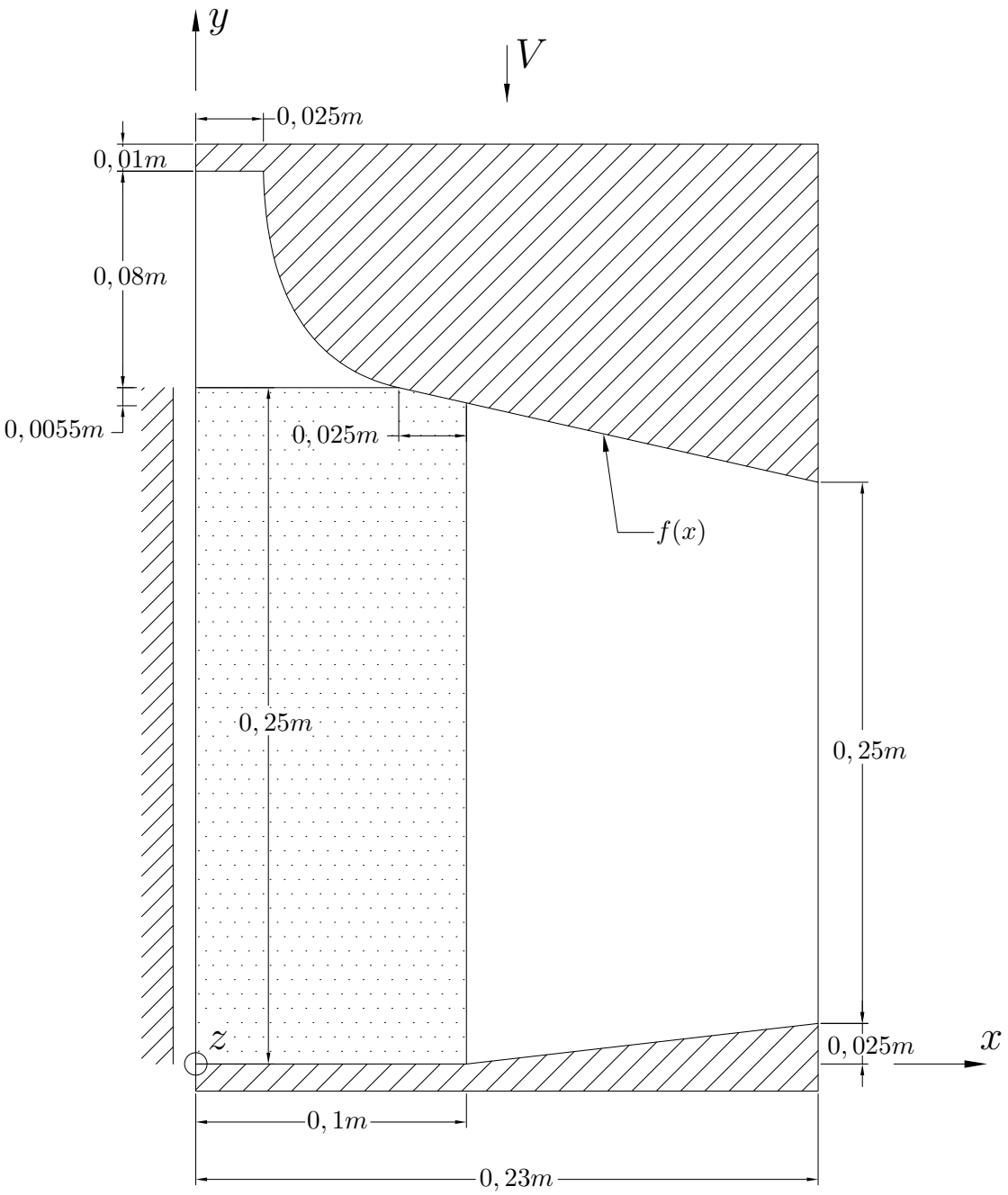

Figure 4.53: Forging: dimensions and boundary conditions.

4

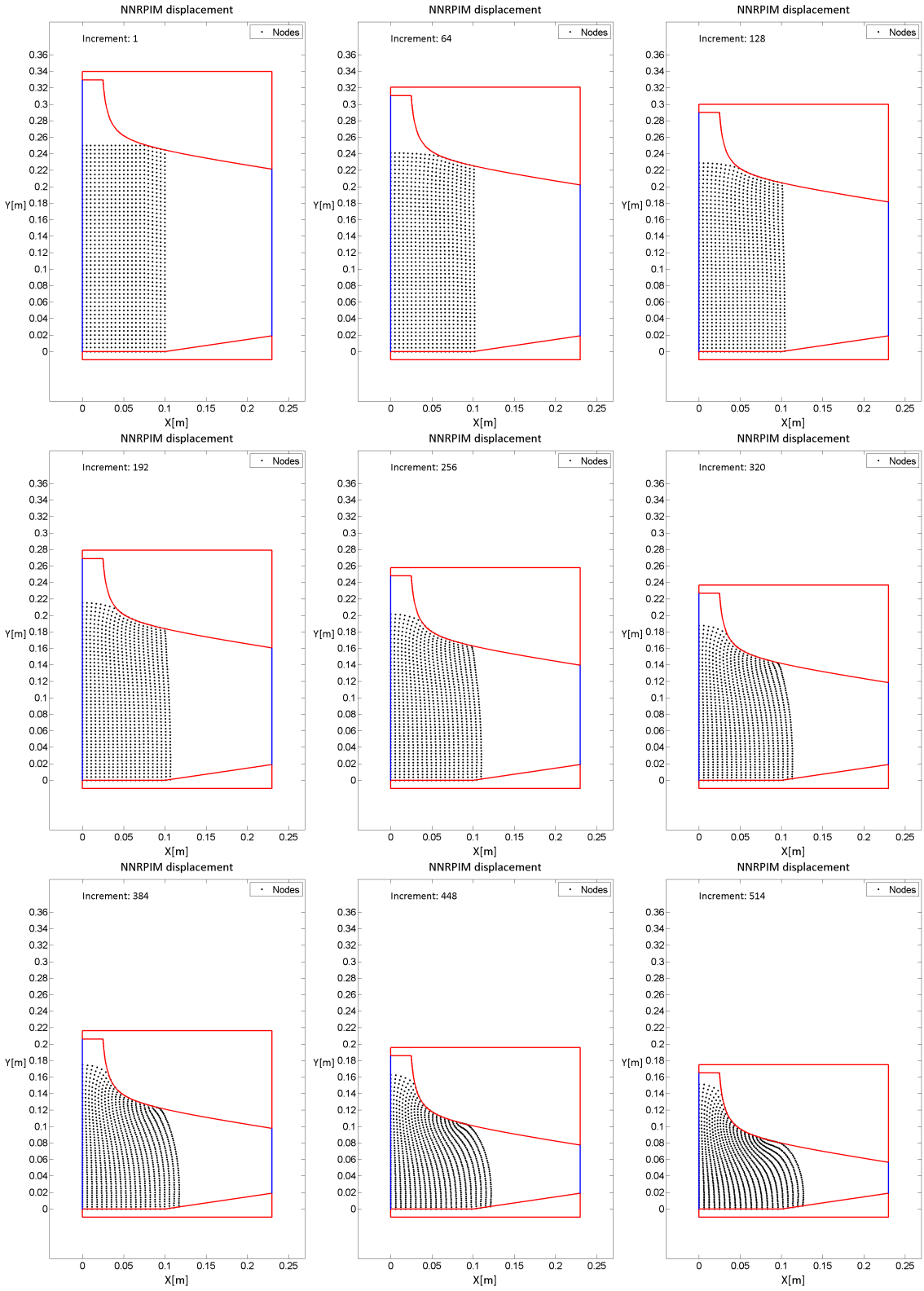

Figure 4.54: Evolution of the deformation and the contact on the forging for plane stress analysis.

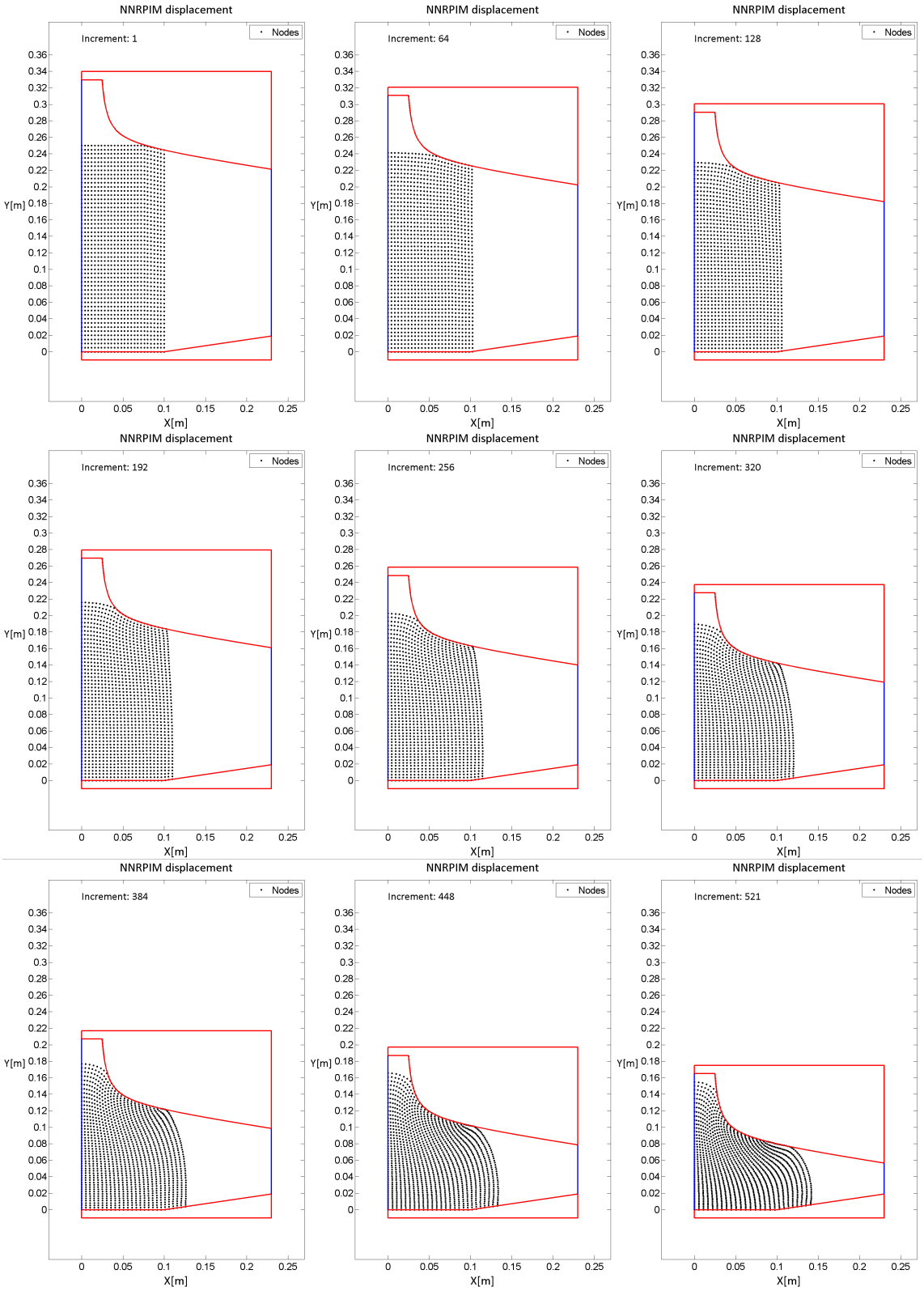

Figure 4.55: Evolution of the deformation and the contact on the forging for plane strain analysis.

Chapter 5

Conclusions and future works

5.1 Conclusions

In this work, the contact problem was extended to the NNRPIM. An approximated non-linear algorithm was applied based on an incremental approach. In each increment the nodal mesh and integration mesh are updated. It was verified that, when dealing with an incremental approach, the integration mesh needs to be updated, otherwise a bad distribution of integration points is obtained. In each increment, the algorithm searches for contact nodes, and if there are any, in the next increment applies the needed boundary conditions. Also in each increment is verified if at least one of the contact nodes should leave the boundary.

The approximated non-linear method used, is easy implemented, however it leads to considerable error in some cases. Nevertheless the contact problem was successfully applied.

Several examples were undertaken. Different boundary shapes were used: constant; linear function; cubic function; circumference; asymptotic function. Both static and dynamic boundaries were used.

5.2 Future works

For future works it is suggested to:

- Apply an exact non-linear method, as well as an elastoplastic model, very useful for forging problems. Then run the previous examples to compare diferences;
- Make a more generic algorithm for searching nodes in contact and impose boundary conditions, in order to eliminate the need to define the boundary with a function;
- Implement friction in the algorithm;

- Following the example of the ring compression, add the ability to detect self-contact, using a generic algorithm;
- Extend the developed algorithm to the 3D space;
- Evolve the algorithm to be able to consider two or more solids in contact and not just one solid with boundaries.

References

[1] J.V. Neumann and H. Goldstine. Numerical inverting of matrices of high order. *Bulletin of the American Mathematical Society*, 53:1021–1099, 1947.

[2] A. Bultheel and R. Cools. *The Birth of Numerical Analysis*. World Scientific, Singapore, 2010.

[3] J.N. Reddy. *An Introduction to the Finite Element Method, 2nd edition*. McGraw-Hill, U.S.A, 1993.

[4] R.J. Leveque. *Finite Difference Methods for Ordinary and Partial Differential Equations, Steady-state and Time-Dependent Problems*. Society for Industrial and Applied Mathematics, U.S.A, 2007.

[5] K.J. Bathe. *Finite Element Procedures*. Prentice-Hall, Englewood Cliffs, NJ, 1996.

[6] P.G. Ciarlet and J.L. Lions. *Handbook of Numerical Analysis, Vol. II, Finite Element Methods (Part 1)*. Elsevier Science B.V. (North-Holland), 1991.

[7] G.R. Liu. *Mesh Free Methods, Moving beyond the Finite Element Method*. CRC Press, U.S.A., 2002.

[8] T. Belytschko, Y. Krongauz, D. Organ, M. Fleming, and P. Krysl. Meshless methods: an overview and recent developments. *Comput. Methods Appl. Mech. Engrg.*, 139: 3–47, 1996.

[9] J. Belinha. The natural neighbour radial point interpolation method, solid mechanics and mechanobiology applications. master thesis. Technical report, Porto, 2010.

[10] B. Nayroles, G. Touzot, and P. Villon. Generalizing the finite element method: Diffuse approximation and diffuse elements. *Computation Mechanics*, 10:307–318, 1992.

[11] P. Lancaster and K. Salkauskas. Surfaces generated by moving least squares methods. *Mathematics of computation*, 37:141–158, 1981.

[12] T. Belytschko, Y.Y. Lu, and L. Gu. Element-free galerkin methods. *International Journal for Numerical Methods in Engineering*, 37:229–256, 30 January 1994.

[13] L.B. Lucy. A numerical approach to the testing of the fission hypothesis. *The astronomical journal*, 82:1013–1024, December 1977.

[14] R.A. Gingold and J.J. Monaghan. Smoothed particle hydrodynamics - theory and application to non-spherical stars. *Monthly notices of the royal astronomical society*, 181:375–389, November 1977.

[15] V.P. Nguyen, T. Rabczuk, S. Bordas, and M. Duflot. Meshless methods: A review and computer implementation aspects. *Mathematics and Computers in Simulation*, 79: 763–813, 1 December 2008.

[16] J. Bonet and S. Kulasegaram. Correction and stabilization of smooth particle hydrodynamics methods with applications in metal forming simulations. *International Journal for Numerical Methods in Engineering*, 47:1189–12, 28 February 2000.

[17] J.J. Monaghan. Why particle methods work. *SIAM Journal on Scientific and Statistical Computing*, 3:422–433, 1982.

[18] J.J. Monaghan. An introduction to sph. *Computer Physics Communications*, 48:89–96, January 1988.

[19] W.K. Liu, S. Jun, and Y. F. Zhang. Reproducing kernel particle methods. *International Journal for Numerical Methods in Fluids*, 20:1081–1106, 15 May 1995.

[20] S.N. Atluri and T. Zhu. A new meshless local petrov-galerkin (mplg) approach in computational mechanics. *Computational Mechanics*, 22:117–127, August 1998.

[21] S.N. Atluri and S. Shen. The meshless local petrov-galerkin (mplg) method: A simple & less-costly alternative to the finite element and boundary element methods. *Computer Modeling in Engineering & Sciences*, 3, 2002.

[22] S. De and K.J. Bathe. The method of finite spheres. *Computation Mechanics*, 25:329–345, April 2000.

[23] E. Oñate, S. Idelsohn, O.C. Zienkiewicz, and R.L. Taylor. A finite point method in computational mechanics. applications to convective transport and fluid flow. *International Journal for Numerical Methods in Fluids*, 39:3839–3866, 30 November 1996.

[24] E. Oñate, S. Idelsohn, O.C. Zienkiewicz, and C. Sacco R.L. Taylor. A stabilized finite point method for analysis of fluid mechanics problems. *Computer Methods in Applied Mechanics and Engineering*, 139:315–346, 15 December 1996.

[25] R.L. Hardy. Theory and applications of the multiquadrics - biharmonic method (20 years of discovery 1968-1988). *Computers and Mathematics with Applications*, 19:127–161, 1990.

[26] R.L. Hardy. Multiquadric equations of topography and other irregular surfaces. *Journal of geophysical research*, 76:1905–1915, 1971.

[27] E.J. Kansa. Multiquadrics - a scattered data approximation scheme with applications to computational fluid-dynamics - i surface approximations and partial derivative estimates. *Computers & Mathematics with Applications*, 19:127–145, 1990.

[28] E.J. Kansa. Multiquadrics - a scattered data approximation scheme with applications to computational fluid-dynamics - ii solutions to parabolic, hyperbolic and elliptic partial differential equations. *Computers & Mathematics with Applications*, 19:147–161, 1990.

[29] A.J.M. Ferreira, C.M.C. Roque, and P.A.L.S. Martins. Radial basis functions and higher-order shear deformation theories in the analysis of laminated composite beams and plates. *Composite Structures*, 66:287–293, October–December 2004.

[30] C.M. Tiago and V.M.A. Leitão. Application of radial basis functions to linear and nonlinear structural analysis problems. *Computers & Mathematics with Applications*, 51:1311–1334, April 2006.

[31] G.R. Liu and Y.T. Gu. A point interpolation method for two-dimensional solids. *International Journal for Numerical Methods in Engineering*, 50:937–951, 2001.

[32] G.R. Liu. A point assembly method for stress analysis for two-dimensional solids. *International Journal of Solids and Structures*, 39:261–276, January 2002.

[33] J.G. Wang and G.R. Liu. A point interpolation meshless method based on radial basis functions. *International Journal for Numerical Methods in Engineering*, 54:1623–1648, 20 August 2002.

[34] J.G. Wang and G.R. Liu. On the optimal shape parameters of radial basis functions used for 2-d meshless methods. *Computer Methods in Applied Mechanics and Engineering*, 191:2611–2630, 29 March 2002.

[35] G.R. Liu, G.Y. Zhang, Y.T. Gu, and Y.Y. Wang. A meshfree radial point interpolation method (rpim) for three-dimensional solids. *Computational Mechanics*, 36:421–430, November 2005.

[36] S.R. Idelsohn and E. Oñate. The meshless finite element method. *International Journal for Numerical Methods in Engineering*, 58:893–912, 14 October 2002.

[37] L. Traversoni. Natural neighbour finite elements. *International conference on hydraulic engineering software, hydrosoft proceedings*, 2:291–297, 1994.

[38] N. Sukumar, B. Moran, A. Yu Semenov, and V. V. Belikov. Natural neighbour galerkin methods. *International Journal for Numerical Methods in Engineering*, 50:1–27, 2001.

[39] J. Braun and M. Sambridge. A numerical method for solving partial differential equations on highly irregular evolving grids. *Nature*, 376:655–660, 24 August 1995.

[40] N. Sukumar. The natural element method in solid mechanics. ph.d. dissertation. Technical report, Evanston, Illinois, 1998.

[41] N. Sukumar, B. Moran, A. Yu Semenov, and V. V. Belikov. The natural element method in solid mechanics. *International Journal for Numerical Methods in Engineering*, 43:839–887, November 15 1998.

[42] N. Sukumar and B. Moran. Natural neighbour interpolant for partial diferential equations. *Numerical Methods for Partial Diferential Equations*, 15:417–447, 1999.

[43] E. Cueto, M. Doblaré, and L. Gracia. Imposing essential boundary conditions in the natural element method by means of density-scaled α-shapes. *International Journal for Numerical Methods in Engineering*, 49:519–546, 10 October 2000.

[44] L.M.J.S. Dinis, R.M. Natal Jorge, and J. Belinha. Analysis of 3d solids using the natural neighbour radial point interpolation method. *Computer Methods in Applied Mechanics and Engineering*, 196:2009–2028, 1 March 2007.

[45] G. Voronoï. Nouvelles applications des paramètres continus à la théorie des formes quadratiques. deuxième mémoire. recherches sur les parallélloèdres primitifs. *Journal für die reine und angewandte Mathematik*, 134:198–287, 1908.

[46] B. Delaunay. Sur la sphere vide. a la memoire de georges voronoï. *Izv. Akad. Nauk SSSR, Otdelenie Matematicheskih i Estestvennyh Nauk*, 7:793–800, 1934.

[47] L.M.J.S. Dinis, R.M. Natal Jorge, and J. Belinha. Analysis of plates and laminates using the natural neighbour radial point interpolation method. *Engineering Analysis with Boundary Elements*, 32:267–279, March 2008.

[48] L.M.J.S. Dinis, R.M. Natal Jorge, and J. Belinha. An unconstrained third-order plate theory applied to functionally graded plates using a meshless method. *Mechanics of Advanced Materials and Structures*, 17:108–133, 2010.

[49] L.M.J.S. Dinis, R.M. Natal Jorge, and J. Belinha. Composite laminated plates: A 3d natural neighbor radial point interpolation method approach. *Journal of Sandwich Structures and Materials*, 12:119–138, 2010.

[50] L.M.J.S. Dinis, R.M. Natal Jorge, and J. Belinha. A 3d shell-like approach using a natural neighbour meshless method: Isotropic and orthotropic thin structures. *Composite Structures*, 92:1132–1142, April 2010.

[51] L.M.J.S. Dinis, R.M. Natal Jorge, and J. Belinha. The natural neighbour radial point interpolation method: dynamic applications. *Engineering Computations*, 16:911–949, 2009.

[52] L.M.J.S. Dinis, R.M. Natal Jorge, and J. Belinha. The dynamic analysis of thin structures using a radial interpolator meshless method, in vibration and strucutural acoustics analysis. *Solid Mechanics and Mechanobiology Applications*, 248, 2011.

[53] L.M.J.S. Dinis, R.M. Natal Jorge, and J. Belinha. Static and dynamic analysis of laminated plates based on an unconstrained third order theory and using a radial point interpolator meshless method. *Computers & Structures*, 89:1771–1784, October 2011.

[54] L.M.J.S. Dinis, R.M. Natal Jorge, and J. Belinha. A natural neighbour meshless method with a 3d shell-like approach in the dynamic analysis of thin 3d structures. *Thin-Walled Structures*, 49:185–196, January 2011.

[55] L.M.J.S. Dinis, R.M. Natal Jorge, and J. Belinha. The natural neighbour radial point interpolation meshless method applied to the non-linear analysis. volume 248, page 1175, 2011.

[56] L.M.J.S. Dinis, R.M. Natal Jorge, and J. Belinha. Large deformation applications with the radial natural neighbours interpolators. *Computer Modeling in Engineering and Sciences (CMES)*, 44:1–34, 2009.

[57] J. Belinha, R.M. Natal Jorge, and L.M.J.S. Dinis. Bone tissue remodelling analysis considering a radial point interpolator meshless method. *Engineering Analysis with Boundary Elements*, 36:1660–1670, November 2012.

[58] P.W. Christensen, A. Klarbring, J.S. Pang, and N. Strömberg. Formulation and comparison of algorithms for frictional contact problems. *International Journal for Numerical Methods in Engineering*, 42:145–173, 15 May 1998.

[59] P. Wriggers. Finite element algorithms for contact problems. *Archives of Computational Methods in Engineering*, 2:1–49, December 1995.

[60] H. Hertz. Study on the contact of elastic bodies. *J. Reine Angew. Math*, 29:156–171, 1882.

[61] Z.H. Zhong. *Finite Element Procedures for Contact-Impact Problem*. Oxford University Press Inc, U.S.A, 1993.

[62] G.ML. Gladwell. *Contact problems in the classical theory of elasticity*. Kluwer Academic Print on Demand, 1980.

[63] K.L. Johnson. *Contact mechanics*. Cambridge university press, 1987.

[64] K.J. Bathe and A. Chaudhary. A solution method for planar and axisymmetric contact problems. *International Journal for Numerical Methods in Engineering*, 21:65–88, 1985.

[65] T. W. Mcdevitt and T. A. Laursen. A mortar-finite element formulation for frictional contact problems. *International Journal for Numerical Methods in Engineering*, 48:1525–1547, 2000.

[66] T.A. Laursen. Formulation and treatment of frictional contact problems using finite elements, phd thesis. Technical report, Stanford, July 1992.

[67] N. Kikuchi and J.T. Oden. *Contact Problems in Elasticity*. Society for Industrial and Applied Mathematics, U.S.A, 1988.

[68] O. C. Zienkiewicz. The finite element method in structural and continuum mechanics. London, 1967. ISBN 99-0388-272.

[69] O. C. Zienkiewicz. *The finite element in Engineering science*. McGraw-Hill, London, 1971.

[70] O. C. Zienkiewicz. *The finite element method*. McGraw-Hill, London, 1977.

[71] K.J. Bathe. *Finite element procedures in engineering analysis*. Prentice-Hall, Englewood Cliffs, 1982.

[72] T.J.R. Hughes. *The finite element method - Linear static and dynamic finite element analysis*. Prentice-Hall, Englewood Cliffs, 1987.

[73] O.C. Zienkiewicz and R.L. Taylor. *The finite element method, 4th edition*. McGraw-Hill, New York, 1989.

[74] J.T. Oden. *Finite elements of non linear continua*. McGraw-Hill, New York, 1972.

[75] A. Signorini. Sopra akune question di elastostatica. In *Atti della Societa Italiana per il Progresso delle Scienze*, 1933.

[76] A.F.M. Azevedo. *Método dos Elementos Finitos 1ª Edição*. Faculdade de Engenharia da Universidade do Porto, 2003.

[77] R.D. Cook, D.S. Malkus, and M.E. Plesha. *Concepts and Applications of Finite Element Analysis, 3rd edition*. John Wiley & Sons, Inc., 1989.

[78] S. Beissel and T. Belytschko. Nodal integration of the element-free galerkin method. *Computer Methods in Applied Mechanics and Engineering*, 139:49–74, 15 December 1996.

[79] M. A. Puso, J.S. Chen, E. Zywicz, and W. Elmer. Meshfree and finite element nodal integration methods. *International Journal for Numerical Methods in Engineering*, 74: 416–446, 16 April 2008.

[80] N.R. Aluru. A point collocation method based on reproducing kernel approximations. *International Journal for Numerical Methods in Engineering*, 47:1083–1121, 28 February 2000.

[81] D.W. Kim. Point collocation methods using the fast moving least-square reproducing kernel approximation. *International Journal for Numerical Methods in Engineering*, 56:1445–1464, 28 February 2003.

[82] R. Sibson. A brief description of natural neighbour interpolation. *Interpreting multivariate data*, 21, 1981.

[83] C.L. Lawson. *Software for C1 surface interpolation. in J. R. Rice (ed.), Mathematical Software III, Volume 3*. Academic Press, New York, 1977.

[84] J.G. Wang, G.R. Liu, and Y.G. Wu. A point interpolation method for simulating dissipation process of consolidation. *Computer Methods in Applied Mechanics and Engineering*, 190:5907–5922, 31 August 2001.

[85] J.N. Reddy. *Applied Functional Analysis and Variational Methods in Engineering*. McGraw-Hill, Singapore, 1986.

[86] D. L. Logan. *A First Course in the Finite Element Method, 4th edition*. Thompson, India, 2007.

[87] S.P. Timoshenko and J.N. Goodier. *Theory of elasticity*. McGraw-Hill Kogakusha, Tokyo, 3rd edition, 1970.

[88] Wikiversity. Introduction to elasticity/plate with hole in tension, June 2013. URL http://en.wikiversity.org/wiki/Introduction_to_Elasticity/Plate_with_hole_in_tension. [Online; accessed 17-June-2013].

[89] Kie-Chan Kwon, Sang-Hoon Park, and Sung-Kie Youn. The least-squares meshfree method for elasto-plasticity and its application to metal forming analysis. *International Journal for Numerical Methods in Engineering*, 64:751–788, 14 October 2005.

[90] J.R. Xiao, B.A. Gama, J.W. Gillespie Jr, and E.J. Kansa. Meshless solutions of 2d contact problems by subdomain variational inequality and mlpg method with radial basis functions. *Engineering Analysis with Boundary Elements*, 29:95–106, February 2005.

[91] N.H. Kim, K.K. Choi, and J.S. Chen. Die shape design optimization of sheet metal stamping process using meshfree method. *International Journal for Numerical Methods in Engineering*, 51:1385–1405, 30 August 2001.

[92] D.A. Hu, S.Y. Long, X. Han, and G.Y. Li. A meshless local petrov-galerkin method for large deformation contact analysis of elastomers. *Engineering Analysis with Boundary Elements*, 37:657–666, July 2007.

[93] Jiun-Shyan Chen and Hui-Ping Wang. New boundary condition treatments in meshfree computation of contact problems. *Computer Methods in Applied Mechanics and Engineering*, 187:441–468, 7 July 2000.

[94] Jiun-Shyan Chen, Cristina Maria Oliveira Lima Roque, Chunhui Pan, and Sérgio Tonini Button. Analysis of metal forming process based on meshless method. *Journal of Materials Processing Technology*, 80–81:642–646, 1 August 1998.

Appendix A

Intersection with a linear or constant dynamic boundary

In order to determine the intersection of the line defined by the initial and final position of a node, with a constant static boundary, it is only required to substitute in the linear equation the respective coordinate value. With a linear boundary, the intersection is defined as a system of linear equations

$$\begin{cases} A_1 x + B_1 y = C_1 \\ A_2 x + B_2 y = C_2 \end{cases} \tag{A.1}$$

which solved to obtain y originate

$$y = \frac{C_2 - \frac{A_2}{A_1} C_1}{B_2 - \frac{A_2}{A_1} B_1} \tag{A.2}$$

and solved to obtain x originate

$$x = \frac{C_2 - \frac{B_2}{B_1} C_1}{A_2 - \frac{B_2}{B_1} A_1} \tag{A.3}$$

In the case of a dynamic boundary (see Figure A.1), it is required to recall equations (3.5) and (3.6). Since a constant boundary is a particular case of a linear equation, consider the last in its standard form

$$Ax + By = C \tag{A.4}$$

where A and B are constant coefficients corresponding to the two coordinates of the line normal vector.

The slope of the line is

$$S = -\frac{A}{B} \tag{A.5}$$

and the intersection with the yy axis is

$$y_{intercept} = \frac{C}{B} \tag{A.6}$$

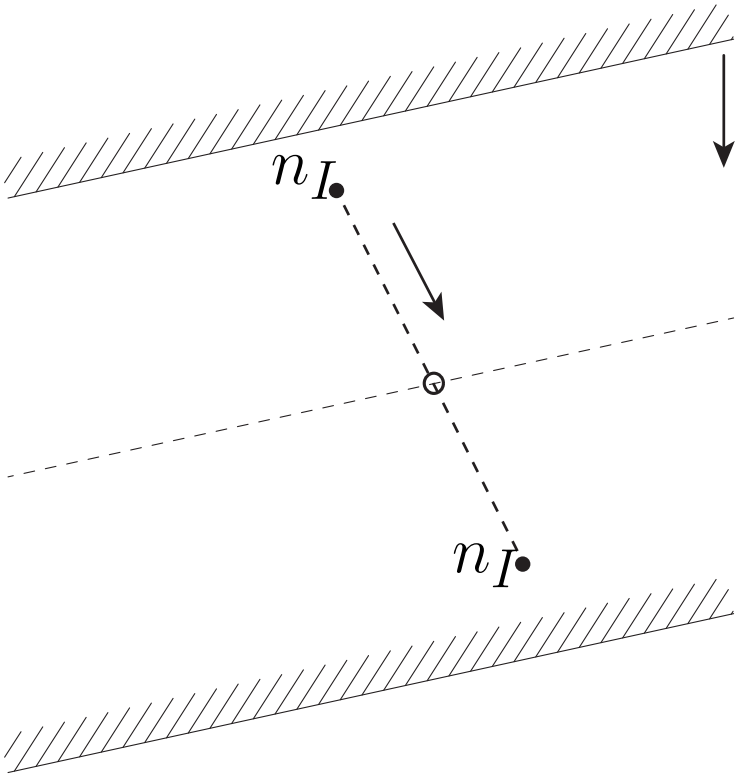

Figure A.1: Initial and final position of contact node and initial and final position of dynamic linear boundary with a vertical displacement.

The linear equation is a static equation, but the boundary moves, that means the equation needs to be changed accordingly to equations (3.5) and (3.6).

The line normal remains the same so, coefficients A and B are constant. Hence the value that makes the boundary change its position is C.

The coefficient C can be written as

$$C_{final} = Vr_f + C_{initial} \tag{A.7}$$

being V the imposed boundary displacement.

As so, equation (A.4) becomes

$$Ax + By = Vr_f + C_{initial} \tag{A.8}$$

This equation only defines a dynamic boundary. To achieve the intersection, x and y are replaced by equations (3.5) and (3.6). As so the equation takes the form

$$A(ur_f + x_{initial}) + B(vr_f + y_{initial}) = Vr_f + C_{initial} \tag{A.9}$$

Developing this equation to express the regress factor in function of the other terms

$$\begin{aligned} Aur_f + Ax_{initial} + Bvr_f + By_{initial} = Vr_f + C_{initial} \Leftrightarrow \\ \Leftrightarrow r_f(Au + Bv - V) = C_{initial} - Ax_{initial} - By_{initial} \end{aligned} \tag{A.10}$$

and so the regress factor is defined as

$$r_f = \frac{C_{initial} - Ax_{initial} - By_{initial}}{Au + Bv - V} \tag{A.11}$$

In the particular case of the line being a horizontal line, the normal vector of that line is $\mathbf{n} = [0\ 1\ 0]$ and so equation (A.11) simplifies to

$$r_f = \frac{C_{initial} - By_{initial}}{Bv - V} \tag{A.12}$$

If the line is vertical, then the normal vector is $\mathbf{n} = [1\ 0\ 0]$ and equation (A.11) simplifies to

$$r_f = \frac{C_{initial} - Ax_{initial}}{Au - V} \tag{A.13}$$

Appendix B

Intersection with a circular static boundary

The equation for a circumference with its centre in an arbitrary point is

$$(x-a)^2+(y-b)^2=r_c^2 \tag{B.1}$$

being (a,b) the coordinates of the circumference's centre.

To intercept the node position line with the circumference (see Figure B.1), is necessary to solve the following system of equations

$$\begin{cases} Ax+By=C \\ (x-a)^2+(y-b)^2=r_c^2 \end{cases} \Leftrightarrow \tag{B.2a}$$

$$\Leftrightarrow \begin{cases} x=\dfrac{C-By}{A} \\ x^2-2xa+a^2+y^2-2by+b^2=r_c^2 \end{cases} \tag{B.2b}$$

Developing the second equation in order to y and replacing x by the first equation

$$x^2+y^2-2xa-2by+b^2+a^2-r_c^2=0 \Leftrightarrow \tag{B.3a}$$

$$\Leftrightarrow \left(\frac{C-By}{A}\right)^2+y^2-2\left(\frac{C-By}{A}\right)a-2by+b^2+a^2-r_c^2=0 \Leftrightarrow \tag{B.3b}$$

$$\Leftrightarrow \frac{C^2-2CBy+B^2y^2}{A^2}+y^2-\frac{2Ca}{a}+\frac{2Bya}{A}-2by+b^2+a^2-r_c^2=0 \Leftrightarrow \tag{B.3c}$$

$$\Leftrightarrow \left(\frac{B^2}{A^2}+1\right)y^2+\left(-\frac{2CB}{A^2}+\frac{2Ba}{A}-2b\right)y+\left(-\frac{2Ca}{A}+\frac{C^2}{A^2}+b^2+a^2-r_c^2\right)=0 \tag{B.4}$$

The obtained solution (equation (B.4)) is a second degree equation that, after being solved with an appropriate method permits two solutions. From the two solutions, it is chosen the real solution that is closer to the initial position of the node, in terms of y, since the equation was derived for y.

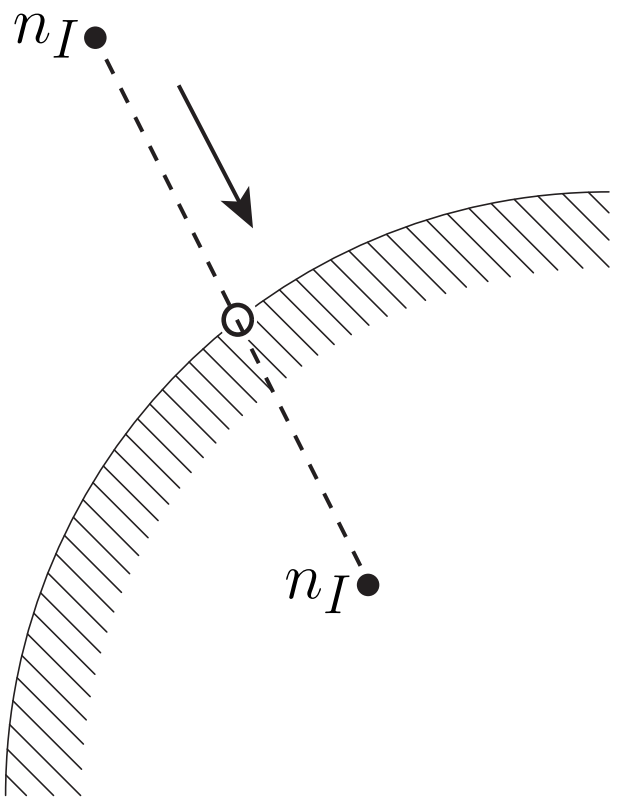

Figure B.1: Position of a contact node before and after he passed a circular boundary.

Appendix C

Intersection with a cubic static boundary

Consider a cubic boundary generated with a function of type

$$y = \left(\frac{(x-b)}{a}\right)^3 - c \tag{C.1}$$

where a, b and c are constant parameters that define the cubic function.

The intersection of the node position line and the cubic boundary (see Figure C.1), is defined by the system of equations

$$\begin{cases} Ax + By = C \\ y = \left(\frac{(x-b)}{a}\right)^3 - c \end{cases} \tag{C.2}$$

Before solving the system, the cubic equation can be developed as follows

$$y = \left(\frac{x-b}{a}\right)\left(\frac{x-b}{a}\right)\left(\frac{x-b}{a}\right) - c \Leftrightarrow \tag{C.3a}$$

$$\Leftrightarrow y = \frac{x^2 - bx - bx + b^2}{a^2}\left(\frac{x-b}{a}\right) - c \Leftrightarrow \tag{C.3b}$$

$$\Leftrightarrow y = \frac{x^3 - 2bx^2 + b^2x - bx^2 + 2b^2x - b^3}{a^3} - c \tag{C.3c}$$

After substituting the linear equation in the form $y = \frac{C - Ax}{B}$ in equation (C.3c), the equation development continues

$$\frac{C - Ax}{B} = \frac{x^3}{a^3} - \frac{2b}{a^3}x^2 + \frac{b^2}{a^3}x - \frac{b}{a^3}x^2 + \frac{2b^2}{a^3}x - \frac{b^3}{a^3} - c \Leftrightarrow \tag{C.4a}$$

$$\Leftrightarrow \frac{C}{B} = \frac{x^3}{a^3} - \frac{2b}{a^3}x^2 + \frac{b^2}{a^3}x - \frac{b}{a^3}x^2 + \frac{2b^2}{a^3}x - \frac{b^3}{a^3} + \frac{A}{B}x - c \Leftrightarrow \tag{C.4b}$$

$$\Leftrightarrow \left(\frac{1}{a^3}\right)x^3 + \left(-\frac{2b}{a^3} - \frac{b}{a^3}\right)x^2 + \left(\frac{b^2}{a^3} + \frac{2b^2}{a^3} + \frac{A}{B}\right)x + \left(-\frac{b^3}{a^3} - \frac{C}{B} - c\right) = 0 \quad \text{(C.5)}$$

Finally a third order equation is obtained, which needs to be solved with an appropriate method. From the three solutions, the one that matters is the real solution closer to the initial position of the node, in terms of x, since the equation was derived for x.

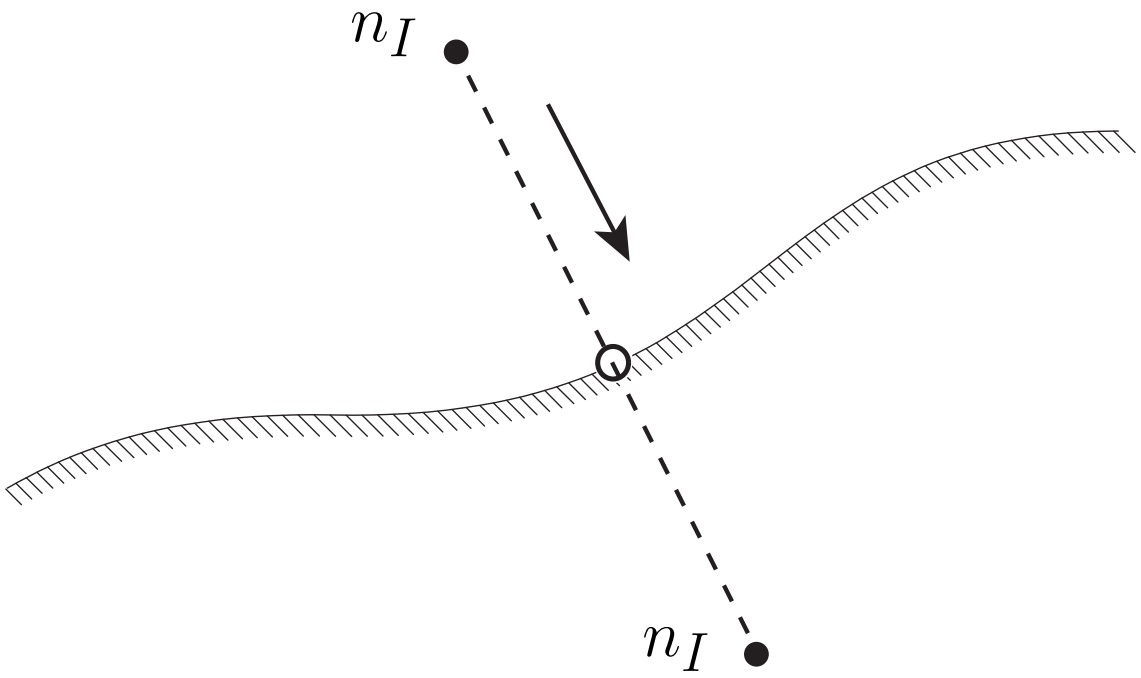

Figure C.1: Position of a contact node before and after he passed a cubic boundary.

Appendix D

Intersection with an asymptotic static boundary

Consider an asymptotic boundary generated with a function of type

$$y = \frac{1}{-x + a} + b \tag{D.1}$$

where a and b are constant parameters that define the asymptotic function. For scaling purposes, the previous equation will be changed to

$$y = \left(\frac{1}{-1000x + a} + b\right)\frac{1}{1000} \tag{D.2}$$

To intercept the boundary with the line that define the node position (see Figure D.1), it is required to solve the next system of equations

$$\begin{cases} Ax + By = C \\ y = (\frac{1}{-1000x + a} + b)\frac{1}{1000} \end{cases} \tag{D.3}$$

Before solving the system, the boundary equation can be developed as follows

$$1000y = \frac{1}{-1000x + a} + b \Leftrightarrow \tag{D.4a}$$

$$\Leftrightarrow 1000y - b = \frac{1}{-1000x + a} \Leftrightarrow \tag{D.4b}$$

$$\Leftrightarrow (1000y - b)(-1000x + a) = 1 \Leftrightarrow \tag{D.4c}$$

$$\Leftrightarrow -1e6yx + 1000ay + 1000bx - ba = 1 \tag{D.4d}$$

After substituting the linear equation in the form $x = \frac{C - By}{A}$ in equation (D.4d), the equation can be developed

$$-1e6y(\frac{C-By}{A}) + 1000ay + 1000b(\frac{C-By}{A}) - ba = 1 \Leftrightarrow \tag{D.5a}$$

$$\Leftrightarrow -1e6y(\frac{C-By}{A}) + 1000ay + 1000b(\frac{C-By}{A}) - ba - 1 = 0 \Leftrightarrow \tag{D.5b}$$

$$\Leftrightarrow -1e6\frac{C}{A} + 1e6\frac{B}{A}y^2 + 1000ay + 1000b\frac{C}{A} - 1000b\frac{B}{A}y - ba - 1 = 0 \Leftrightarrow \tag{D.5c}$$

$$\Leftrightarrow (1e6\frac{B}{A})y^2 + (-1e6\frac{C}{A} + 1000a - 1000b\frac{B}{A})y + (1000b\frac{C}{A} - ba - 1) = 0 \tag{D.6}$$

Thus it is obtained a second order equation that, after being solved with an appropriate method permits two solutions. It is chosen the real solution closer to the initial position of the node, in terms of y, since the equation was derived for y.

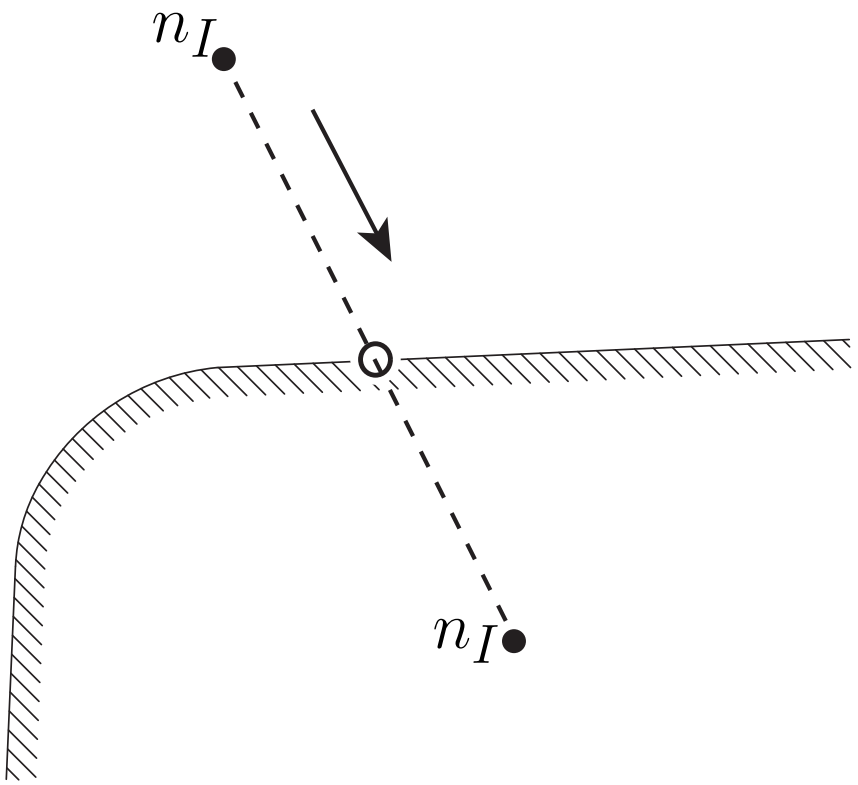

Figure D.1: Position of a contact node before and after he passed an asymptotic boundary.

Appendix E

Intersection with an asymptotic dynamic boundary

Consider an asymptotic boundary generated with a function of type

$$y = -a(x-b) + c(x-b)^{-1} + d \tag{E.1}$$

were coefficients a, b, c and d are constants.

This is a static equation, but the boundary moves (see Figure E.1), that means the equation needs to be changed accordingly to equations (3.5) and (3.6).

Parameters a and c are shape parameters that have to do with the shape of the boundary, therefore remain constant. Parameter b is a translation along xx direction, so considering the boundary moves vertically, it also remains constant. The only parameter that changes is d, which has to do with the vertical translation.

The parameter d can be written as

$$d_{final} = Vr_f + d_{initial} \tag{E.2}$$

being V the imposed boundary displacement.

As so, equation (E.1) becomes

$$y = -a(x-b) + c(x-b)^{-1} + Vr_f + d_{initial} \tag{E.3}$$

This equation only defines a dynamic boundary. To achieve the intersection x and y are replaced by equations (3.5) and (3.6). The final equation is defined as

$$(vr_f + y_{initial}) = -a((ur_f + x_{initial}) - b) + c((ur_f + x_{initial}) - b)^{-1} + Vr_f + d_{initial} \tag{E.4}$$

This equation is an implicit equation of the variable r_f, so no further development is made. The equation needs to be solved by an iterative process. The sought solution is the real solution contained in the interval $[0\ 1]$. Obviously, there is only one solution to be found, because there is only one geometric place where the node intercepts the boundary.

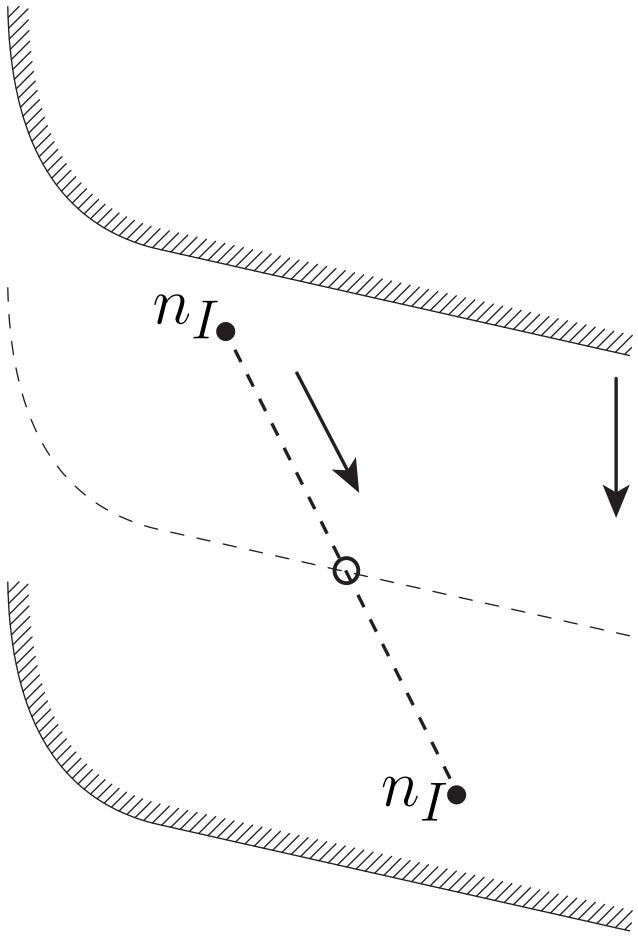

Figure E.1: Initial and final position of contact node and initial and final position of dynamic asymptotic boundary.